Report of Investigation 2018-2

Tsunami Inundation Maps for Skagway and Haines, Alaska

D.J. Nicolsky, E.N. Suleimani, and J.B. Salisbury

Published by
STATE OF ALASKA
DEPARTMENT OF NATURAL RESOURCES
DIVISION OF GEOLOGICAL & GEOPHYSICAL SURVEYS
June 2018

Cover. View of Haines city harbor. Photo by Elena Suleimani.

Tsunami Inundation Maps for Skagway and Haines, Alaska

D.J. Nicolsky, E.N. Suleimani, and J.B. Salisbury

Report of Investigations 2018-2

State of Alaska
Department of Natural Resources
Division of Geological & Geophysical Surveys

State of Alaska
Bill Walker, Governor

Department of Natural Resources
Andrew T. Mack, Commissioner

Division of Geological & Geophysical Surveys
Steve Masterman, State Geologist and Director

Publications produced by the Division of Geological & Geophysical Surveys (DGGS) are available for download from the DGGS website (dggs.alaska.gov). Publications on hard-copy or digital media can be examined or purchased in the Fairbanks office:

Alaska Division of Geological & Geophysical Surveys
3354 College Rd., Fairbanks, Alaska 99709-3707
Phone: (907) 451-5010 Fax (907) 451-5050
dggspubs@alaska.gov | dggs.alaska.gov

DGGS publications are also available at:
Alaska State Library,
Historical Collections & Talking Book Center
395 Whittier Street
Juneau, Alaska 99811

Alaska Resource Library and Information Services (ARLIS)
3150 C Street, Suite 100
Anchorage, Alaska 99503

Suggested citation:
Nicolsky, D.J., Suleimani, E.N., and Salisbury, J.B., 2018, Tsunami inundation maps for Skagway and Haines, Alaska: Alaska Division of Geological & Geophysical Surveys Report of Investigation 2018-2, 69 p., 3 sheets. http://doi.org/10.14509/30029

Contents

Figures

Tables

Appendix

Map Sheets

Tsunami Inundation Maps for Skagway and Haines, Alaska

D.J. Nicolsky[1], E.N. Suleimani,[1] and J.B. Salisbury[2]

Abstract

In this report we evaluate potential tsunami hazards for the southeastern Alaska communities of Skagway and Haines and numerically model the extent of inundation from tsunami waves generated by tectonic and submarine landslide sources. We calibrate our tsunami model by numerically simulating the 2011 Tohoku, Japan tsunami at Skagway and comparing our results to instrument records. Analysis of calculated and observed water level dynamics for the 2011 event in Skagway reveals that the model underestimates the observed wave heights in the city by a factor of 1.5, likely due to complex tsunami-tide interactions. We compensate for this underestimation numerically by increasing the coseismic slip of the hypothetical tsunami sources in our models. Potential hypothetical maximum credible tsunami sources include variations of the extended 1964 rupture and megathrust earthquakes in the Prince William Sound and Alaska Peninsula regions. Local underwater landslide events in Taiya, Chilkoot, and Chilkat inlets are also considered as possible tsunamigenic scenarios. The results show that the maximum predicted wave height resulting from a tectonic tsunami is 2–3 m (7–10 ft) in Skagway and Haines, while the maximum landslide-generated tsunami may cause a runup of 15–16 m (49–52 ft). Results presented here are intended to provide guidance to local emergency management agencies in tsunami inundation assessment, evacuation planning, and public education to mitigate future tsunami hazards.

INTRODUCTION

Subduction of the Pacific plate under the North American plate has resulted in numerous great earthquakes and is the source of locally-generated tsunamis in Alaska (Dunbar and Weaver, 2008). Several historic earthquakes along the Alaska–Aleutian subduction zone (fig. 1) have generated tsunamis resulting in widespread damage and loss of life in exposed coastal communities in Alaska and throughout the Pacific (Lander, 1996). However, tsunamis originating in the vicinity of the Aleutian Islands, Alaska Peninsula, and the Gulf of Alaska are of particular concern to Alaskans because, as local hazards, waves can reach coastal communities within minutes of the earthquake that caused them.

The vulnerability of Alaska's coast to tsunami waves was demonstrated by the March 27, 1964, Great Alaska earthquake. This M_w 9.2 megathrust earthquake (fig. 1) was the largest recorded earthquake in North America and generated the most destructive tsunami in Alaska history (Johnson and others, 1996; Kanamori, 1970; Lander, 1996; Plafker and others, 1969). In addition to the major tectonic tsunami triggered by ocean-floor displacement, multiple local tsunamis were generated by submarine landslides. The landslide-generated tsunamis arrived almost immediately after shaking was felt, leaving virtually no time for warning or evacuation. Of the 131 fatalities associated with the 1964 earthquake, 122 were caused by tectonic and landslide-generated tsunamis (Lander, 1996). The local tsunamis in the Gulf of Alaska region caused most of the damage and accounted for 76 percent of the aforementioned 122 tsunami deaths (Lander, 1996).

The 1964 tsunami did not uniformly impact the vast Alaska coastline. Waves did not cause significant damage in Skagway and Haines. The 1964 tsunami arrived in Skagway approximately three hours after the earthquake on a rising tide and its height was estimated to be about 5 m (16 ft).

[1]Alaska Earthquake Center, Geophysical Institute, University of Alaska, P.O. Box 757320, Fairbanks, Alaska 99775-7320; djnicolsky@alaska.edu
[2]Alaska Division of Geological & Geophysical Surveys, 3354 College Rd., Fairbanks, Alaska 99709-3707

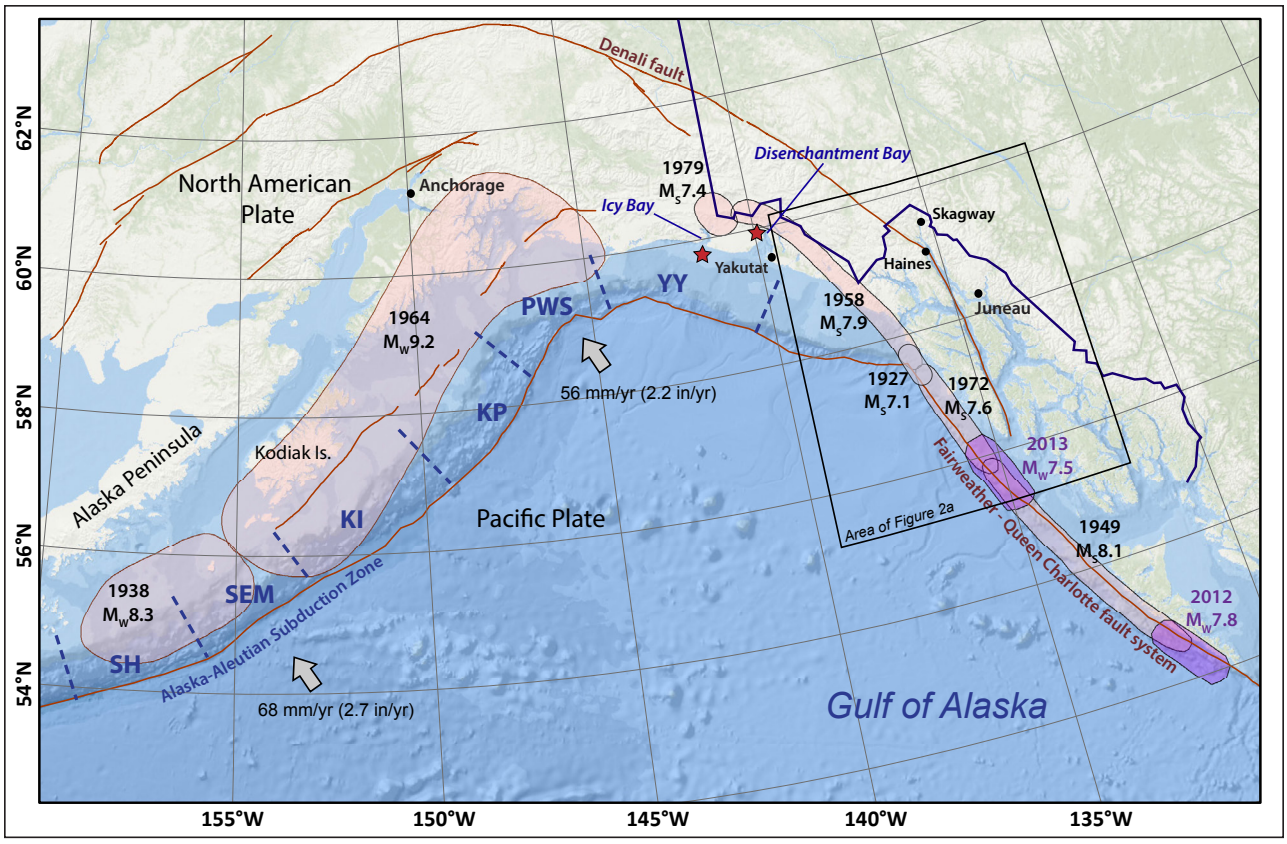

Figure 1. Map of south-central and southeastern Alaska, showing rupture areas of major historical earthquakes (light pink shading) and the two most recent major earthquakes in Southeast Alaska (dark pink shading). Gray arrows and the numbers next to them indicate the direction and rate of plate convergence, respectively. Red lines are major active faults. Red stars mark epicenters of two September 1899 earthquakes. The segment notations of the Alaska–Aleutian megathrust are from Nishenko and Jacob (1990): Yakataga–Yakutat (YY), Prince William Sound (PWS), Kenai Peninsula (KP), Kodiak Island (KI), Semidi Islands (SEM), and Shumagin Islands (SH) segments. The area inside the black rectangle is shown in detail in figure 2A.

The water inundated about 3 m (10 ft) above the bay level but caused no damage (Lander, 1996). At Haines, unusually high tides of 5.8 m (19.0 ft) were reported about 6 hours after the earthquake and were followed by five more waves about 1 hour apart (Lander, 1996). During future tsunamis, it is possible that the highest wave in the tsunami wave train could arrive during high tide and cause more damage than occurred in 1964. The potential future occurrence of earthquakes and tsunamis in the Gulf of Alaska and around the Pacific Ocean necessitates the development of inundation and tsunami evacuation maps for use in tsunami risk mitigation.

We approach this problem—modeling the outcome of different tsunami-generating scenarios—deterministically. This means we are not focused on calculating the relative likelihood and frequency of various magnitude earthquakes, as is done for land-use planning or insurance estimates (Geist and Lynett, 2014; Geist and Parsons, 2006). Because the known earthquake and tsunami history of Alaska is short, we instead model the results of many hypothetical earthquakes and landslides to explore potential "worst case scenarios" given details of the region. Producing a tsunami inundation map for a community therefore consists of several steps. First, we develop credible scenarios for maximum considered tsunamigenic earthquakes based on historical records and known fault segmentation. We then model tsunami dynamics resulting from each of

the scenarios; again, we do not assign probabilities to the earthquake occurrences. The results are then compared with historical tsunami observations if such data exist. Finally, we develop a "worst-case" inundation line that encompasses the maximum extent of flooding from all model simulations of all source scenarios and historical observations. The worst-case inundation line becomes a basis for local tsunami hazard planning.

The intended audience for this report consists of scientists, engineers, and planners interested in mitigating effects of tsunami inundation and utilizing results to develop evacuation maps. Digital data and documentation provided with the report enable technical users to explore the range of tsunami inundation expected for future events.

PROJECT BACKGROUND: REGIONAL AND HISTORICAL CONTEXT

Setting

Skagway (59°27' N, 135°19' W) is a town in southeastern Alaska with a population of 1,065 (Alaska Department of Labor and Workforce Development, 2016). It is located 145 km (90 mi) northwest of Juneau at the northernmost end of Lynn Canal (figs. 2A and 2B). Skagway has deep roots in Klondike Gold Rush history and is a popular cruise ship stop for summer tourists. The population of Skagway more than doubles in the summer season with the influx of working people to accommodate the tourist trade.

Haines (59°14' N, 135°27' W) is a town in southeastern Alaska with a population of 2,466 (Alaska Department of Labor and Workforce Development, 2016). It is located 129 km (80 mi) northwest of Juneau on the shores of Lynn Canal (figs. 2A and 2B) between the Chilkoot and Chilkat inlets. The first permanent U.S. military installation in Alaska, Fort William H. Seward, was constructed south of Haines in 1904. Until World War II, it was the only U.S. Army post in Alaska.

Earthquake and tsunami history

Skagway and Haines are in southeastern Alaska, where the primary tectonic elements of the Pacific–North American plate boundary are the Alaska–Aleutian subduction zone and the >1,000-km-long (>620-mi-long) Fairweather–Queen Charlotte (FW–QC) fault system (fig. 1). In southeastern Alaska, plate motion is accommodated along the Fairweather fault, a right-lateral transform fault that extends primarily offshore along the entire southeastern Alaska coastline, becoming the Queen Charlotte fault to the south in British Columbia (figs. 1 and 2A). The entire FW-QC fault system ruptured in large strike-slip earthquakes over the last hundred years: 1927 (M_S 7.1; Sykes, 1971), 1949 (M_S 8.1; Sykes, 1971), 1958 (M_S 7.9; Tocher, 1960), 1972 (M_S 7.6; Page, 1973), 2012 (M_W 7.8; Leonard and Bednarski, 2015), and 2013 (M_W 7.5; Holtkamp and Ruppert, 2015). See Suleimani and others (2013, figure 4) for additional rupture location details of these earthquakes and further information on seismotectonics of the region. An analysis of the above-mentioned events indicates that seismic slip along the FW–QC fault system is parallel to the direction of motion between the North American and the Pacific plates (Doser and Lomas, 2000). Recently, an unusual thrust event on the southern part of the FW–QC fault system—the 2012 Haida Gwaii earthquake—generated a large tsunami along the outer coast of British Columbia. The local run-up was observed to reach 7.5 m (24.6 ft) in some inlets near the rupture area. Although large magnitude earthquakes can occur on the FW-QC fault system, the predominantly strike-slip mechanism of these earthquakes lack large vertical perturbations to the sea floor and are therefore unlikely to generate large tsunamis in Skagway and Haines.

Most of the hazard related to the strike-slip earthquakes, besides the strong ground shaking, is related to ground failures. The 1958 M_S 7.9 Lituya earthquake triggered a large landslide into Lituya

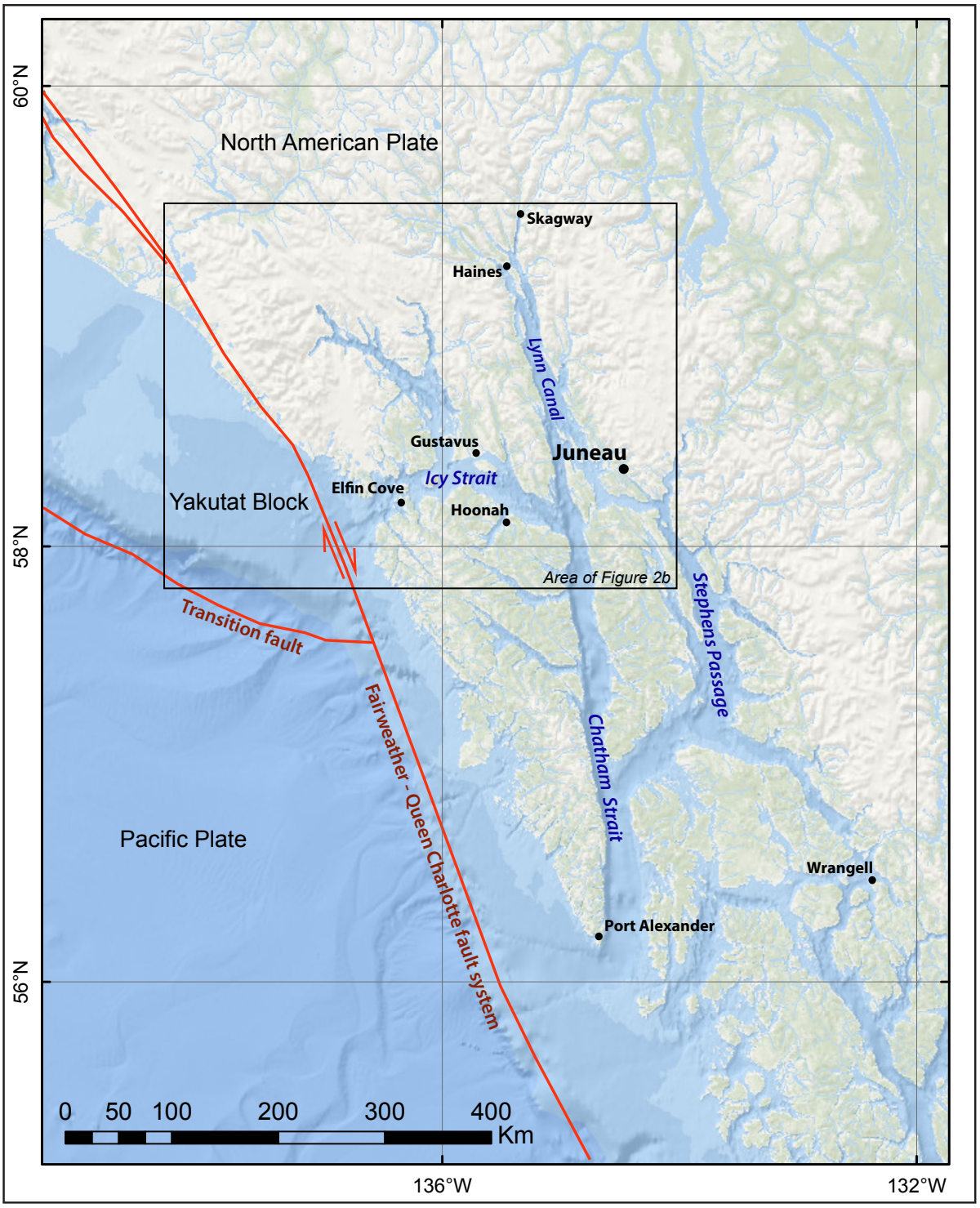

Figure 2A. Map of southeastern Alaska showing the location of Skagway and Haines with respect to other communities. The area inside the black rectangle is shown in figure 2B.

Bay (fig. 2B) that generated a 530 m-high (1,740 ft-high) wave (Miller, 1960). Other smaller landslides and ground failures during the 1958 event occurred in Disenchantment Bay, Dry Bay, the Haines/Skagway area, and near Wrangell (Lander, 1996). Several cable breaks occurred in Lynn Canal between Juneau and Skagway (locations indicated by red crosses in fig. 2B). No tsunami damage was reported for Skagway and Haines during the 1958 event.

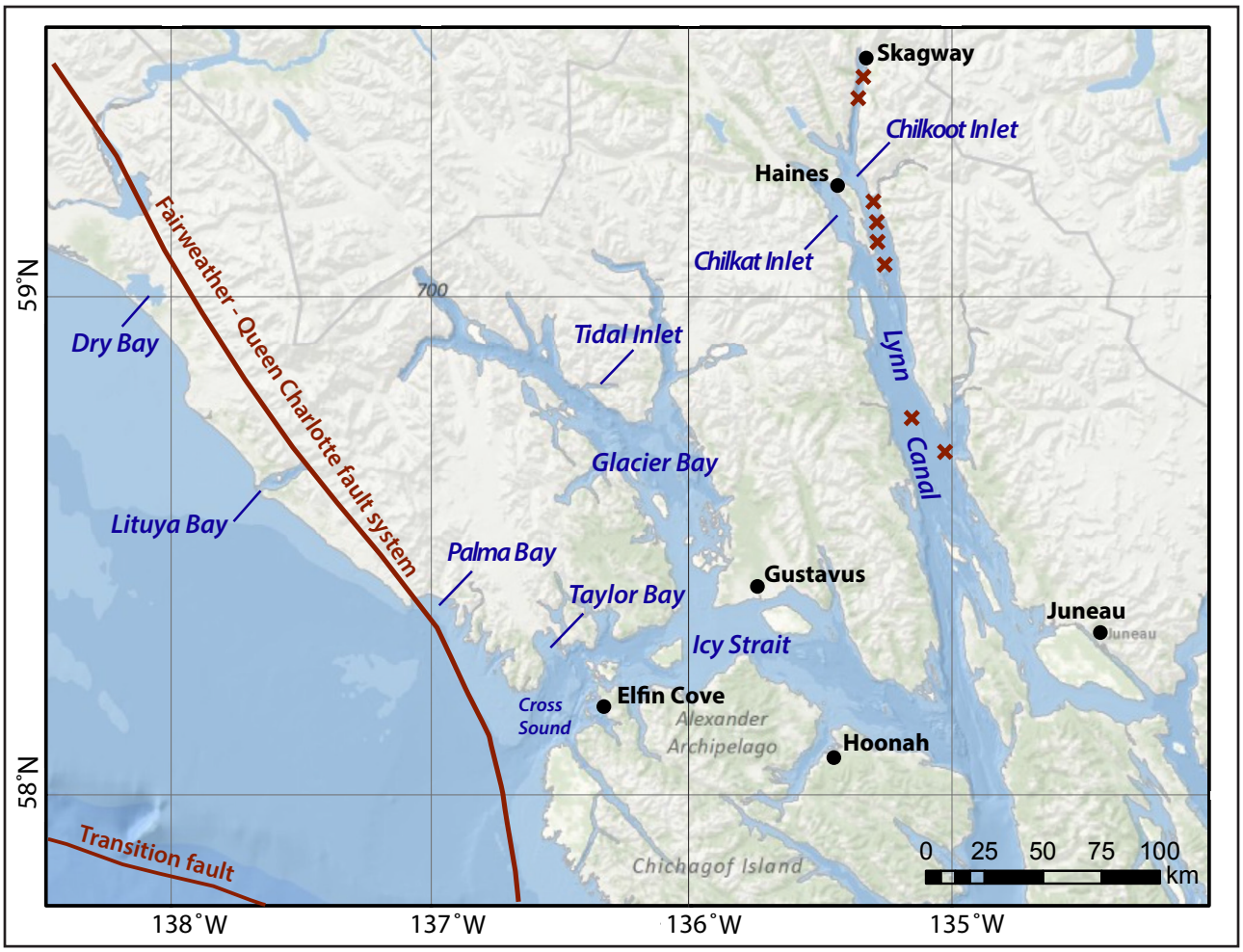

Figure 2B. Detailed map of the areas adjacent to Icy Strait and Lynn Canal. Red crosses indicate locations of underwater cable breaks associated with the M_S 7.9 earthquake of June 9, 1958.

Skagway and Haines are located on the shores of Lynn Canal, which is one of the major passages that weave through southeastern Alaska and British Columbia (figs. 2A and 2B). The towns are generally protected from earthquake-generated tsunami waves coming from the Pacific Ocean, as they are located far from the ocean at the end of a complex inlet configuration. Only several historical tectonic tsunamis have reached the towns, and none have resulted in any damage or loss of life. Because future earthquakes in the area might have different patterns of energy release, we cannot rely solely on historical events to estimate hazards as this could lead to significant underestimation of potential inundation in the communities. Table 1 provides a summary of tectonic and landslide tsunami effects at Skagway and Haines in the last century, as summarized by Lander (1996), and recent trans-Pacific and local tsunami records extracted from the tsunami database of the National Center for Environmental Information (NCEI). The following descriptions of earthquakes and landslides that have affected Skagway and Haines are taken from Lander (1996) unless otherwise noted:

1907, September 24. A report from Haines said that the Davidson Glacier was moved a half mile by the shock (Lander, 1996). Captain Nyland of the Petrel, which was four miles north of Haines, observed a slight temporary change in water level (Tarr and Martin, 1912, p. 96). The earthquake was recorded on the seismograph at Sitka, and Soloviev and Go (1975), p. 216-217) estimate the magnitude

Table 1. Tsunami effects at Skagway and Haines; data from the National Geophysical Data Center Global Historical Tsunami Database and comments from Lander (1996).

Date	Magnitude (M_w)	Origin	Maximum water height (m)	Comments
Skagway				
10/24/1927	7.1	Southeast Alaska	Observed	Heavy seas broke towline, water muddy and churned. The Juneau-Skagway-Haines cable broke in two places. Cable breaks were ascribed to a submarine slide.
11/04/1952	8.2	Kamchatka Peninsula	0.01	
7/10/1958	7.9	Southeast Alaska	7.6	Landslide caused cable breaks.
5/22/1960	9.3	Chile	0.18	
3/28/1964	9.2	Gulf of Alaska	3.00	
11/03/1994	Landslide	Skagway Harbor	7.62	One person dead, $20 million damage.
3/11/2011	9.0	Japan: Honshu	0.21	
Haines				
10/24/1927	5.5	Alaska: Skagway	Observed	Small temporary change in water level noted.
3/28/1964	9.2	Gulf of Alaska	5.8	

to have been 5.5 based on the small record there. They believe the water change was a seiche as the magnitude was small. However, landslides and icefalls could be associated with small-to-moderate earthquakes.

1927, October 24. The most severe earthquake (magnitude 7.1) in the memory of local inhabitants occurred in Petersburg between 6:51 and 7:05 A.M. It was feared that a tidal wave or other disasters would result from the shock but none were reported (Lander, 1996). The Petersburg-Wrangell cable was cut about five miles west of Wrangell; the Juneau-Skagway-Haines cable broke in two places. Both cable breaks were ascribed to a submarine slide. Also, the Ketchikan-Wrangell cable was broken due to a "submarine landslide causing earthquake."

1958, July 10. The Alaska communication system had two cable breaks, one and three miles from the Skagway Beach terminal, caused by silt movement carried out into Lynn Canal from the Skagway River. Subaqueous slides in Taiya Inlet are blamed for 25 foot waves at Skagway that, coming at low water, caused no damage (Lemke and Yehle, 1972, p. 84). Tocher (1960) reports that these waves were augmented by subaerial slides from the steep-sided fjords. There were two other breaks south of the Katzehin River delta with the cables deeply buried. The break near the Katzehin River was buried under tons of sand, mud, and gravel. Significantly, there was a buoy at the mouth of the river, which was being used by a fisherman to maintain his boat's position. Immediately after the

earthquake he noticed that the buoy had disappeared. No trace of the buoy was found, but the fisherman did not mention any wave action.

1964, March 28. The marine cable was broken 19-1/5 miles south of Skagway near the delta of the Katzehin River. No visual wave was reported. The 1964 tsunami arrived in Skagway approximately three hours after the earthquake on a rising tide and the total height was estimated to be about 5 m (17 ft). Later the water inundated about 3 m (10 ft) above the bay level, but caused no damage. At Haines, unusually high tides of 5.8 m (19 ft) were reported about 6 hours after the earthquake, which were followed by five more waves about 1 hour apart.

1994, November 4. At 7:10 pm when the tide was at minus 4 feet, an 800-foot section of the 1,300-foot dock slid away on the eastern side of Skagway harbor. The dock was carried away when the underlying sediments collapsed and slid into deeper water. One person was caught under the pilings when the collapse occurred, and was killed by the returning wave. A 20- to 25-foot wave crossed the harbor and caused $2,000,000 damage to the ferry terminal near the middle of the harbor. A wave also entered the small boat harbor and caused about $100,000 damage there. The slide was estimated to have been 600 feet wide, 50 to 60 feet thick, and 4,500 feet long (1-3 million cubic yards). There was a report that a similar event had occurred in November, 1966, at night, and had left a scoured channel across the bottom of the bay due to the collapse of fill material near the location of the 1994 failure. There was no marigraph record for this date and no earthquakes occurred in this area in November 1966. The state of the tides is unknown, and it is not known whether a wave was generated. The slide of November 4, 1994 is described in more detail below.

In the "Landslide-Generated Tsunamis" section of his book, Lander (1996, p. 26) also mentions that slumps along the Katzehin River delta were responsible for many cable breaks but it is uncertain if these generated tsunamis.

Landslide tsunami hazard potential

Tsunamis caused by slope failures constitute a significant hazard in the fjords of coastal Alaska and other high-latitude fjord coastlines (Lee and others, 2006). Kulikov and others (1998) analyzed tsunami catalog data for Southeast Alaska and British Columbia and showed that this region has a long record of tsunami waves generated by submarine and subaerial landslides, avalanches, and rockfalls. In the majority of cases, tectonic tsunamis arriving in bays and fjords from the open ocean had wave heights smaller than those of local landslide-generated tsunamis. For example, the 1964 landslide-generated tsunami in Port Valdez devastated the waterfront and caused the 52 m (~170 ft) run-up near Shoup Bay, while the tectonic tsunami was not even noticed until a high tide late in the evening (Coulter and Migliaccio, 1966; Wilson and Tørum, 1968).

Fjords in southeastern Alaska are also prone to tsunami waves generated by subaerial rockfalls caused by fractures in the bedrock along fjord sidewalls. Evans and Clague (1994) described the process of glacier debuttressing as an important mechanism that generates instability of the rock slopes due to relaxation of internal stress after deglaciation. Southeastern Alaska is a tectonically active area, and earthquakes often trigger rock-slope failures in such environments. Although it is hard to separate the contribution of a seismic event into the triggering of a rockfall, Cossart and others (2008) found that glacial unloading and associated stress release play an important role in triggering rock-slope failures. One of the largest historical tsunami waves (generated by a subaerial rock-slope failure in Lituya Bay) occurred in 1958 and topped 530 m (1,740 ft) (Miller, 1960). Another massive subaerial landslide occurred near Tyndall Glacier

in Taan Fjord—an arm of Icy Bay—in October, 2015 (press release, University of Alaska Fairbanks, http://www.gi.alaska.edu/alaska-science-forum/giant-wave-icy-bay). A mountainside with an estimated volume of 55 million m^3 (72 million yd^3) collapsed into the fjord and caused 190 m (623 ft) run-up on the opposite side (P. Lynett, USC, oral communication, 2017). According to Geist and others (2003) and Wieczorek and others (2007), another potential massive subaerial landslide could occur in Tidal Inlet—a fjord in Glacier Bay (fig. 2B). Strong ground motions from an earthquake along the eastern part of the Denali fault (fig. 1) could also cause submarine landslides in fjords of Southeast Alaska. The tsunami hazard due to such an earthquake-induced landslide in nearby Alaska communities is assessed by Suleimani and others (2015).

The landslide and tsunami of November 3, 1994, in Skagway were studied in depth by many researchers (Campbell, 1997; Campbell and Nottingham, 1999; Cornforth and Lowell, 1996; Kowalik, 1997; Kulikov and others, 1996; Mader, 1997; Nottingham, 1997; Petroff and Watts, 1995; Plafker and Greene, 1998; Rabinovich and others, 1999; Raichlen and others, 1996; Synolakis, 1999; Thomson and others, 2001). It was concluded that failure initiated at the back of a riprap stockpile ~25 minutes after an extreme low tide and resulted in additional submarine slope failure (Cornforth and Lowell, 1996; Thomson and others, 2001). The sliding was accompanied by a series of tsunami waves with amplitudes ranging, according to observers, from 5 to 11 meters (16 to 36 feet) (Kulikov and others, 1996; Rabinovich and others, 1999; Raichlen and others, 1996).

Evidence of previous submarine landslides is also manifested as damage to submarine communication cables (Heezen and Johnson, 1969; Tarr and Martin, 1912). An overview of the natural seafloor processes that have resulted in damage to the Alaska underwater cable system was given by Heezen and Johnson (1969). The authors identified turbidity currents and gravitational slides as the primary causes of cable failures. They summarized numerous documented cable breaks in Lynn Canal near Skagway and Haines (fig. 3). Most of the submarine cable failures occurred near the mouth of the Katzehin River delta and in upper Taiya Inlet where the Skagway River is entering Taiya Inlet from the north (fig. 3). The 1958 Lituya earthquake triggered a sediment flow, which ran southward from Skagway and was amplified by slumps from the steep sides of the canal (Heezen and Johnson, 1969). There were also instances of cable failures due to south-directed

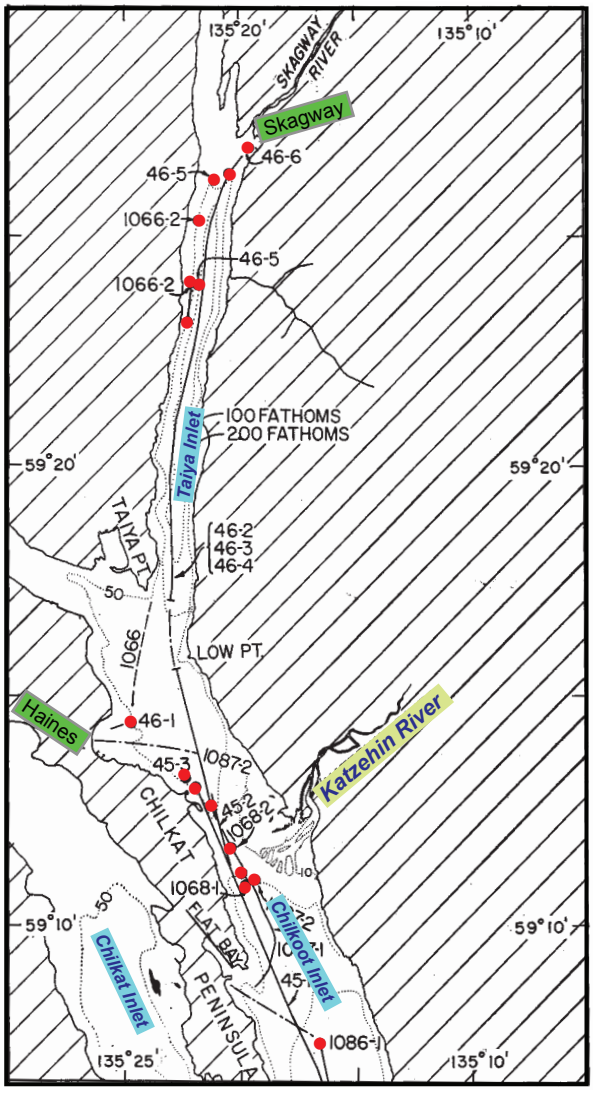

Figure 3. Documented breaks of underwater communication cables (modified from Heezen and Johnson, 1969).

slides and turbidity currents from the Katzehin River delta,which fills and nearly blocks Chilkoot Inlet (Heezen and Johnson, 1969).

One of the most recent cable failures in Southeast Alaska occurred on July 25, 2014, when an offshore M_W 6.1 strike-slip earthquake on the Fairweather fault was recorded near Palma Bay (fig. 2B). This event did not generate a tsunami, due to mostly horizontal displacements of the ocean floor. However, after the earthquake, the Alaska Communications Company reported a broken fiber optic cable caused by a submarine landslide in Cross Sound (Suleimani and others, 2015).

The combination of high sedimentation rates, abundant seismic activity, and a history of submarine landslides in the steep-sided fjords and canals of Southeast Alaska led us to consider several potential landslides as sources of tsunami waves that could impact Skagway and Haines. Figure 4 identifies six potential underwater slide areas on deltas of glacial rivers that deposit sediment on underwater slopes or submerged terminal moraines. Later in the report, we describe these submarine landslide-generated tsunami scenarios in detail and analyze results of numerical modeling of slide-generated waves.

A potentially unstable subaerial rock slump has been identified adjacent to the northern shore of Lutak Inlet near Haines, across the inlet from the Alaska Marine Highway Terminal (figs. 4B and 4C). This potential slump hasn't been investigated for tsunami-related hazards and associated risks imposed to ships and ferries that enter the Lutak Inlet. While it is known that earthquakes often trigger rock-slope failures in similar environments in southeastern Alaska, site-specific slope stability analysis that integrates geophysical, geological, and geotechnical data is required to adequately assess slope stability of this rock slump and its potential contribution to tsunami hazard.

METHODOLOGY AND DATA

Grid development and data sources

Numerical modeling of the governing equations for water dynamics requires a discrete approximation of the motion of a continuous medium—the water. In this work we discretize the shallow-water equations in spherical coordinates using a finite difference method. To compute a detailed map of potential tsunami inundation triggered by local and distant earthquakes, we use a series of nested computational grids. A nested grid allows for higher resolution in areas where it is needed without expending computer resources in areas where it is not. The bathymetric and topographic relief in each nested grid is based on digital elevation models (DEMs) developed at the National Center for Environmental Information (NCEI) of the National Oceanic & Atmospheric Administration (NOAA) in Boulder, Colorado (Caldwell and others, 2012). The extent of each grid used for inundation mapping of Skagway and Haines is listed in table 2. The coarsest grid (level 0) spans the central and northern Pacific Ocean and has a resolution of 2 arc-minutes (~2 km), while the two highest-resolution grids (level 4, Skagway high-resolution grid and level 4, Haines high-resolution grid) cover the communities only (fig. 5). We use three intermediate grids between the coarsest- and highest-resolution grids (table 2). Other grids were employed in testing sensitivity of the tsunami modeling to the grid resolution (Nicolsky and others, 2017).

The bathymetry data for the 2-arc-minute-resolution grid is extracted from the ETOPO2[1] dataset. The data sources and methodology used to create the 24-, 8-, and 3-arc-second and high-resolution DEMs are described in greater detail in Caldwell and others (2012), Love and others (2012), and Macpherson and others (2014).

[1]National Oceanic and Atmospheric Administration [NOAA], National Center for Environmental Information [NCEI]. http://www.ngdc.noaa.gov/mgg/bathymetry/relief.html

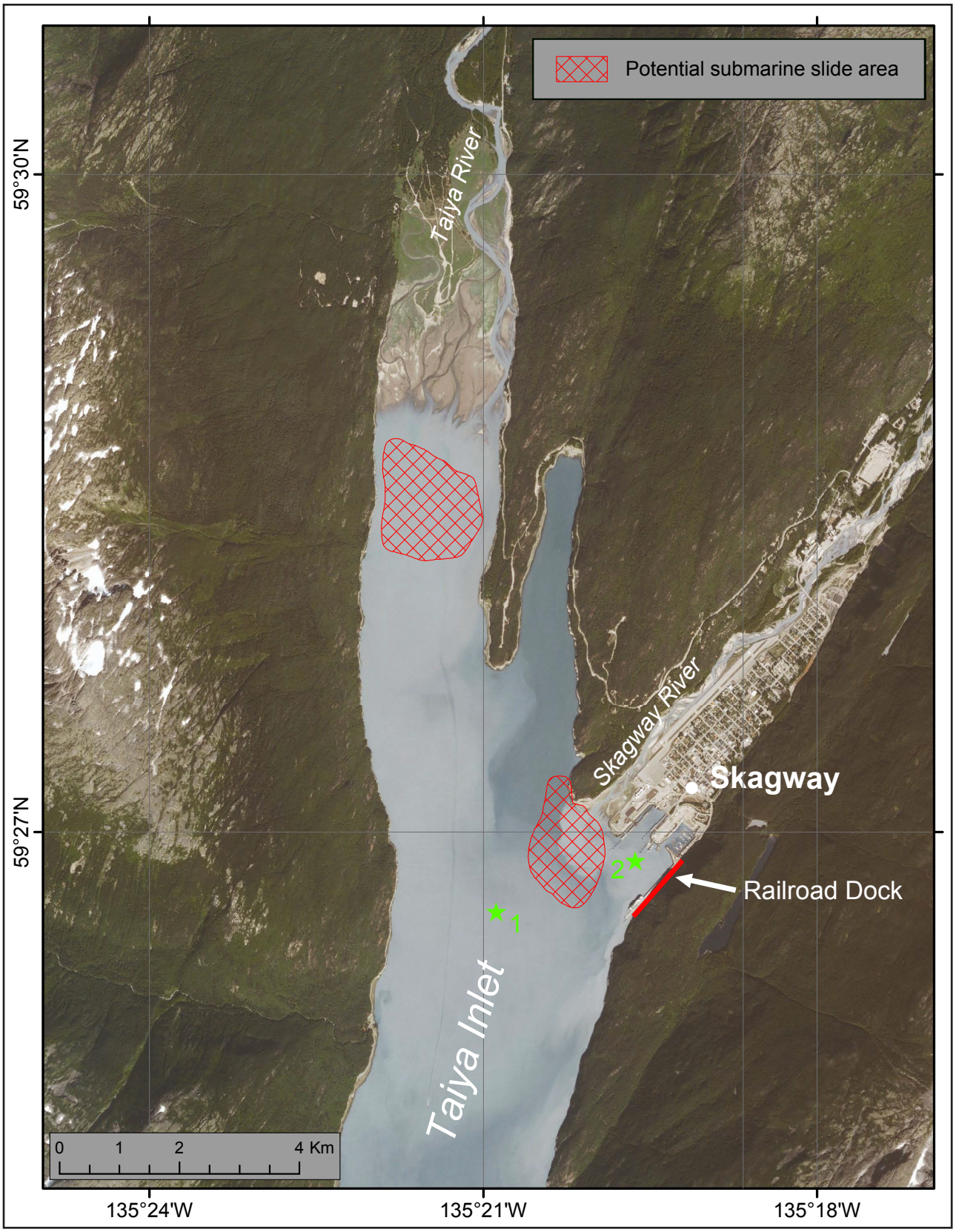

Figure 4A. Potential locations of underwater slides in the vicinity of Skagway. Green stars indicate locations where tsunami wave dynamics were compared for the NHWAVE and FUNWAVE models.

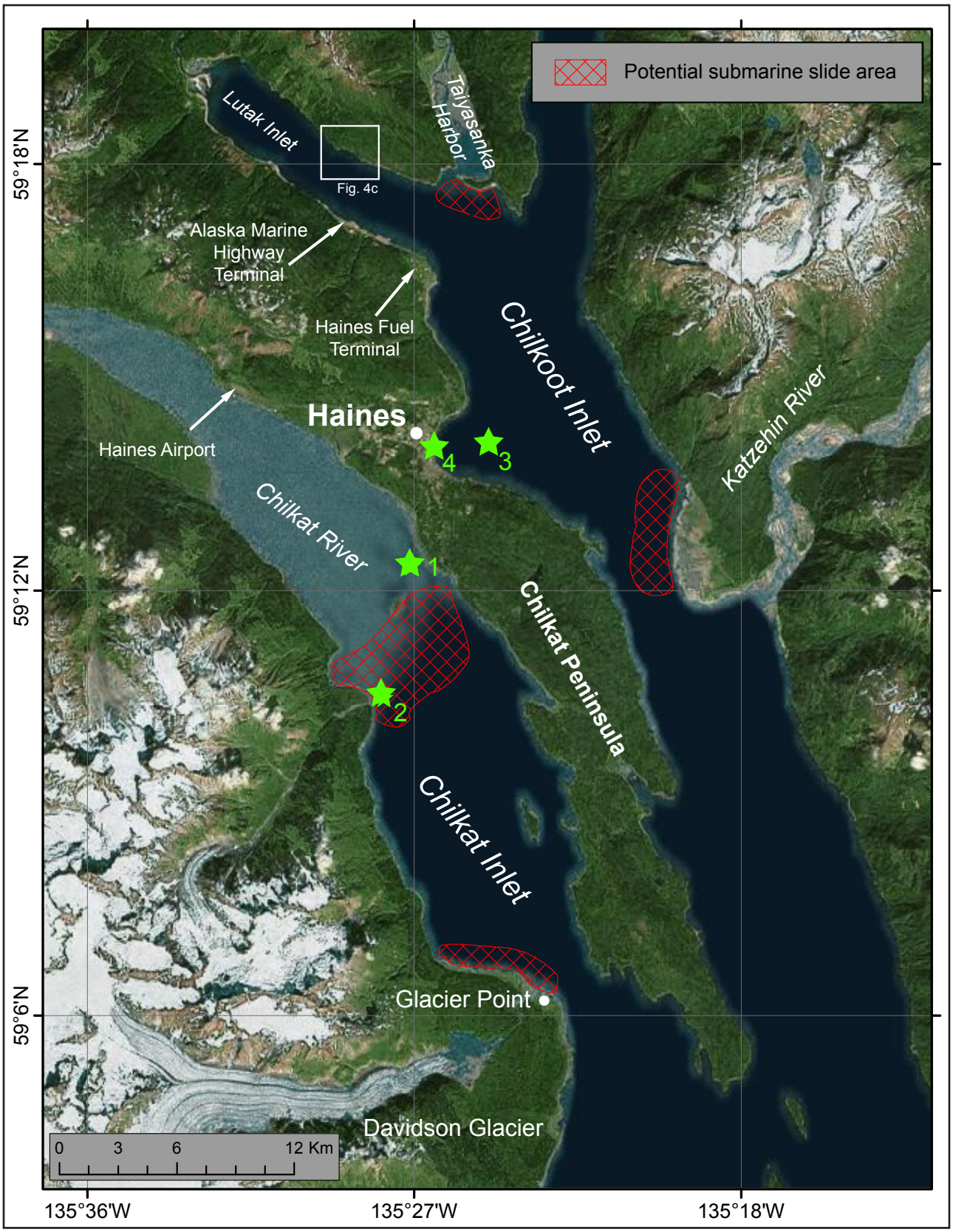

Figure 4B. Potential locations of underwater slides in the vicinity of Haines. Green stars indicate locations where tsunami wave dynamics were compared for the NHWAVE and FUNWAVE models. White rectangle outlines the area shown in figure 4C.

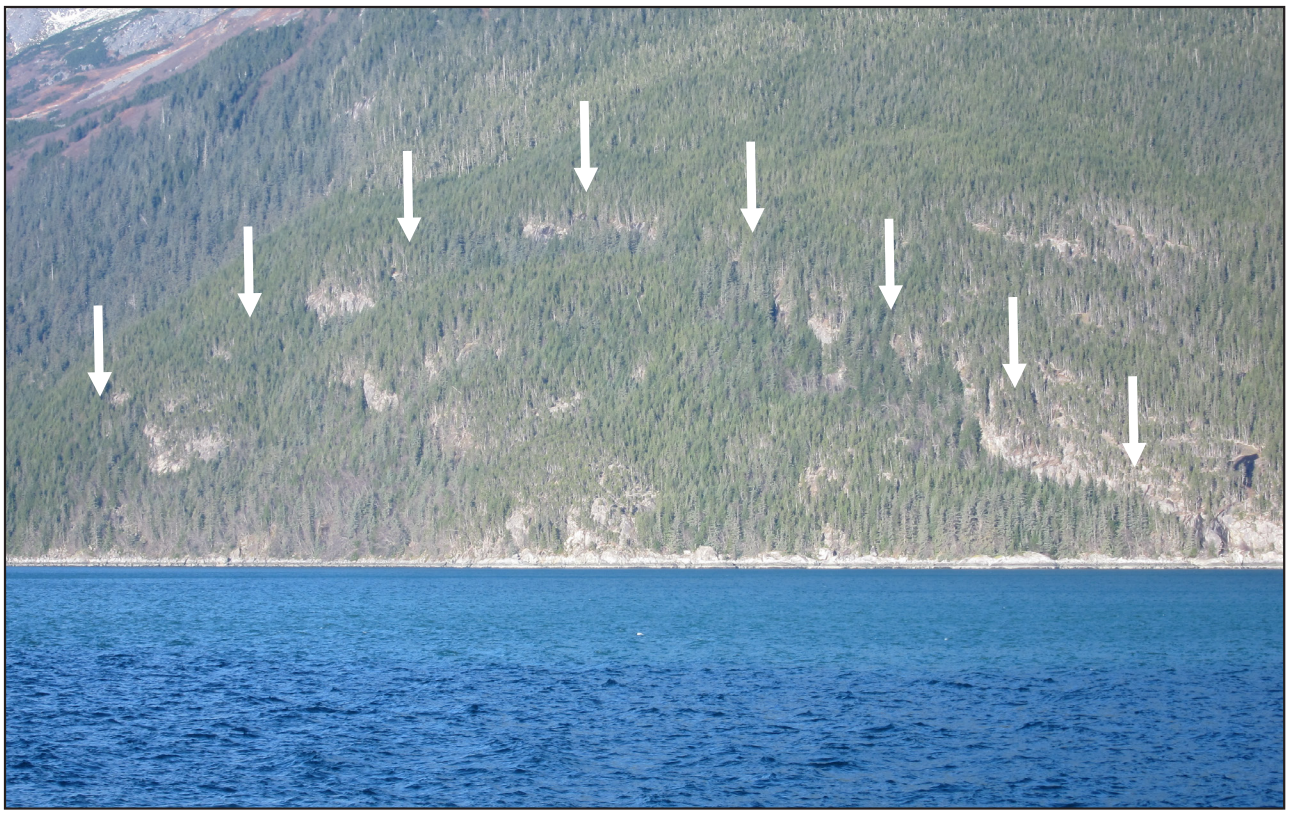

Figure 4C. A potentially unstable rock slump as seen from the Alaska Marine Highway Terminal in Lutak Inlet near Haines.

The horizontal datum for these grids is WGS84, and the vertical datum is Mean Higher High Water (MHHW). The spatial resolution of the high-resolution grids satisfies NOAA minimum recommended requirements for computation of tsunami inundation (NTHMP, 2010).

Numerical modeling of tsunami wave propagation and run-up

To model propagation of tectonic tsunamis from the Pacific Ocean to the communities of Skagway and Haines, we apply the numerical model developed by Nicolsky and others (2011b) and Nicolsky (2012) and used in previous Alaska tsunami inundation studies (Nicolsky and others, 2011a, 2013, 2014a, 2014b, 2015; Suleimani and others, 2010, 2013, 2015). This model currently has been validated through a set of analytical benchmarks and tested against laboratory and field data (Nicolsky and others, 2011b; Nicolsky, 2012). The model solves the nonlinear shallow-water equations with friction using a finite-difference method on a staggered grid with two-way nesting. For any coarse–fine pair of computational grids we apply a time-explicit numerical scheme as follows. First we compute the water flux in a coarse-resolution grid. These calculated flux values are used to define the water flux on a boundary of the fine-resolution grid. Next the water level and then the water flux are calculated over the fine-resolution grid. Finally the water level computed in the fine-resolution grid is used to define the water level in the area of the coarse-resolution grid that coincides with the fine grid. Subsequently we compute the water elevation for all other points in the coarse grid and proceed to the next time step. More details about the numerical scheme, grid nesting, and time stepping can be found in Goto and others (1997) and in Nicolsky and others (2011b). Even though the nested grids decrease the total number of grid cells needed to preserve computational accuracy in certain regions of interest, actual simulations are still unrealistic if parallel computing is not implemented. Here we use the

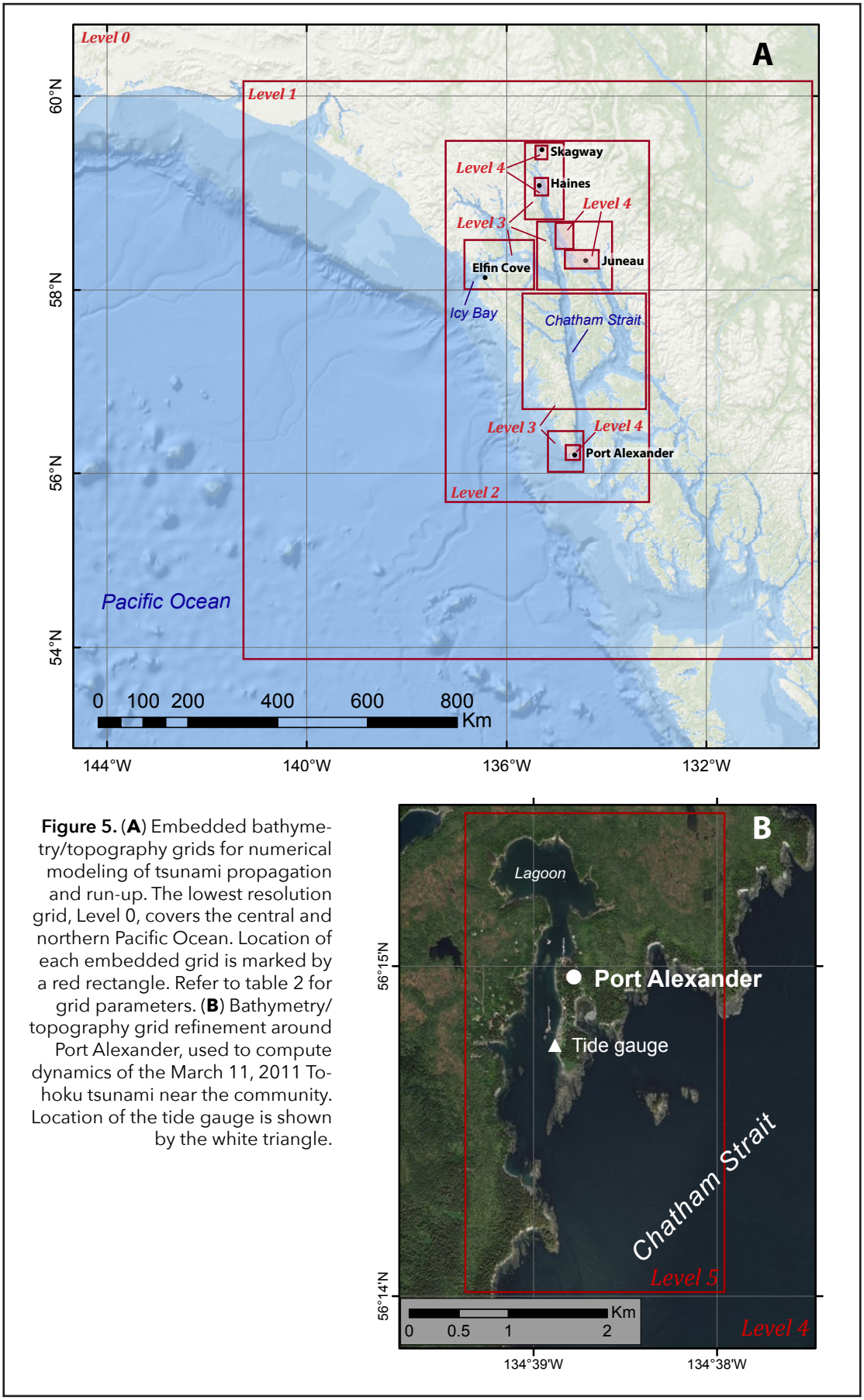

Figure 5. (**A**) Embedded bathymetry/topography grids for numerical modeling of tsunami propagation and run-up. The lowest resolution grid, Level 0, covers the central and northern Pacific Ocean. Location of each embedded grid is marked by a red rectangle. Refer to table 2 for grid parameters. (**B**) Bathymetry/topography grid refinement around Port Alexander, used to compute dynamics of the March 11, 2011 Tohoku tsunami near the community. Location of the tide gauge is shown by the white triangle.

Table 2. Nested grids used to compute propagation of tsunami waves generated in the Pacific Ocean to the communities of Skagway and Haines. High-resolution grids are used to compute the inundation. Note that the grid resolution in meters is not uniform and is used to illustrate grid fineness near the communities. Grids marked by asterisk (*) were used in the sensitivity study described in Nicolsky and others (2017). The first dimension is the longitudinal grid resolution, while the second is the latitudinal resolution.

Grid name	Resolution		Longitudinal boundaries	Latitudinal boundaries
	arc-seconds	Meters (near communities)		
Level 0, Northern Pacific	120″ × 120″	1,850 × 3,700	120°00′ E – 100°00′ W	10°00′00″ N – 65°00′00″ N
Level 1, Southeastern Alaska	24″ × 24″	402 × 740	130°00′ W – 141°00′ W	54°00′00″ N – 60°00′00″ N
Level 2, Juneau West	8″ × 8″	132 × 246	133°15′ W – 137°17′ W	55°44′00″ N – 59°33′00″ N
Level 3, Lynn Canal	2.7″ × 2.7″	42.2 × 82.2	133°55′04′′ W – 135°18′27′′W	58°02′21′′ N – 58°41′40′′ N
Level 3, Juneau	2.7″ × 2.7″	44 × 82	133°55′04′′W – 135°18′27′′W	58°02′21′′N – 58°41′40′′N
Level 3, Chatham Strait*	2.7″ × 2.7″	44 × 82	133°17′W – 135°41′W	56°45′00″ N – 58°00′00″ N
Level 3, Icy Bay*	2.7″ × 2.7″	44 × 82	135°20′51′′W – 136°53′57′′W	58°02′22′′N – 58°33′05′′N
Level 3, Port Alexander*	2.7″ × 2.7″	45 × 82	134°24′38′′W – 135°07′34′′W	56°00′34′′N – 56°28′39′′N
Level 4, Skagway high-resolution grid	0.9″ × 0.53″	13.9 × 16.4	135°22′27′′ W – 135°16′59′′W	58°17′28′′ N – 58°29′44′′ N
Level 4, Haines high-resolution grid	0.9″ × 0.53″	14 × 16.4	135°32′25′′ W – 135°23′41′′W	59°11′17′′ N – 58°17′28′′ N
Level 4, Juneau high-resolution grid*	0.9″ × 0.53″	14.4 × 16.4	134°18′04′′W – 134°47′28′′W	58°14′58′′N – 58°25′22′′N
Level 4, Tongass Forest high-resolution grid*	0.9″ × 0.53″	14.4 × 16.4	134°45′00′′W – 135°00′42′′W	58°25′31′′N – 58°41′25′′N
Level 4, Port Alexander high-resolution grid*	0.3″ × 0.18″	5.1 × 5.5	134°37′58′′W – 134°39′22′′W	56°14′02′′N – 56°15′29′′N

Portable, Extensible Toolkit for Scientific Computation (PETSC), which provides sets of tools for the parallel numerical solution of shallow-water equations (Balay and others, 2012). Each computational grid listed in table 2 can be subdivided among an arbitrary number of processors. The above-mentioned passing of information between the water flux and level is implemented efficiently using PETSc subroutines.

All hypothetical tsunami simulations are conducted using the bathymetric/topographic data corresponding to the MHHW tide level in Skagway and Haines. We assume that the initial displacement of the ocean surface is equal to the vertical displacement of the ocean floor induced by the earthquake rupture process. In the numerical simulations we used a constant Manning's roughness of 0.02. We do not account for the finite speed of the rupture propagation along the fault and we consider the ocean-bottom displacement to be instantaneous.

Modeling of the March 11, 2011, Tohoku tsunami

Before proceeding with hypothetical earthquake scenarios, we verify our tsunami model against the observed tsunami generated by the March 11, 2011, M_W 9.0 Tohoku earthquake in Japan. Among many reasons for model verification listed in Synolakis and others (2007), the one that has particular importance for distant tsunami events is ensuring the consistency of the DEM nesting.

The March 11, 2011, Tohoku tsunami resulted in 21 cm (8.3 in) water wave recorded by the NOAA tide gauge in Skagway (NCEI/WDS). The tsunami was also recorded at tide gauges in Elfin Cove, Port Alexander, and Juneau (fig. 5). The Tohoku tsunami did not result in significant waves in Southeast Alaska because the tsunami traveled a great distance from its source and waves were directed primarily to the northwest–toward the coast of Japan–and to the southeastern region of the Pacific Ocean (Tang and others, 2012). The 2011 Tohoku tsunami arrived at Skagway on the falling tide and the highest wave arrived on the rising tide; the tidal range was 3.9 m (12.8 ft) on March 11, 2011 (National Oceanic and Atmospheric Administration/National Ocean Service [NOAA/NOS], in progress; https://tidesandcurrents.noaa.gov/waterlevels.html?id=9452210).

Several slip distribution deformation models representing the slip distribution of the 2011 Tohoku earthquake were published after the event. Here, we apply the finite fault model III by Shao and others (2011). The resulting vertical seafloor deformation is illustrated in figure 6. Similar to Suleimani and others (2013) and Nicolsky and others (2015), we model the 2011 tsunami dynamics without considering tidal sea level change and all model runs are conducted using bathymetric data that correspond to the MHHW tide level, if not otherwise noted.

Analysis of the modeling data reveals that the simulated tsunami arrives sooner than the observed one. We apply a time correction of δT = 12 min to the Elfin Cove and Port Alexander time series and δT = 15 min to the Juneau and Skagway time series. Figure 7 shows a comparison between the observed wave histories and the calculated time series at the Elfin Cove, Port Alexander, Juneau, and Skagway tidal stations. The water level observations were processed to remove the tidal component. We observe a time shift between the computed and observed waves that is similar to the shift reported by Tang and others (2012). Tang and others (2012) did not use the tidal stations of Elfin Cove, Juneau, and Skagway in their analysis, but for the Yakutat station they applied a time correction of δT = 12 min. Systematic tsunami travel time delays (due to elasticity of the solid Earth, seawater compressibility, and variations of gravitational potential) occur in many numerical experiments (Watada and others, 2014).

The visual comparison between the computed and measured water-level dynamics at Elfin Cove (fig. 7A) shows that the model provides a good approximation to the recorded tsunami amplitudes for the first ten hours after the earthquake,

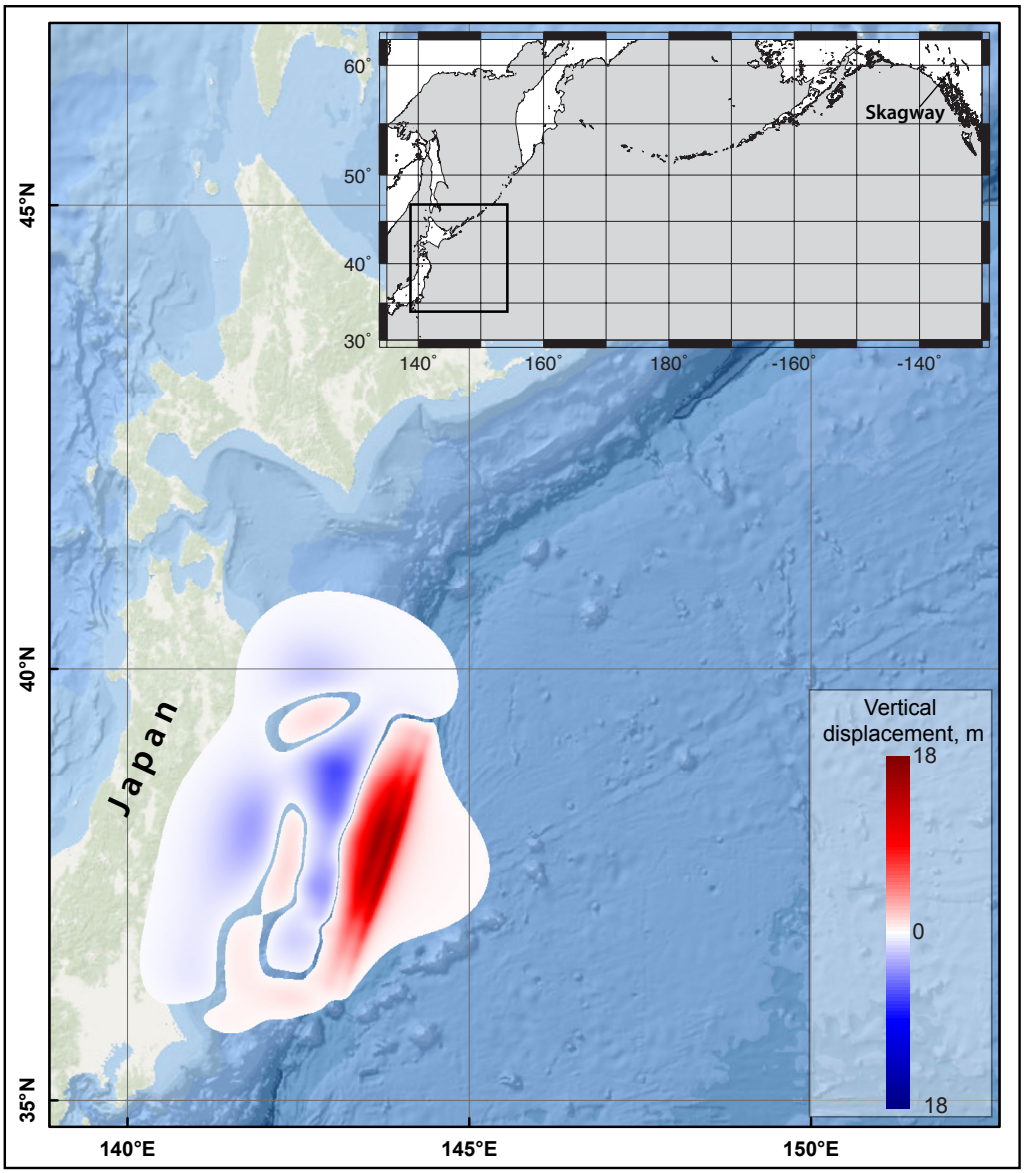

Figure 6. Vertical deformations of the ocean floor and adjacent coastal region corresponding to the March 11, 2011, Tohoku earthquake, based on a finite fault model by Shao and others (2011). Red indicates uplift; blue indicates subsidence. Inset map shows the location of the Tohoku earthquake source with respect to the Juneau tide gauge.

i.e., the modeled and observed waves arrive mostly in phase with each other and have similar amplitudes. After ten hours, phases of the modeled and observed waves start to differ and the comparison eventually degrades such that, by 20–24 hours after the earthquake, the observed and calculated waves are out of phase. The comparison between the first modeled and observed wave in Port Alexander (fig. 7B) is quite good except that the first wave is slightly underestimated, as is also the case for Elfin Cove. The underestimation at both tide gauges could be attributed, to a certain extent, to errors in the 2011 tsunami source model, discrepancies in the bathymetry, and to simplifications of the utilized numerical model.

We also note that tsunami dynamics in Port Alexander are characterized by 9-min oscillations, and the modeled range of water level variability is smaller than the observed range. The tide gauge at Port Alexander is at the mouth of the narrow and shallow channel connecting Chatham Strait to an inland lagoon (fig. 5B). The Tohoku tsunami arrived on the falling Southeast Alaska tide with a tidal range of ~3 m (~10 ft). The maximum waves in Port Alexander occurred when the tide was 2.0–2.5 m (6.6–8.2 ft) below the MHHW (National Oceanic and Atmospheric Administration/National Ocean Service [NOAA/NOS], in progress; https://tidesandcurrents.noaa.gov/waterlevels.html?id=9451054). Because our numerical model

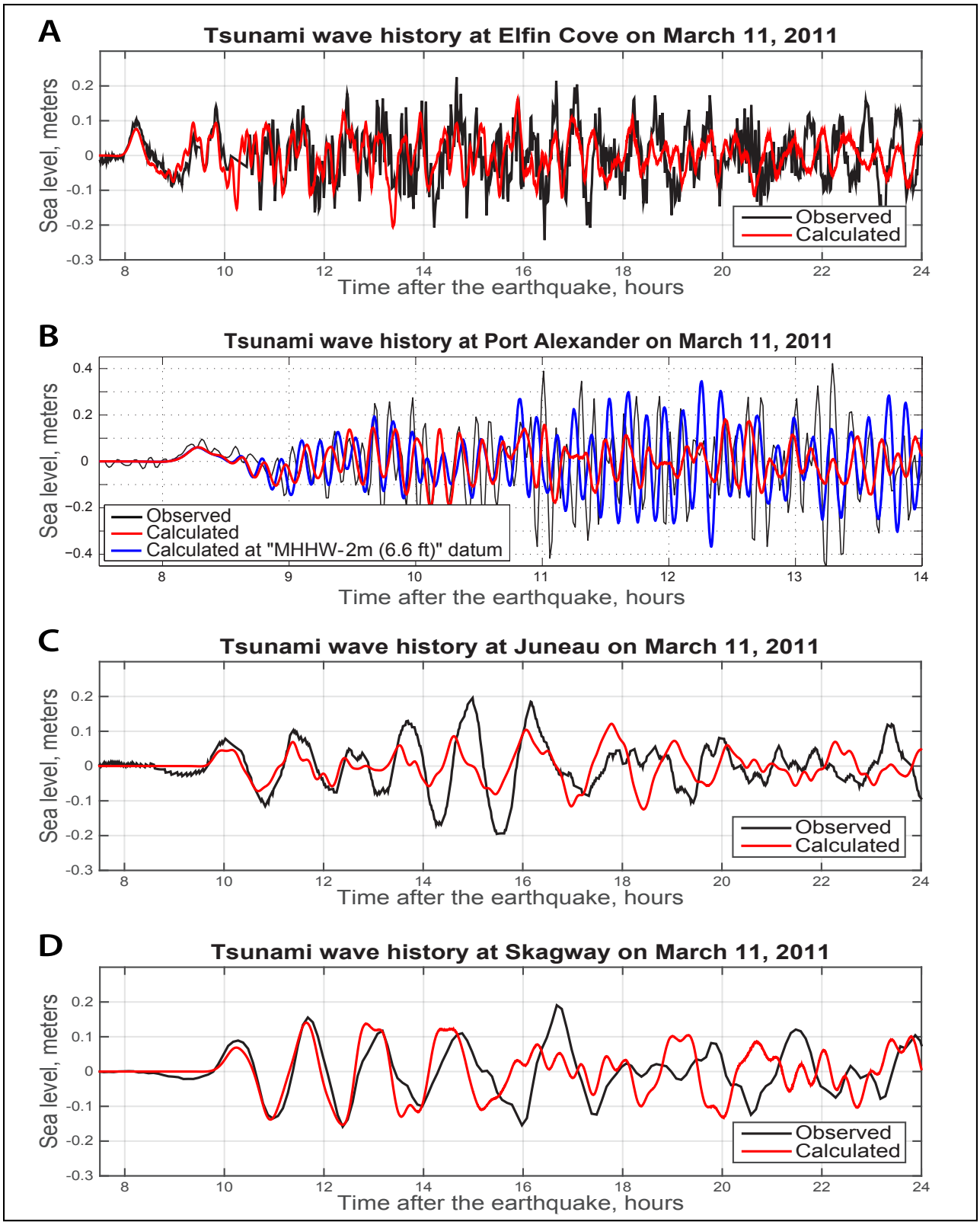

Figure 7. Observed and simulated water-level dynamics during the March 11, 2011, Tohoku tsunami at (**A**) Elfin Cove, (**B**) Port Alexander, (**C**) Juneau, and (**D**) Skagway tidal stations. All simulated are carried out while assuming that the still water level is at the MHHW level (no ocean tides in the model), except for the Port Alexander simulation. One of the simulations for Port Alexander was completed with the still water depth at 2 m (6.6 ft) below the MHHW level (blue line).

cannot simulate tidal dynamics, we simulate the 2011 tsunami with the water level corresponding to 2 m (7 ft) below the MHHW datum (fig. 7B). With these conditions, the channel connecting the lagoon to Chatham Strait is much shallower, if even existent, and thus less water can flow into the inland lagoon. Shallower conditions significantly increase the amplitude of modeled oscillations such that the new modeled results are comparable to the observations. We conclude that it is important to consider tides at Port Alexander because dynamic opening and closing of narrow, shallow channels has a significant impact on tsunami model accuracy.

For the inside locations of Juneau and Skagway, the numerical model accurately reproduces the first two (fig. 7C) and four waves (fig. 7D), respectively. For the subsequent waves the reproduction is not as good. The calculated highest wave at Skagway (fig. 7C) underestimates its recorded counterpart by ca. 50 percent. The discrepancy could be due to: a) effects of bottom friction; b) coarse resolution of intermediate grids describing the complex network of channels and passages that lead to Skagway from the Pacific coast; c) positive interference between various oscillation patterns in the fjord system; or d) tsunami-tide interactions. Nicolsky and others (2017) conducted a series of tests to determine which mechanisms are most likely responsible for wave height underestimation inside the network of passages and canals. Among the considered parameters, the tide level variations and the tidal dynamics, in general, have the greatest effect on the natural oscillation patterns of waves in Juneau and Skagway. Unfortunately, tide-tsunami coupling is a complicated problem (Kowalik and others, 2006; Kowalik and Proshutinsky, 2010) and its solution needs extensive exploration and validation before application in tsunami hazard assessments. Therefore, to account for the model's underestimation of the potential tsunami impact for Skagway, we numerically adjust the tsunami sources as discussed later in the report. However, a few studies have recently been performed that directly model dynamic tsunami-tide interactions, in particular in Columbia River (Tolkova, 2013; Tolkova and others, 2015; Yeh and others, 2012) and Hudson River (Shelby and others, 2016). These studies show tsunami amplification as a function of the tide, but with some site-specific effects–related both to the local geometry and the timing of tsunami waves–to their periods and also to the phase with which the tide enters the river. Similar future work related to tsunami–tide interactions in narrow fjords of coastal Alaska with large tidal amplitudes will be beneficial for Alaska tsunami hazard assessment.

Numerical model of landslide-generated tsunamis

In this report, we follow the methodology outlined in the tsunami hazard assessment report for the City of Juneau (Nicolsky and others, 2017). In particular, we use a numerical model by Kirby and others (2016) with two fully coupled components: a depth-integrated layer of Newtonian viscous fluid for the landslide model (Fine and others, 1998; Jiang and LeBlond, 1992) and the shock-capturing Non-Hydrostatic Wave (NHWAVE) model by Ma and others (2012). At some moment after the initial submarine landslide, the water level and water velocities (depth-averaged across all layers in NHWAVE) are used as initial conditions for the FUNWAVE-TVD model to simulate potential inundation over dry land at the 0.01 m (0.4 in) threshold between dry and wet cells. A similar two-stage approach is implemented to simulate inundation along the U.S. East Coast (Grilli and others, 2013) and the Gulf of Mexico (Lopez-Venegas and others, 2014) where the sliding area and the coast are not adjacent to each other. Further details regarding coupling and parameters used to simulate submarine landslide dynamics can be found in Nicolsky and others (2017). The cou-

pling of the NHWAVE and FUNWAVE-TVD models is illustrated later in this report for one of the hypothetical scenarios.

Modeling of waves generated by subaerial slides and rockfalls presents a major challenge. Subaerial landslides, unlike submarine ones, impact water bodies at high speeds and can cause larger tsunamis, given all other assumptions are the same. The impact of a rockfall on the water surface results in a turbulent splash and consequent mixing of the granular materials with water. Unfortunately, coupling of NHWAVE to the depth-integrated layer of Newtonian viscous fluid for the landslide model is not an optimal modeling approach to rockfalls or subaerial slides. Furthermore, due to insufficient data on the locations and volumes of hypothetical subaerial landslides, we do not model tsunamis generated by this type of landslide in this report.

Hypothetical tectonic tsunami sources

In this section, we consider several tectonic tsunami sources to develop tsunami hazard maps for the communities of Skagway and Haines. We follow the notations of Nishenko and Jacob (1990) for megathrust segmentation: Yakataga–Yakutat (YY), Prince William Sound (PWS), Kenai Peninsula (KP), Kodiak Island (KI), Semidi Islands (SEM), and Shumagin Islands (SH) (fig. 1).

The many islands, channels, and passages that characterize the landscape near Skagway and Haines may provide protection to the communities by dissipating tsunamis that hit the outer coast of southeastern Alaska. Conversely, the same passages may also serve as wave guides to channel tsunami energy. Analysis of available bathymetry charts shows that waves can reach Skagway and Haines primarily by two routes: from the west through Icy Strait or from the south through Chatham Strait, both of which connect to Lynn Canal (fig. 2A). In recently completed studies by Suleimani and others (2015, 2016) and Nicolsky and others (2017), tsunamis generated by earthquakes along the KI, KP, PWS, and YY segments are thought to be worst-case scenarios for Juneau and for the Icy Strait communities of Elfin Cove, Gustavus, and Hoonah. Because Skagway and Haines are located further inland along the same tsunami propagation route, in this report we consider the same tsunami scenarios. We also consider tsunamis propagating north through Chatham Strait and Stephens Passage generated by an earthquake in the Cascadia subduction zone along the Washington–Oregon coast.

To parameterize coseismic slip distributions for tectonic scenarios, we employ a discretization of the Alaska–Aleutian plate interface (Hayes and others, 2012) between the subducting and overriding plates. The interface is discretized into a set of 10–15 km-long (6–9 mi-long) rectangles with the upper and lower edge of each rectangle being coincident with 1-km (0.6 mi) depth contour of the interface. The value of slip is ascribed to each rectangle (subfault) and its contribution to the overall coseismic deformation is consequently computed by Okada (1985) formulae. The value of rake—the direction a hanging wall block moves during rupture—is assumed to be 90° in order to maximize coseismic deformation for the given slip. All contributions from subfaults are added together to derive the coseismic deformation associated with the considered scenario. The rigidity modulus is assumed to be constant 3.6×10^{10} N/m^2 and independent of depth.

As in previous investigations (Nicolsky and others, 2011a, 2017; Suleimani and others, 2015, 2016), we consider a repeat and three variations of the 1964 earthquake source model. Table 3 provides a summary of all tectonic scenarios considered in this report. All tectonic scenarios used to estimate tsunami inundation in Juneau (Nicolsky and others, 2017) are considered in this report.

Table 3. Hypothetical tectonic scenarios used to model tsunami run-up in Skagway and Haines. All tectonic scenarios used to estimate tsunami inundation in Juneau (Nicolsky and others, 2017) are listed below.

#	M_W	Description	Maximum slip, m (ft)	Average slip, m (ft)	Maximum subsidence, m (ft)	Maximum uplift, m (ft)
1	9.2	Repeat of the 1964 M_W 9.2 Alaska Earthquake	23 (75)	10 (33)	5.5 (18)	9 (30)
2	9.3	Earthquake modeling extension of the 1964 rupture to the YY segment	23 (75)	15(49)	5.5 (18)	9 (30)
3	9.2	Tohoku-type earthquake in the area of the 1964 rupture	37 (120)	9 (30)	4 (13)	14 (48)
4	9.2	Tohoku-type earthquake in the area of the 1964 rupture and YY segment	37 (120)	11 (34)	4.5 (15)	10 (33)
5	9.0	Tohoku-type earthquake across the Prince William Sound and Kenai Peninsula	44 (144)	22 (72)	8 (26)	14 (44)
6	9.0	Earthquake according to the SAFRR project	75 (245)	16 (52)	3 (9)	15 (49)
7	9.1	Earthquake in the Cascadia subduction zone along the British Columbia, Washington, Oregon, and northern California shore	45 (148)	36 (118)	8 (25)	11 (35)

Scenario 1. Repeat of the 1964 M_W 9.2 Alaska Earthquake (fig. 8A).

Over the last two decades, several models of coseismic deformation for the M_W 9.2 Great Alaska Earthquake were developed by Johnson and others (1996), Ichinose and others (2007), Suito and Freymueller (2009), and Suleimani (2011). Most of the difference between them is in distribution of the slip and extent of slip on splay faults along the Kenai Peninsula. Maximum slip across all sources is 23 m (75 ft); average slip is 10 m (33 ft).

We conduct numerical simulations for each of the above-mentioned coseismic deformation models. An envelope of the potential inundation extents among all of these models is used to define the hypothetical inundation according to this scenario.

In a paleoseismic study, Hamilton and Shennan (2005) evaluated the coseismic subsidence that occurred during the 1964 earthquake and two earlier events—900 and 1,500 years BP. It was shown that the earthquake dated to 1,500–1,400 years BP produced more than twice the subsidence caused by the 1964 earthquake. By comparing the Kenai Peninsula sites with other sites around Cook Inlet, the authors found that each of the three great earthquakes in the study had a different pattern of overall coseismic subsidence. In a subsequent study, Shennan and others (2008) present geologic evidence of six major prehistoric tsunamigenic earthquakes in the Kenai Peninsula area of south-central Alaska

in the past 4,000 years based on radiocarbon ages of tidal marsh deposits in Girdwood. They test the hypothesis that in some seismic cycles, the PWS, KK, KP, and YY megathrust segments can rupture simultaneously to produce earthquakes of greater magnitude than historical events. Their paper presents evidence that earthquakes approximately 900 and 1,500 years BP simultaneously ruptured three adjacent segments of the Aleutian megathrust: the PWS, KI, and YY segments. The rupture area of these earthquakes was estimated to be 23,000 km^2 (8,880 mi^2) greater than that of the M_W 9.2 Great Alaska Earthquake of 1964, and with a 15 percent larger seismic moment. Therefore, we constructed a hypothetical tsunami scenario based on the extended 1964 source.

Scenario 2. M_W 9.3 earthquake modeling extension of the 1964 rupture to the YY segment (fig. 8B).

We develop extensions of the four above-mentioned coseismic deformation models for the 1964 event by adding to each of them a coseismic deformation in the YY segment. The latter deformation is based on scenario 5 in Nicolsky and others (2013). We note that extensions of Johnson's and Suleimani's models were used as scenarios 1 and 2 by Suleimani and others (2013) to assess potential inundation in Sitka. Maximum slip across all sources is 22–23 m (72–75 ft); average slip is 13–15 m (43–49 ft).

We conduct numerical simulations for each of the considered coseismic deformation models. An envelope of potential inundation extents among all of these models is used to define the hypothetical inundation according to this scenario.

Following lessons learned from the 11 March 2011 M_W 9.0 Tohoku earthquake and tsunami (Ito and others, 2011), and given similarities between the Alaska and Tohoku subduction margins (Kirby and others, 2013; Ryan and others, 2012), we propose that a hypothetical rupture might propagate to shallow depths and produce a large amount of slip close to the trench (i.e., in the seafloor). Therefore, we also consider tsunami scenarios in the Gulf of Alaska (scenarios 3–5)—the most sensitive location for Southeast communities due to the directivity of the tsunami pattern.

Scenario 3. M_W 9.2 Tohoku-type earthquake in the area of the 1964 rupture (fig. 8C).

This scenario is the same as scenario 2 in Suleimani and others' (2015) tsunami modeling study for Elfin Cove, Gustavus, and Hoonah. Maximum slip is 37 m (120 ft); average slip is 9 m (30 ft).

Scenario 4. M_W 9.2 Tohoku-type earthquake in the area of the 1964 rupture and YY segment (fig. 8D).

This scenario is the same as scenario 4 in Suleimani and others' (2016) tsunami modeling study for Yakutat. Maximum slip is 37 m (120 ft); average slip is 11 m (36 ft).

Scenario 5. M_W 9.0 Tohoku-type earthquake across Prince William Sound and Kenai Peninsula (fig. 8E).

This scenario is the same as scenario 3 in Suleimani and others' (2015) tsunami modeling study for Elfin Cove, Gustavus, and Hoonah. Maximum slip is 44 m (144 ft); average slip is 22 m (72 ft).

We supplement the above sources with two additional scenarios. First, we consider a scenario developed by the USGS Science Application for Risk Reduction (SAFRR) project to describe the impacts to the coastline of southern California from a tsunami generated by an earthquake in the Alaska Peninsula region (Ross and others, 2013). Second, we consider a scenario along the Oregon-Washington coast; although a rupture of the Cascadia subduction zone is not a worst-case scenario for the Skagway and Haines areas, we simulate this large hypothetical earthquake along the western seaboard of the U.S. for the sake of completeness and community awareness.

Scenario 6. M_W 9.0 earthquake according to the SAFRR project (fig. 8F).

This scenario is the same as scenario 5 in Suleimani and others' (2015) tsunami modeling study for Elfin Cove, Gustavus, and Hoonah. Maximum slip is 75 m (246 ft); average slip is 16 m (52 ft).

Scenario 7. M_W 9.1 earthquake in the Cascadia subduction zone along the British Columbia, Washington, Oregon, and northern California shore (fig. 8G).

This scenario is the same as scenario 7 in Suleimani and others' (2015) tsunami modeling study for Elfin Cove, Gustavus, and Hoonah. Maximum slip is 45 m (148 ft); average slip is 36 m (118 ft).

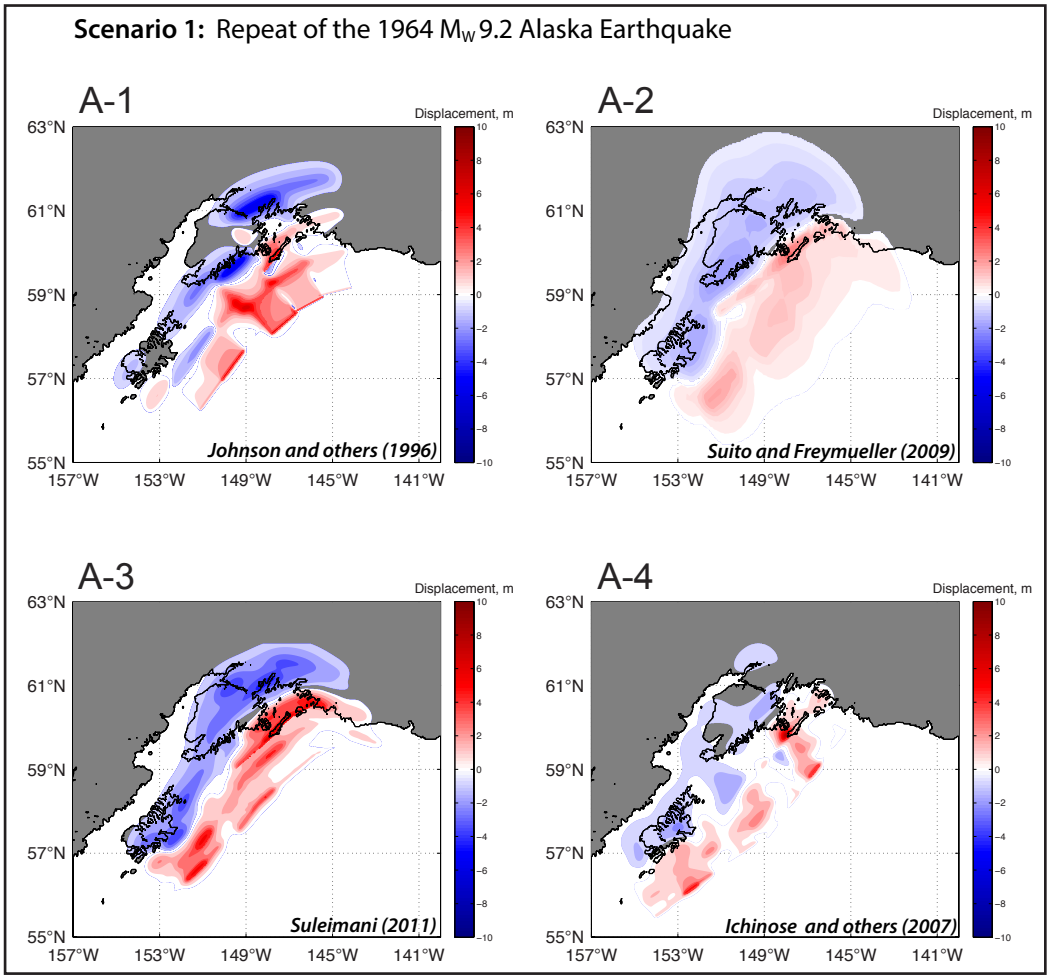

Figure 8A. Computed vertical ground-surface deformation related to tectonic scenario 1. Blue shaded areas are associated with coseismic ground subsidence; areas of uplift are shown in red.

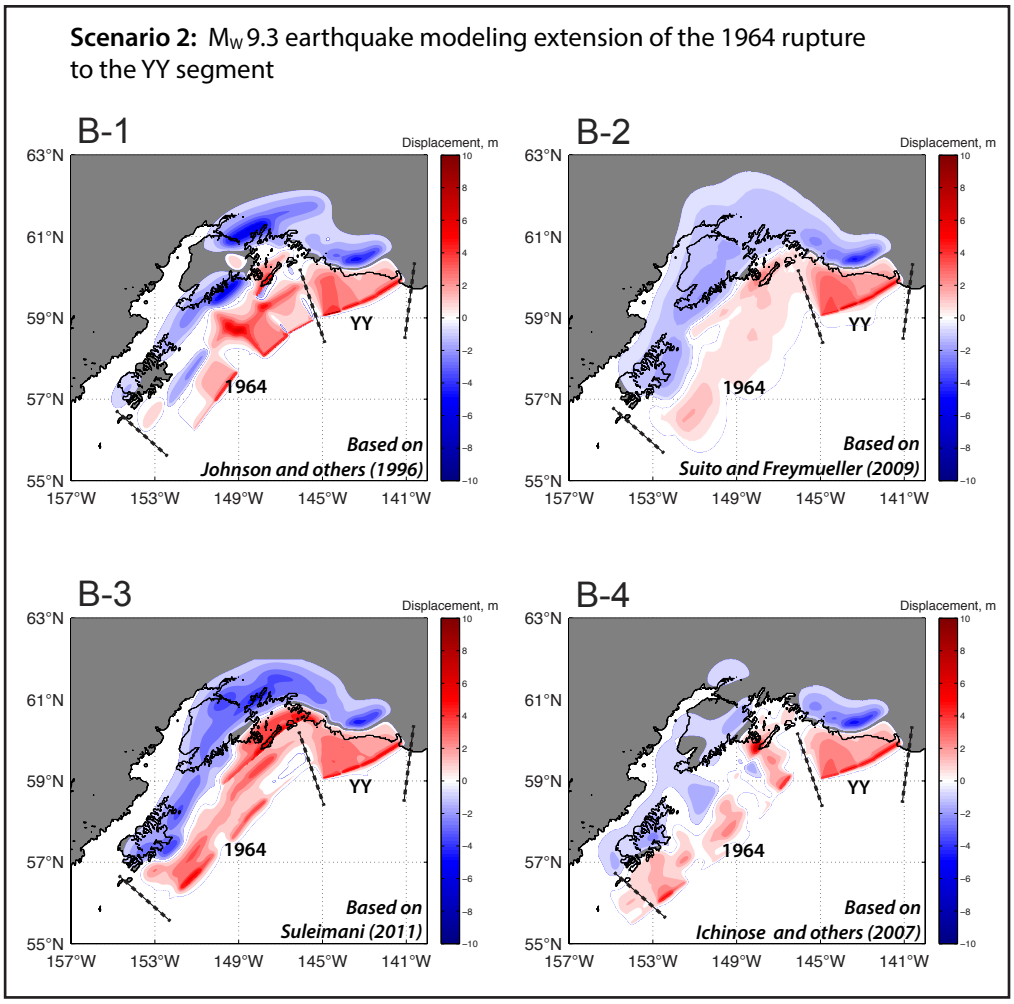

Figure 8B. Computed vertical ground-surface deformation related to tectonic scenario 2. Blue shaded areas are associated with coseismic ground subsidence; areas of uplift are shown in red.

Fortunately, the regions of the Aleutian megathrust that correspond to the aforementioned scenarios are about 1,000 km (620 mi) from the upper Lynn Canal, while the northern part of the Cascadia subduction zone source is about 1,200 km (750 mi) away. Therefore, all scenarios result in zero coseismic land level change in Skagway and Haines.

Hypothetical landslide tsunami sources

In addition to the hypothetical tectonic scenarios, we consider several submarine landslide scenarios that could generate hazardous waves along the Haines and Skagway waterfronts. Subaerial landslides are not considered in this report because of the significant uncertainties associated with specifying their potential locations and volumes.

Overviews of submarine landslides in waters close to Alaska are presented in several studies (Kulikov and others, 1998; Lee and others, 2006; Schwab and others, 1993). Additionally, after the 1964 earthquake, several geologic investigations were conducted in numerous locations around south-central and southeastern Alaska (Lemke, 1967; Plafker and others, 1969; Shannon and Hilts, 1973; Wilson and Tørum, 1968). One of the resounding conclusions from these studies is that the accumulation of loose deltaic sediment or artificial fill material on underwater slopes causes over-steepening of fjord walls and contributes directly to underwater slope instability. During an earthquake, dynamic forces imposed by seismic acceleration add to the gravitational force and triggers sliding of the unconsolidated sediments (Hampton and others, 2002). The major factors contributing to the total slide volume and extent are the intensity and duration of ground motion, configuration of underwater slopes, load of the

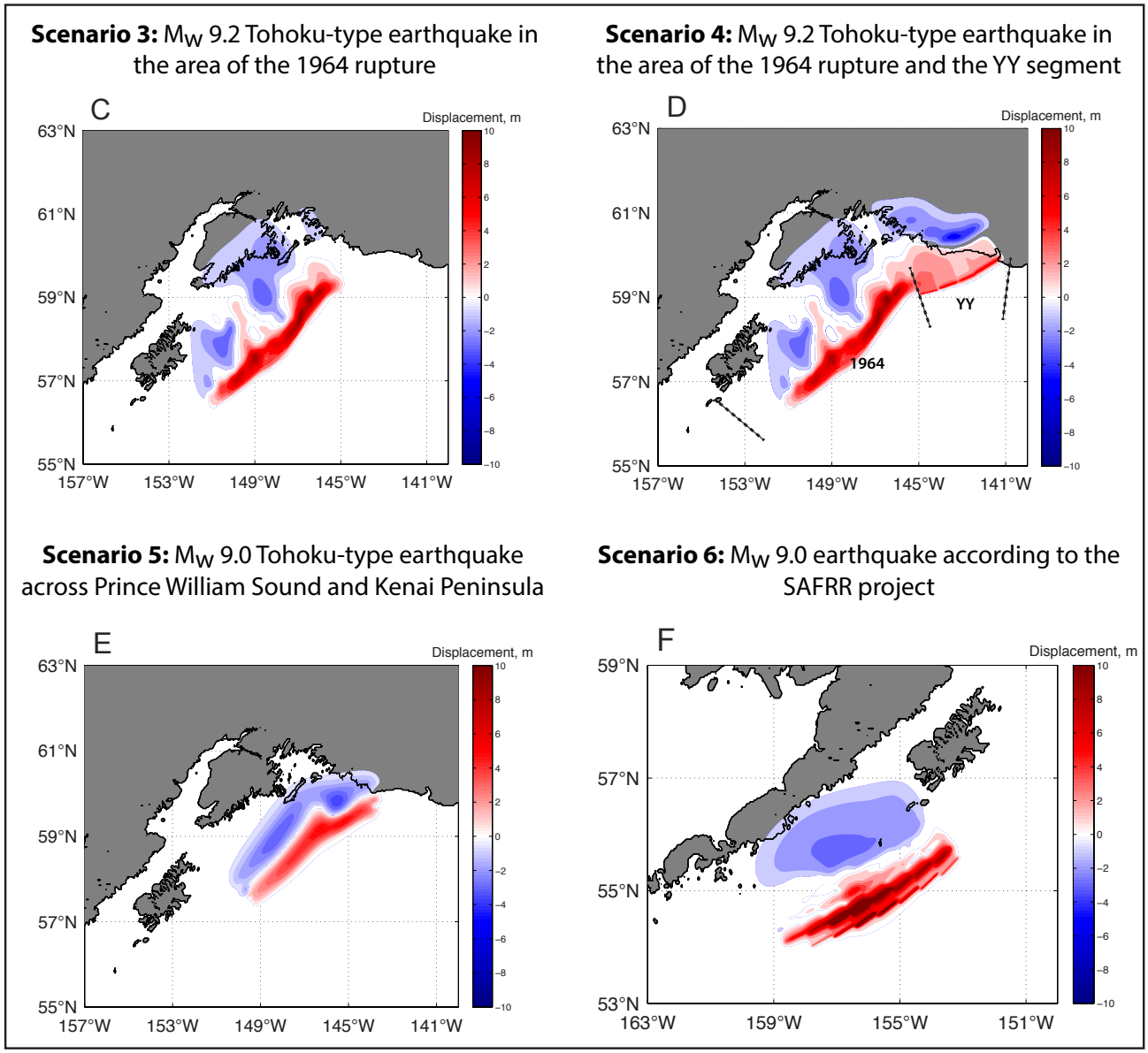

Figure 8C,D,E,F. Computed vertical ground-surface deformation related to tectonic scenarios 3-6. Blue shaded areas are associated with coseismic ground subsidence; areas of uplift are shown in red.

material (including natural and artificial fill, docks, etc.) above the water level, and type of sediment forming these slopes—unconsolidated or fine-grained materials are more prone to failure. Therefore, artificial fill areas and glacial creek deltas are especially susceptible to sliding and are considered as locations for potential landslides (Nicolsky and others, 2011a, 2013, 2017; Suleimani and others, 2010, 2015, 2016). Recall that multiple submarine landslides have caused cable breaks near Haines and Skagway (e.g., Lander, 1996, p. 58), with most of the breaks near the Katzehin River delta and in Taiya Inlet (fig. 3).

Because there is practically no geotechnical data for submarine sediments, we take a heuristic approach to developing a set of hypothetical landslide scenarios. First, we identify creek deltas and artificial fill areas near the community. Next, we assume generic, bowl-shaped failure surfaces in the underwater materials at the identified locations

Scenario 7: M_W 9.1 earthquake in the Cascadia subduction zone along the British Columbia, Washington, Oregon, and northern California shore

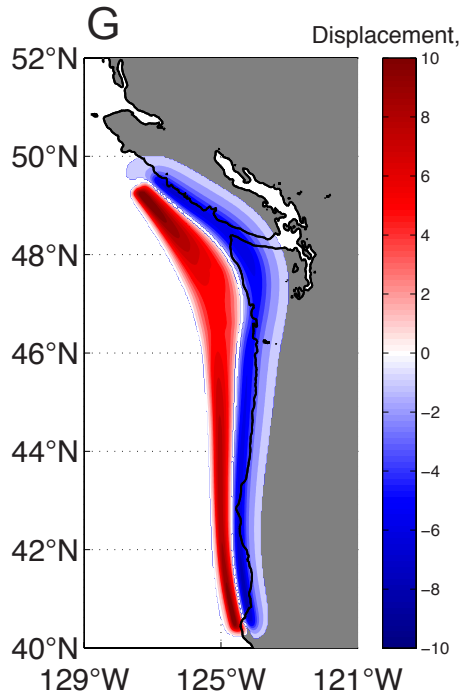

Figure 8G. Computed vertical ground-surface deformation related to tectonic scenario 7. Blue shaded areas are associated with coseismic ground subsidence; areas of uplift are shown in red.

based on the generic parameters (thicknesses and volumes) of landslides investigated after the 1964 earthquake, described below. Lastly, we differentiate between the modern bathymetry and failure surfaces to compute the thickness of a potential slide and its volume (Nicolsky and others, 2013, 2017; Suleimani and others, 2015, 2016).

Without geotechnical information we lack data to support alternative, more complicated slide plane geometries, but there are several well-studied submarine slides that occurred in Seward, Valdez, and Whittier after the 1964 earthquake. For example, several failures initiated along the fjord walls at relatively shallow depths in Seward (Haeussler and others, 2007; Lemke, 1967). The total volume of transported material was estimated to be 210 million m^3 (275 million yd^3) and the maximum slide thickness was about 60 m (200 ft). In Whittier, the maximum slide thickness along several transects in Passage Canal was similarly about 50–70 m (160–230 ft) (Kachadoorian, 1965, plate 3). Massive landslides also occurred in Valdez. Coulter and Migliaccio (1966, plate 2) estimated that approximately 75 million m^3 (98 million yd^3) of unconsolidated deposits were transferred from the Valdez waterfront into the bay, and the waterfront slide thickness was estimated at <100 m (<330 ft). Nicolsky and others (2013) revised the volume to be between 75 and 100 million m^3 (98 and 131 million yd^3). Therefore, we limit thickness of the hypothetical slides next to creeks and rivers in Haines and Skagway to 50–90 m (160–230 ft).

From a tsunami modeling perspective, an initial landmass failure on a fjord wall has much greater potential to produce a tsunami than the fjord-bottom material disturbed by the slide. Therefore, we place landslides near the shore in shallow water to increase their wave generation potential. Because both the slide volume and the initial acceleration are important parameters for the tsunami generation potential, we test the sensitivity of our model to these parameters later in the report.

We identified two potential slide areas in the vicinity of Skagway—at the mouths of Skagway and Taiya rivers (fig. 4A). A third location for a potential landslide in Skagway is along the railroad dock on the southeast bank of the harbor (fig. 4A). This is the site of a slide that occurred in 1994, thus this hypothetical scenario would reproduce the 1994 landslide-generated tsunami. A timeline of the events during this tsunami as well as observations of the wave level dynamics are summarized by Cornforth and Lowell (1996) and Rabinovich and others (1999). We do not consider this scenario and refer readers to consult the above-mentioned papers for details regarding the event.

Scenario 8. Underwater slide at the mouth of the Taiya River (TR slide, fig. 9A).

The head of Taiya Inlet is 3 km (2 mi) northwest of Skagway and is an estuary fed by the Taiya River carrying sediments from Alaska Boundary Range glaciers. A submarine landslide could potentially occur along the delta front, sending waves south along Taiya Inlet. We estimate a maximum hypothetical volume of 13 million m^3 (17 million yd^3) and a maximum thickness of 47 m (154 ft).

Scenario 9. Underwater slide offshore of the Skagway River (SR slide, fig. 9B).

Similar to the Taiya River, the Skagway River carries glacial sediments to the ocean. The Skagway River delta was the site of several previous cable breaks, likely indicating frequent underwater failures. Therefore, we hypothesize that the sediments offshore of the Skagway River delta could fail and slide into the bottom of the inlet. Volume of the maximum hypothetical slide is estimated to be 11 million m^3 (14 million yd^3), with a maximum thickness of 59 m (194 ft).

Finally, we also consider four potential slide areas in the vicinity of Haines—at the distal ends of deltas in Chilkat and Chilkoot inlets and at the glacier moraine in Taiyasanka Harbor (fig. 4B)

Scenario 10. Underwater slide offshore of the Glacier Point (GP slide, fig. 9C).

The Davidson Glacier originating in the Chilkat Range forms an extensive outwash plain and a semicircular alluvial fan protruding far offshore into Chilkat Inlet. Accumulation of sediment at the distal end of the fan creates the conditions for a potential submarine landslide. Waves generated at the northern segment of the fan, west of Glacier Point, will be directed toward the community of Haines. After specifying hypothetical failure surfaces for the GP slide, we assume that the slide volume is 65 million m^3 (85 million yd^3) and the maximum thickness is 89 m (290 ft).

In this report, we develop an envelope scenario along the head of Chilkat Inlet and estimate the volume for the hypothetical CR slide to be 160 million m^3 (210 million yd^3), with a maximum thickness of 54 m (177 ft). The difference in volume between this scenario and the one considered for the city of Valdez is due to the difference in width of the frontal area of the fjord. Note that the hypothetical CR slide is thinner than the one used for modeling a tsunami in Port Valdez.

Scenario 11. Underwater slide at the mouth of the Chilkat River (CR slide, fig. 9D).

Before discharging into the ocean, the Chilkat River forms an extensive delta with wide tidal flats at the head of Chilkat Inlet. Similar to the Lowe River in Valdez and Resurrection River in Seward, the deltas of which were locations of submarine landslides in 1964, the Chilkat River is a major carrier of glacial sediments into the fjord. For example, Nicolsky and others (2013, scenario 16-Envelope) hypothesized that a potential submarine landslide at the head of Port Valdez could be up to 85 m (280 ft) thick and reach up to 100 million m^3 (131 million yd^3) in volume.

Scenario 12. Underwater slide at the mouth of the Katzehin River (KR slide, fig. 9E).

Similar to the Glacier River, the Katzehin River carries sediments from the Mead Glacier to Chilkoot Inlet and also forms an extensive semicircular alluvial fan. Likewise, accumulation of sediments creates potential for a submarine landslide at the distal ends of the Katzehin River delta. See figure 3 for locations of multiple submarine cable failure offshore of the river delta. Waves generated at the northwestern segment of the fan will be primarily directed toward the community of Haines and its harbor. After specifying hypothetical failure surfaces for the KR slide, we assume that the slide volume is 78 million m^3 (102 million yd^3) and the maximum thickness is 62 m (203 ft).

Scenario 13. Underwater slide at the Taiyasanka Harbor moraine (TH slide, fig. 9F).

Strong ground shaking during the 1964 earthquake caused a massive slide at Shoup Bay moraine (Coulter and Migliaccio, 1966). Similar geological settings—a semicircular, partially eroded and breached glacial moraine—exist at the south end of Taiyasanka Harbor. We assume that sediment along the southern bank of the moraine can fail and generate waves directed towards the northern limits of the community. After specifying hypothetical failure surfaces for the TH slide, we estimate that the slide volume is 15 million m^3 (20 million yd^3) and the maximum thickness is 38 m (125 ft).

Slide volume and maximum slide thickness for each landslide scenario are summarized in table 4.

Table 4. Hypothetical landslide scenarios used to model potential extent of inundation by landslide-generated tsunamis in Skagway and Haines.

Scenario	Location of underwater slide	Maximum slide volume, million m^3 (yd^3)	Maximum slide thickness m (ft)
8	Offshore of Taiya River delta (Taiya River Slide)	13 (17)	47 (154)
9	Offshore of Skagway River delta (Skagway River Slide)	11 (14)	59 (193)
10	Glacier Point (Glacier Point Slide)	65 (85)	89 (292)
11	Offshore of Chilkat River delta (Chilkat River Slide)	160 (210)	54 (177)
12	Offshore of Katzehin River delta (Katzehin River Slide)	78 (100)	62 (203)
13	Taiyasanka Harbor Moraine (Taiyasanka Harbor Slide)	15 (20)	38 (125)

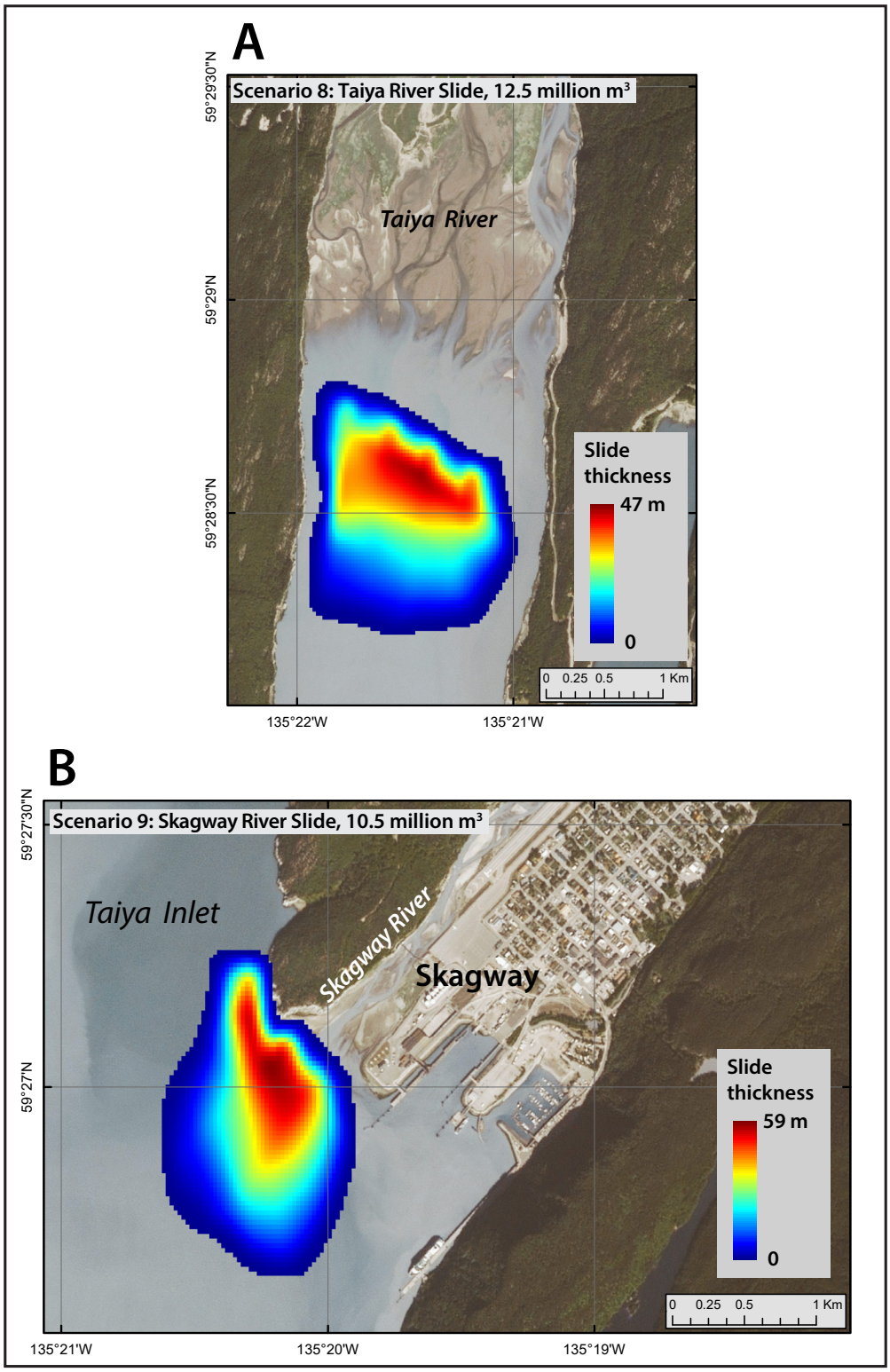

Figure 9A,B. Locations and initial landslide thicknesses for scenarios 8 and 9.

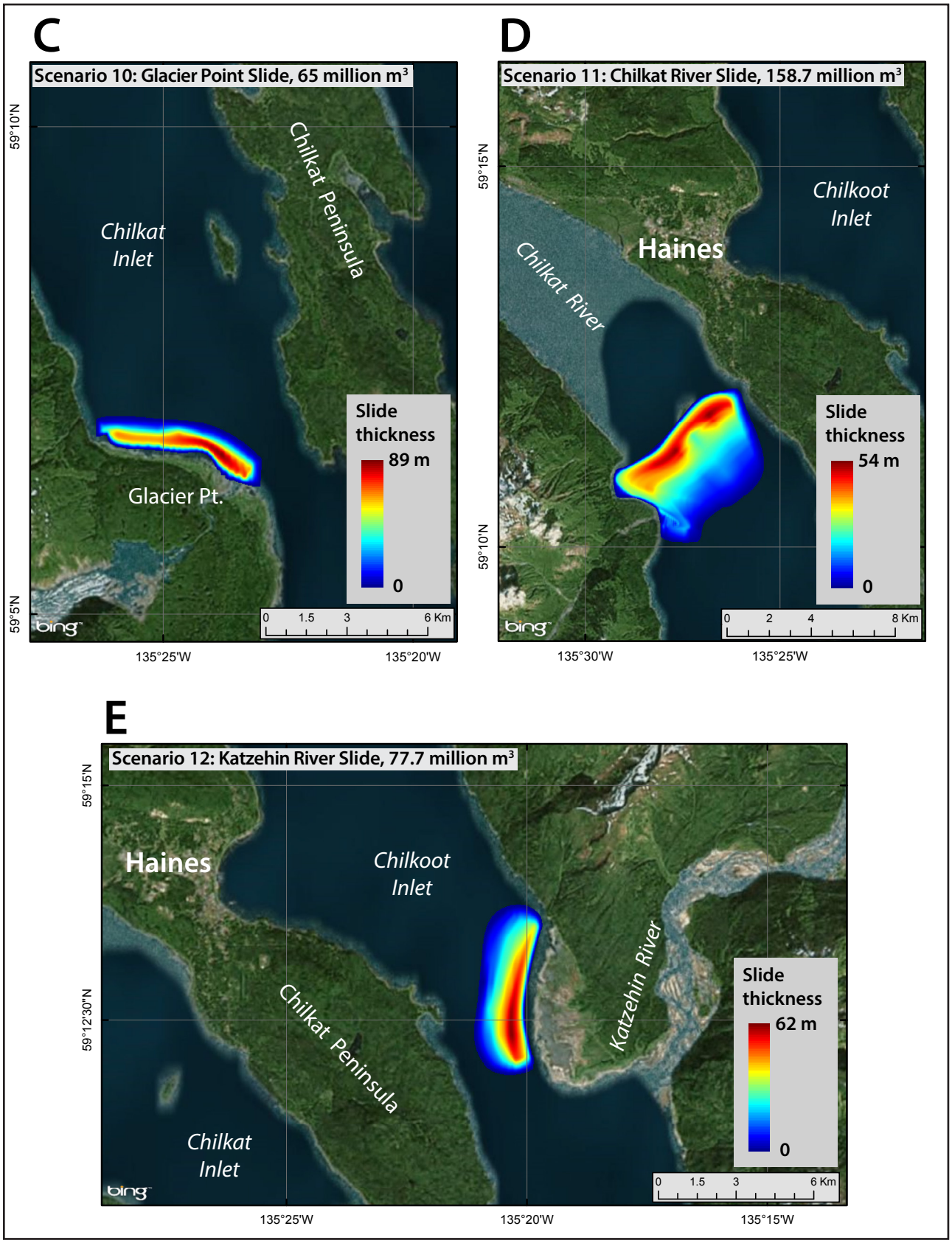

Figure 9C–E. Locations and initial landslide thicknesses for scenarios 10–12.

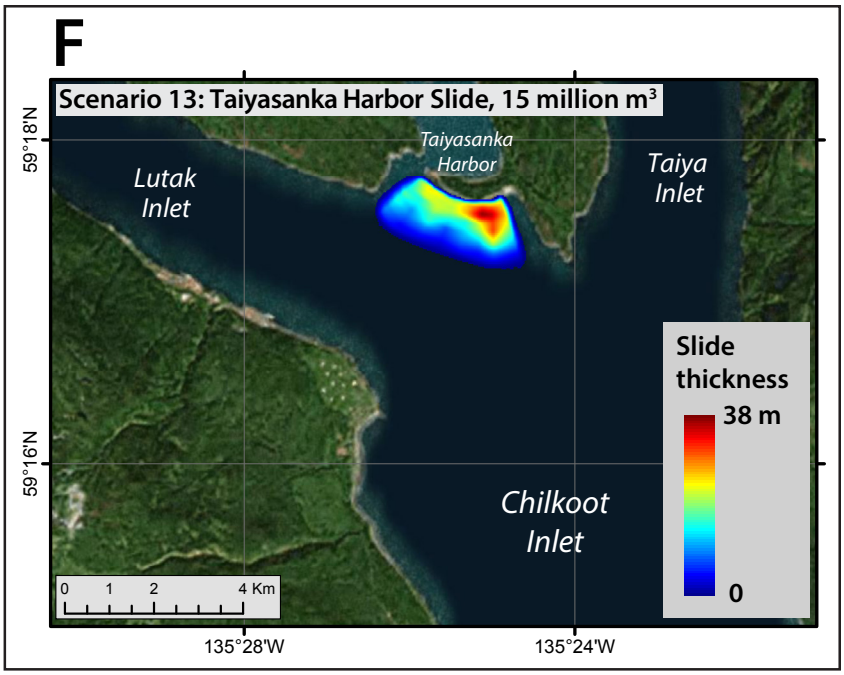

Figure 9F. Locations and initial landslide thicknesses for scenario 13.

MODELING RESULTS

We performed numerical calculations for 13 scenarios that include both earthquake- and landslide-generated tsunamis. For tectonic tsunami scenarios, we modeled water dynamics in each grid listed in table 2 without an asterisk (*). For scenarios related to landslide-generated tsunamis, we simulated water dynamics and computed runup only for the high-resolution grids. The extent of inundation is only computed for the high-resolution grids. To visualize different effects of earthquake- and landslide-generated waves in the vicinity of Skagway and Haines, we separately plot maximum wave heights for each tectonic scenario and maximum composite wave heights for all landslide scenarios.

Tectonic scenarios

Numerical experiments indicate that tsunamis generated by a potential earthquake rupture in the Gulf of Alaska region can reach Skagway and Haines in about three hours after the earthquake. However, the first wave might not be the highest wave, as was the case during the 2011 Tohoku tsunami. To assess the potential impact of seven different tectonic tsunami scenarios, we simulate wave heights at several locations. Computer experiments reveal that tectonic scenarios 3, 4, and 7 produce the maximum wave heights near Skagway and Haines. These three scenarios describe Tohoku-type ruptures in the Gulf of Alaska region and a rupture of the Cascadia subduction zone, respectively. To illustrate the modeled tsunami dynamics according to these scenarios, we select two locations (shown in figure A1): the Skagway tidal gauge (point 1), and the ore dock (Point 7). The computed water level dynamics for both are shown in figure 10. For both locations, scenario 4—the multi-segment Tohoku-type earthquake in the Gulf of Alaska—results in the highest modeled wave.

Scenario 4M

Numerical modeling of the 2011 Tohoku tsunami demonstrated that the tsunami wave amplitude at Skagway could be underestimated by a factor of 1.5 even with good correlation between observed and modeled waveforms at other locations in the same region (fig. 7). As conjectured, the tsunami-tide interaction might be responsible for the underestimation of modeled tsunami height in Skagway. Thus, in order to produce a maximum potential estimate of inundation that compensates for the underestimation of modeled wave height, we generated an additional scenario (scenario 4M) as described below.

We compensate for the fact that our model underestimates maximum tectonic tsunami height by increasing the coseismic slip of scenario 4—the scenario which resulted in the highest wave. Because propagation of tsunamis in the open ocean and deep fjords is assumed to be a linear process, we can adjust the modeled wave amplitude in Skagway simply by increasing the coseismic slip by a factor of 1.5. We emphasize that this "additional earthquake slip" scenario is a numerical solution to the underestimation of tsunami height in Skagway (due to complex tsunami-tide interactions that are beyond the scope of current tsunami modeling capabilities). The effective slip (multiplied by a factor of 1.5) should not be considered from a geophysical point of view, but rather as an adjustment to our numerical model because we know that it provides underestimations of tsunamis in Haines and Skagway. Thus, scenario 4M is a hypothetical tsunami that could be generated by a conjectural earthquake of scenario 4 with adjusted coseismic slip (the letter "M" stands for the modified slip in the scenario).

Scenario 4M. M_W 9.3 Tohoku-type earthquake in the area of the 1964 rupture and YY segment, with modified slip. This scenario is the same as scenario 4, but with the coseismic slip increased by a factor of 1.5 to compensate for the underestimation of tsunami height in Skagway. Maximum slip is 55.5 m (182 ft); average slip is 16.5 m (54 ft).

Scenario 1M

The available geologic evidence suggests that repeated 1964-type events (scenario 1) may occur more frequently throughout repeated seismic cycles (several thousands of years) than scenario 4. Thus, scenario 1 is also a credible estimate of a future earthquake in the Gulf of Alaska—albeit not as severe as scenario 4—that we consider here. Thus, just as we modified scenario 4, we modify scenario 1 to account for the underestimation of the modeled tsunami, resulting in scenario 1M. We first adjust the coseismic slip for all four components (figs. 8A-1 through 8A-4) of scenario 1 and then model the resulting composite inundation in the communities.

Scenario 1M. Repeat of the 1964 M_W 9.2 Alaska Earthquake, with modified slip. This scenario is the same as scenario 1, but with the coseismic slip increased by a factor of 1.5 for all four sub-scenarios to compensate for the underestimation of tsunami height in Skagway. Maximum slip across all sources is 34.5 m (113.2 ft); average slip is 15 m (49.2 ft).

The modeling results indicate that the highest waves according to Johnson and others (1996) and Suleimani (2011) are almost the same and are the highest of the four models. The maximum modeled wave height according to these two models is about 1.8 m (5.9 ft) at the Skagway tide gauge (fig. A2). The 1964 tsunami arrived at Skagway on a rising tide and the total height was estimated to be about 5 m (16 ft) (Lander, 1996). The tide was about 3.5 m (11.5 ft) at the time of the tsunami arrival (National Oceanic and Atmospheric Administration/National Ocean Service [NOAA/NOS], in progress; https://tidesandcurrents.noaa.gov/waterlevels.html?id=9452400). Therefore, the first wave that arrived at Skagway after the 1964 earthquake was about 1.5 m (5 ft). The modeled first wave at Skagway according to scenario 1M is 1.2 m (4 ft), which correlates well with historical observations and corroborates the adjusted slip of scenario 1M.

Figures 11 and 12 show maximum tectonic tsunami heights above MHHW (scenario 4M) in

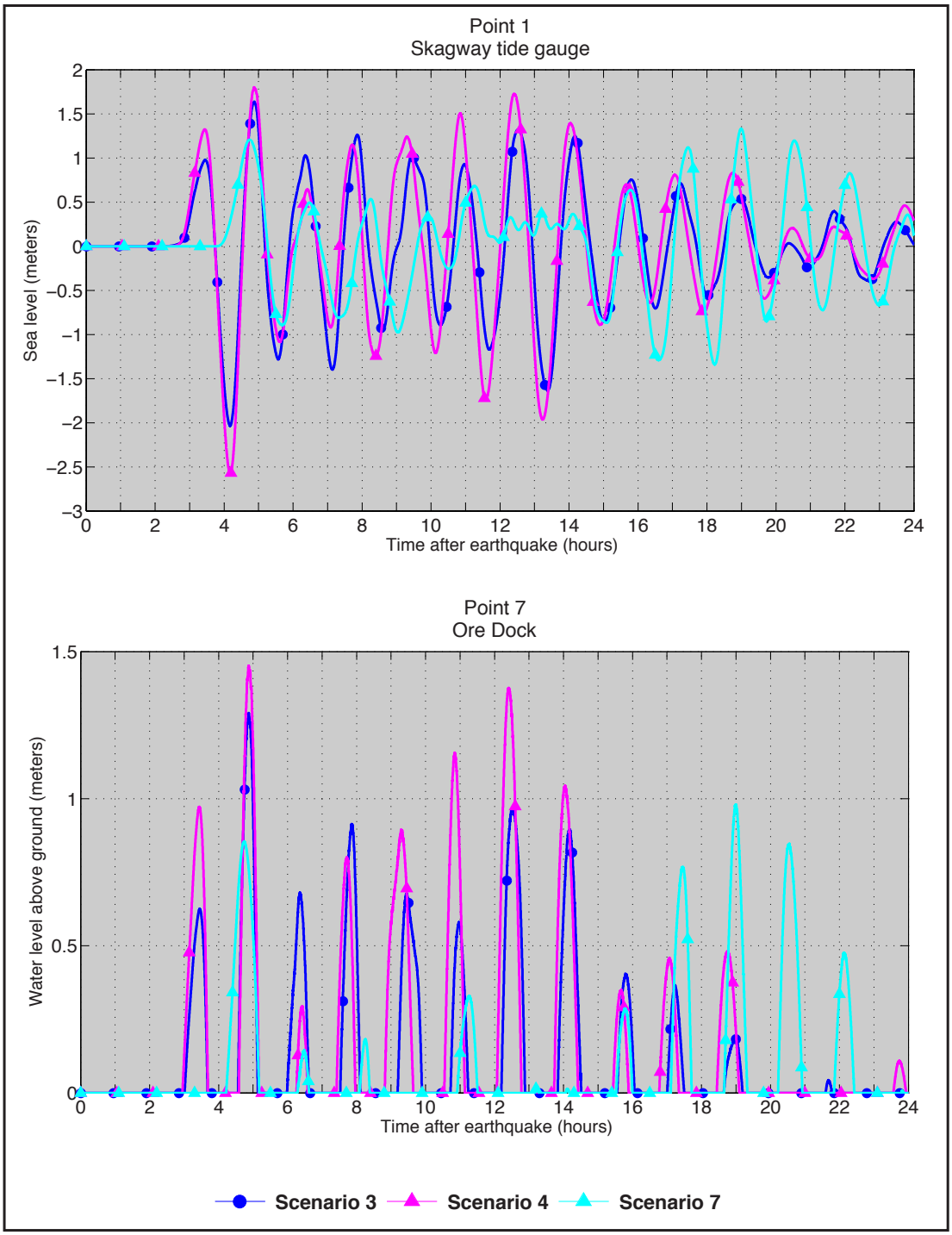

Figure 10. Simulated water-level dynamics at three locations in the vicinity of Skagway (locations on fig. A-1) for selected scenarios that have the highest potential to produce the maximum wave near Skagway and Haines.

Skagway and Haines, respectively. In both figures, we also delineate the modeled inundation extents according to scenarios 1M and 4. Tsunami flow depth over dry land is another important indicator of potential damage. Thus, in addition to the computed maximum tsunami heights, figure 13 shows the flow depths in Skagway according to scenario 4M, our worst case tectonic scenario. Figure 13 also shows the calculated envelope of the inundation extents of the four models of a repeat of the

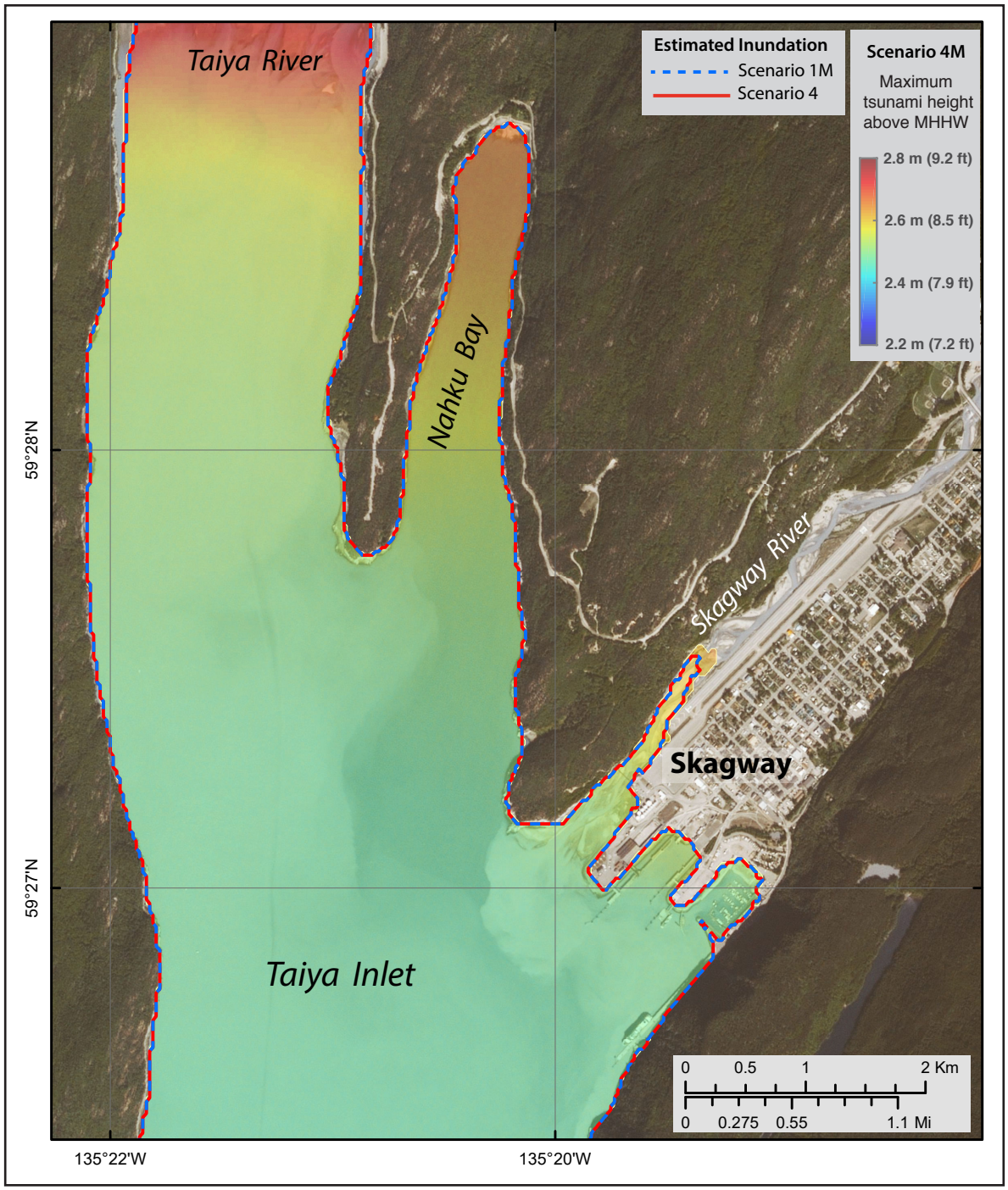

Figure 11. Maximum water level above MHHW for maximum credible tectonic scenario 4M in the upper Taiya Inlet and around Skagway. Modeling results for scenario 4M assume the effective slip parameterization compensates for the tsunami-tide interactions. Also shown are maximum water levels for scenarios 1M and 4.

1964 event (scenario 1M) and the modeled extent of potential inundation according to scenario 4, which are identical. All tectonic scenarios result in minimal inundation in Haines, therefore we do not provide a plot of maximum flow depths for Haines.

Modeling results suggest that scenarios 1M, 4, and 4M produce almost identical inundation in both Skagway and Haines. In Skagway, the inundation extents differ only along the bed of Skagway River, where inundation due to scenario

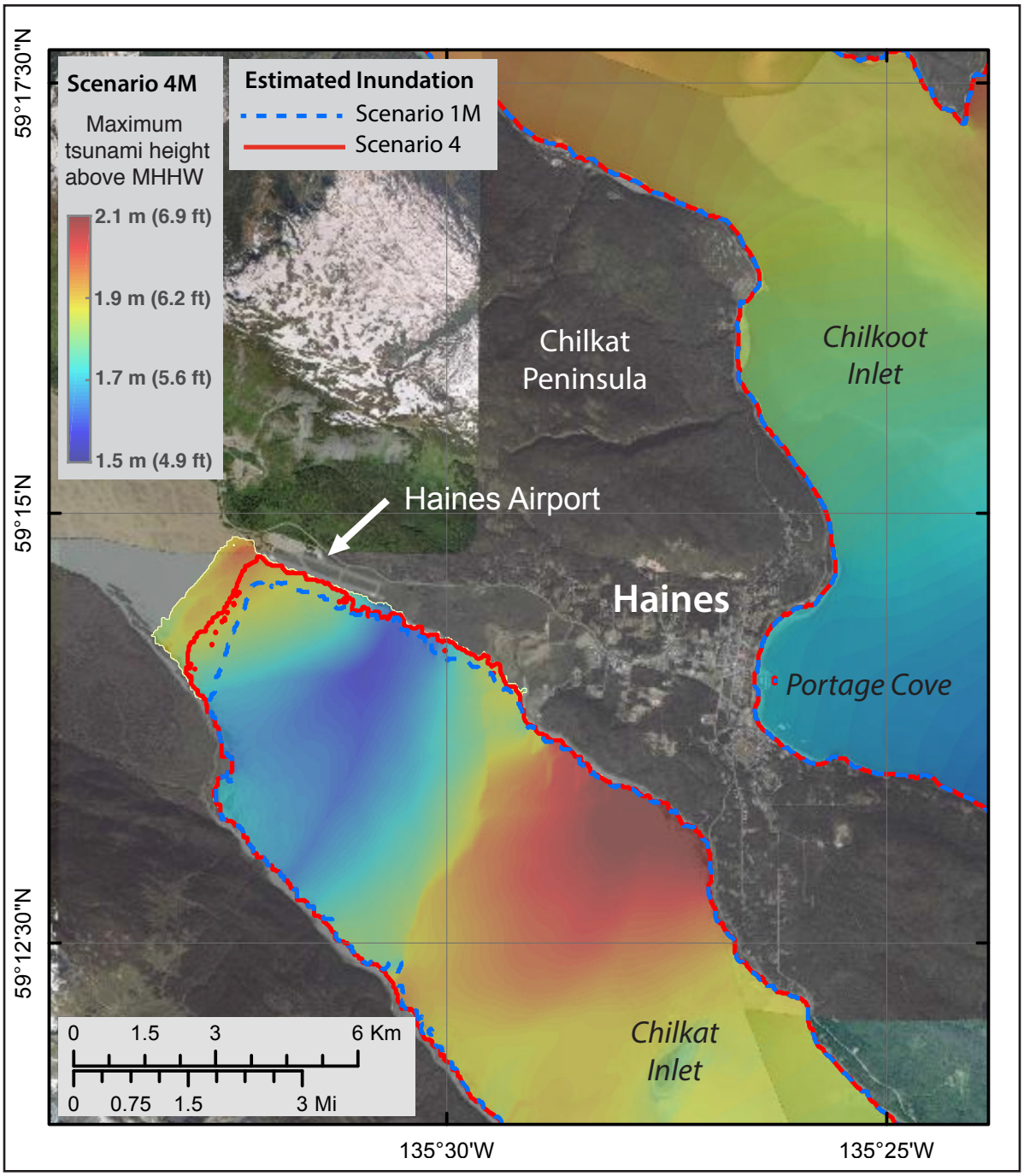

Figure 12. Maximum water level above MHHW for maximum credible tectonic scenario 4M around Haines. Modeling results for scenario 4M assume the effective slip parameterization compensates for the tsunami-tide interactions. Also shown are maximum water levels for scenarios 1M and 4.

4M extends farther upstream (fig. 11). The highest waves, up to 2.7 m (8.9 ft), occur in upper Taiya Inlet and in upper Nahku Bay, and the wave heights are uniform everywhere else in Taiya Inlet with slight increase in the Skagway harbor and along the bed of Skagway River. All three scenarios result in a similar amount of inundation in the Skagway waterfront area.

In Haines, the difference in the area of inundation for scenarios 1M, 4, and 4M exists only at the top of Chilkat Inlet, but none of the scenarios

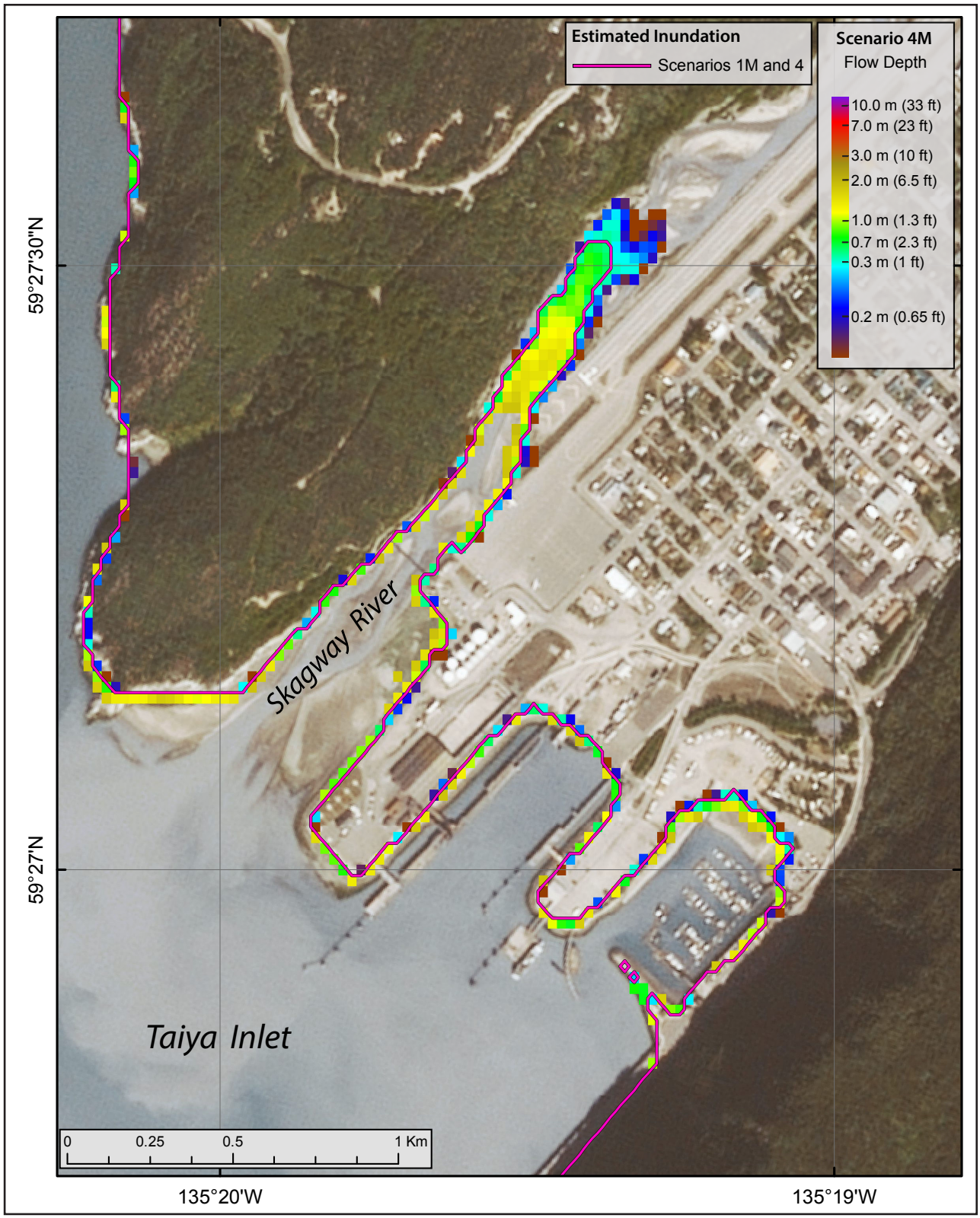

Figure 13. Modeled maximum water flow depth for maximum credible event (scenario 4M) and the modeled extent of potential inundation for repeat of the 1964 event (scenario 1M) at Skagway. Modeling results for scenarios 1M and 4M assume the effective slip parameterization compensates for the tsunami-tide interactions.

result in the inundation of the Haines airport (fig. 12). The highest waves, up to 2.0 m (6.6 ft), occur along the eastern shore of Chilkat Inlet, but do not result in inundation of this section of the mostly uninhabited shoreline either. The hypothetical extent of the inundation according to the modified 1964 event (scenario 1M) is less than that for the Tohoku-type rupture in the Gulf of Alaska (scenario 4). For all cases, the inundation of the town is minimal.

Submarine landslide scenarios

While tectonically generated waves may not inundate the coast for hours after an earthquake, landslide-generated waves could hit low-lying areas while the ground is still shaking (Coulter and Migliaccio, 1966; Wilson and Tørum, 1968). Additionally, some landslide-generated waves can occur without an earthquake and therefore without any warning. In this section, we present some details used to estimate the extent of inundation for the hypothetical landslide scenarios. More details regarding the modeling technique can be found in Nicolsky and others (2017).

We assume that slide-prone unconsolidated deposits are initially at rest and ground shaking triggers the slide; the extents of the slides are shown by the cross-hatched red polygons in figure 4. First, we simulate wave generation caused by the motion of a viscous landslide down the fjord slope using NHWAVE—the fully coupled model (Kirby and others, 2016). At the beginning of each numerical experiment, when the submarine slide initially propagates down the fjord wall, it pushes water and creates a positive wave propagating away from the slide. Behind, at the original slide location, an initial water surface depression occurs and is consequently filled with water under the restoring force of gravity. The wave radiation patterns created by slide dynamics are complex and usually include a series of crests and troughs radiating away from the slide area. We refer to Løvholt and others (2015) for an in-depth description of landslide tsunami generation. When the slide reaches a fjord bottom, most of its energy has already been transferred to the water. At this moment, execution of the fully coupled model is terminated. The resultant water level and the water velocities (depth-averaged across all layers in NHWAVE) are used as initial conditions for the FUNWAVE model. FUNWAVE then models inundation of the dry land. The extent of potential inundation from the landslide scenario encompasses the total inundation extent of the NHWAVE and FUNWAVE models.

Because there is uncertainty in choosing the exact moment at which to transition from the NHWAVE to FUNWAVE model, we transfer NHWAVE conditions (water levels and velocities) from two different time steps into the FUNWAVE model (figures 14 and 15). In addition to running both FUNWAVE scenarios to completion, we also run the initial NHWAVE model beyond the transition points and compare results from all three to assess model uncertainties. We compare the inter-model water levels at two locations near Skagway and four locations near Haines (figures 4A and 4B, respectively). Note for some slides there is only one FUNWAVE simulation, and modeling results for the Taiyasanka Harbor slide, scenario 13, are omitted for the sake of brevity. Despite minor differences between individual models, the amplitudes and periods of the waveforms are grossly in agreement. Moreover, the coupling between two FUNWAVE outputs is stable, as the results are not greatly affected by the time step at which we transition from NHWAVE to FUNWAVE.

Modeling results are conjectures about the actual landslide-generated tsunami dynamics. Recall that the initial landslide volumes (fig. 9) are defined by idealized failure surfaces and are modeled as viscous fluids; hence changes to landslide geometries, assumed rheologies, or other model parameters could affect the difference between the FUNWAVE and NHWAVE modeling results. Thus, for each landslide, we determine the maximum potential extent of flooding by generating a composite set of results from all models.

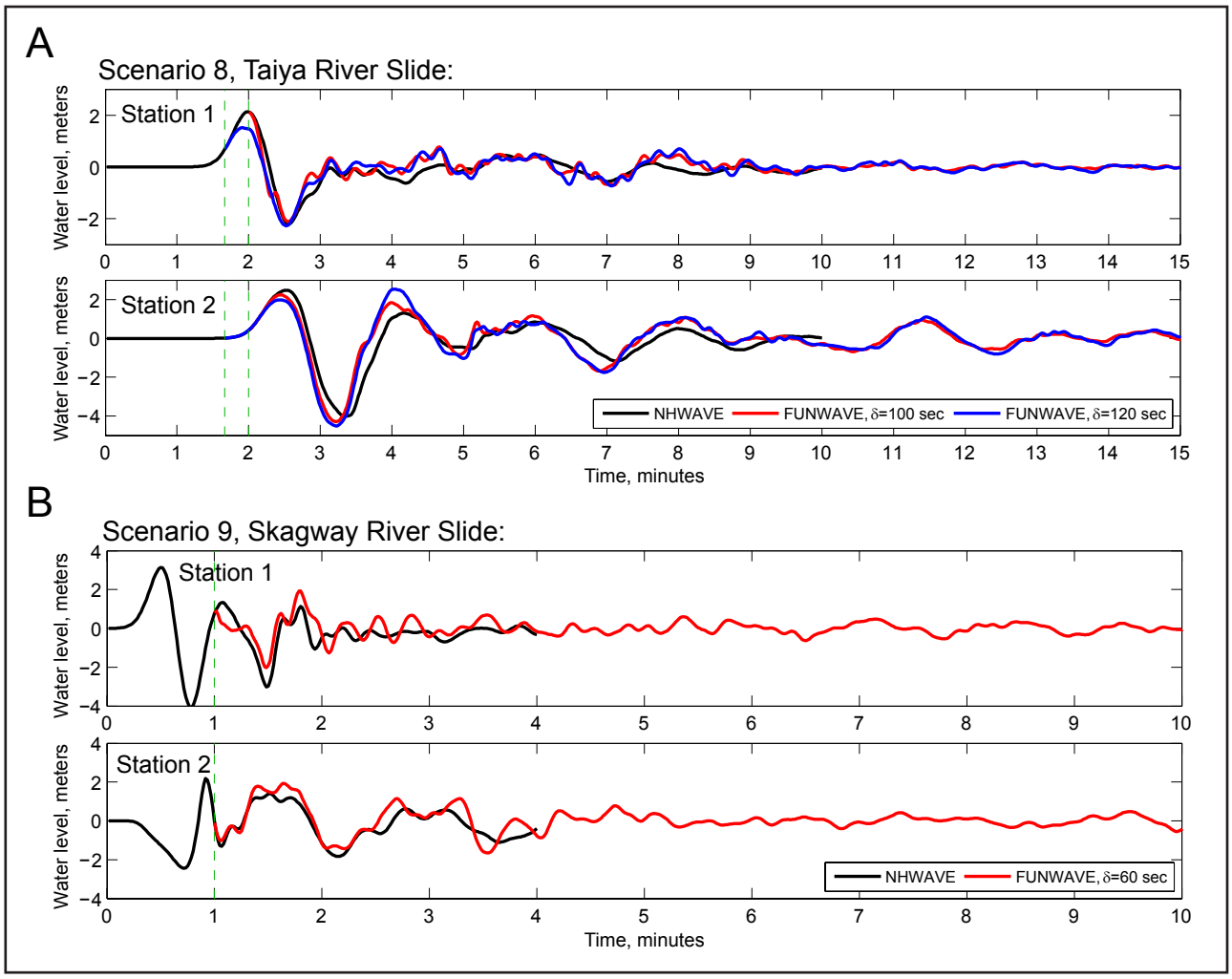

Figure 14. Comparison of scenarios 8-9 NHWAVE- and FUNWAVE-computed water-level dynamics at two stations near Skagway, shown by green stars in figure 4a.

Modeled hypothetical inundation for Skagway

Numerical simulations of landslide-generated tsunamis indicate that the first wave can reach Skagway in less than a minute (scenario 9, the Skagway River slide, fig. 4A). Figure 14 shows plots of water-level dynamics for the two slide scenarios in Skagway (see fig. 4A for station locations in Taiya Inlet and Skagway Harbor). While the waves that reach the city harbor are rather small (i.e., only about 2 m [6 ft] high) they nevertheless breach the shoreline and flood low-lying areas. Because the city is located on flat, low-lying ground, waves travel far inland and flood an extensive area beyond the harbor (fig. 16). The composite flow depth for these two landslide scenarios is shown in figure 17. It is important to note that while most of the flooding beyond the shoreline areas is less than 0.6 m (2 ft), tsunami currents can be strong (and may carry debris) and could easily overwhelm pedestrians.

Finally, the hypothetical inundation according to our models is much more extensive than the inundation caused by the 1994 dock failure and underwater slide. The 1994 slide occurred at an extreme low tide of -1.3 m (4 ft) relative to the MLLW datum and did not flood beyond the shoreline. Our hypothetical tsunamis are modeled above the MHHW datum and the vertical difference between MLLW and MHHW is about 5.1 m (17 ft).

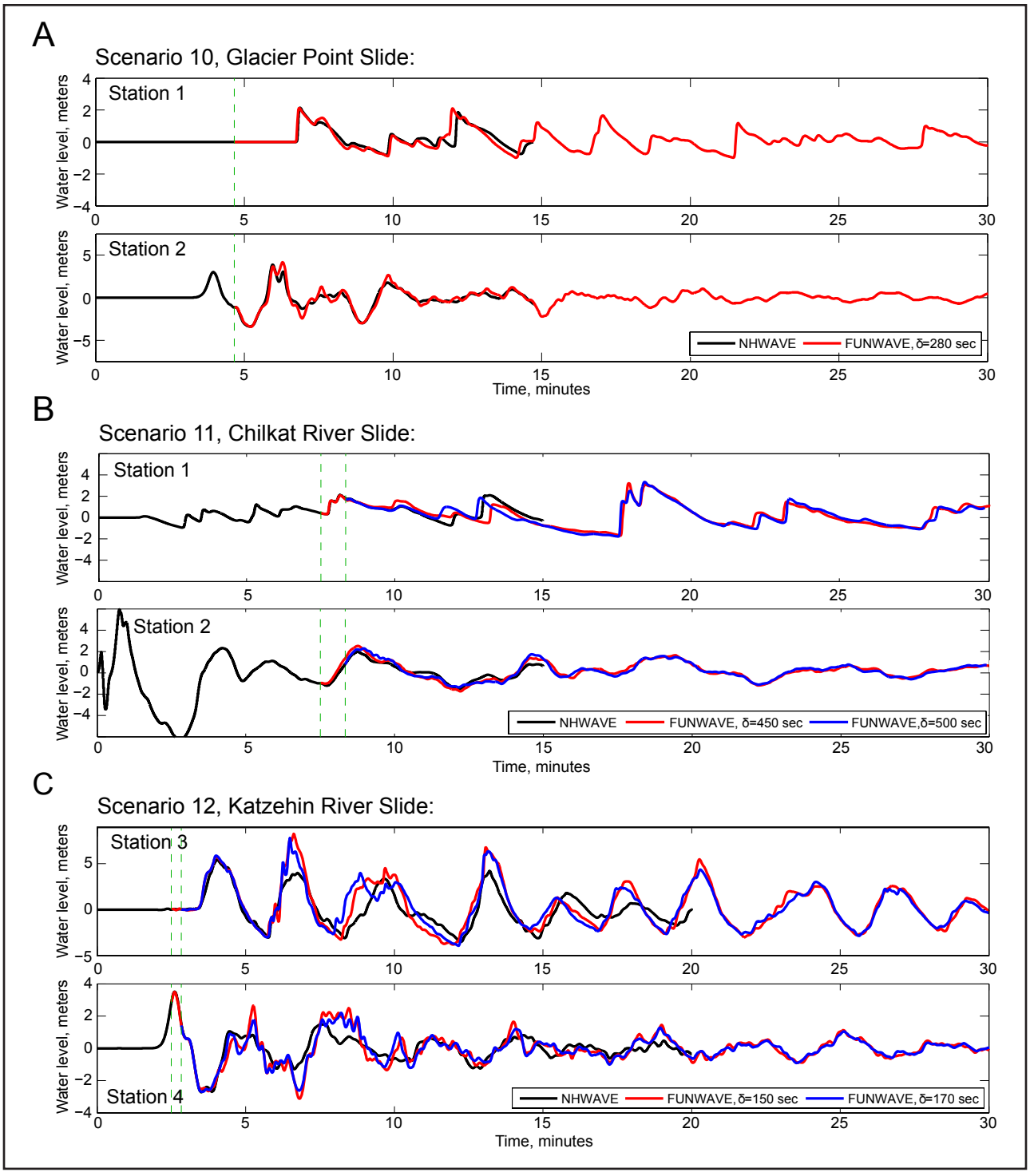

Figure 15. Comparison of scenarios 10-13 NHWAVE- and FUNWAVE-computed water-level dynamics at four stations near Haines, shown by green stars in figure 4b.

Modeled hypothetical inundation for Haines

The maximum flow depth over dry land (above the Mean Sea Level [MSL] datum) in Chilkat Inlet for the GP slide (scenario 10) is shown in figure 18A and the maximum flow depth for the CR slide (scenario 11) is shown in figure 18B. Numerical experiments indicate that the first waves ar-

rive at the Haines airport in about 25–30 minutes after the initial underwater failure.

Waves generated by the KR slide (scenario 12) can reach the city harbor in only 3–4 minutes after the initial slope failure; figure 19 shows a time-series of modeled water heights near Haines city harbor. The landslide-generated wave (fig. 19A) first produces a local runup at Nukdik Point (fig. 19B) and 30 seconds later the wave reaches the city harbor area (fig. 19C). Seconds later, waves converging from the north and south meet near Mission Street and produce an amplified local runup there (fig. 19D). The resulting inundation near the city harbor for scenario 12 is shown in figure 20. It is important to note that there are many unknowns regarding how the converging waves will interfere with one other. The local runup along Mission Street could be smaller than the model shows. However, it could potentially be worse than what our model shows. The local topographic high along Mission Street is shown in figure 20. If the wave propagates beyond this local high, then water can flow all the way to Chilkat Inlet. We emphasize that the numerical grids used to calculate local runup are based on a bare-earth DEM. Even though the resolution of the Haines grid is high enough to describe major relief features, some small topographic features, buildings, and other facilities cannot be resolved accurately by the existing model. Therefore, there is an uncertainty in local runup along the Mission Street related to the bare-earth DEM.

Finally, we discuss the potential tsunami generated by scenario 13—a hypothetical Taiyasanka Harbor Moraine slide (fig. 21). According to the numerical experiment, the first wave, about 2–3 m (6.6–9.8 ft) high, can reach the Haines (fuel terminal) 60 seconds after the initial slope failure. There the wave splits and propagates west to the ferry dock and south to the city harbor. According to the numerical experiment, the waves can reach 2 m (6.6 ft) in the city harbor and produce local runup to 3–4 m (9.8–13 ft). Numerical experiments also indicate a maximum local runup south of the Haines fuel terminal may reach 10 m (33 ft) above sea level. However, the modeled inundation has large uncertainties and is only to be used as a guideline—the accuracy of the DEM near the ferry dock is not as good as near the city harbor.

Composite inundation

We use the predicted maximum flow depths from both hypothetical landslide-generated and tectonic tsunamis to develop the composite flow depth maps for Skagway and Haines, as strong ground motions from large earthquakes can potentially trigger landslides. In particular, we superpose the maximum-credible tectonic tsunami (scenario 4M, with the modified slip of scenario 4 as part of the numerical modeling technique) with inundation from landslide-generated tsunamis (scenarios 8–13) by selecting the maximum computed flow depth values at each grid point. Map sheet 1 shows the maximum composite calculated extent of inundation and the maximum composite flow depths over dry land in Skagway, respectively. Map Sheets 2 and 3 illustrate the same results for Haines.

We note that while scenario 4 is the maximum credible event considered in our study, the available geologic evidence suggests that repeated 1964-type events (scenario 1) might occur more frequently over the course of multiple seismic cycles (several thousands of years) and therefore we present results from this type of earthquake as well. Thus, on map sheets 1, 2, and 3, we also plot the potential inundation areas according to tectonic scenarios 1M and 4. Recall that scenario 1M, similar to scenario 4M, accounts for the underestimation of the modeling results due to tsunami-tide interactions. The wave heights according to scenario 1M correlate well with the observations of the 1964 tsunami in the city, and thus scenario 1M also provides a plausible estimate of future tsunami inundation for a repeat of the 1964 event.

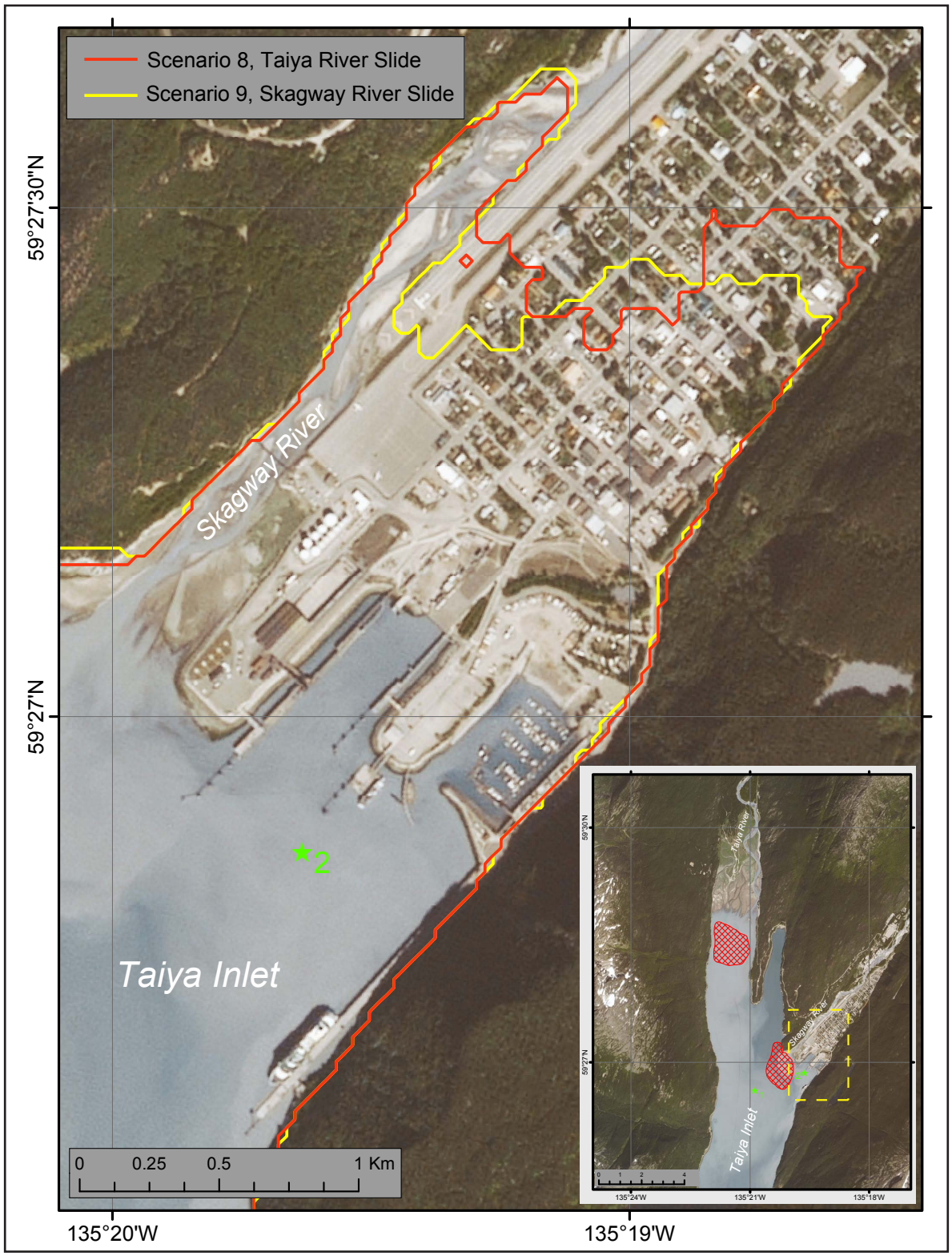

Figure 16. Modeled extents of inundation for submarine landslide scenarios 8 and 9 at Skagway. Point 2, marked by a green star, is a location for which time series of water level are shown in figure 14.

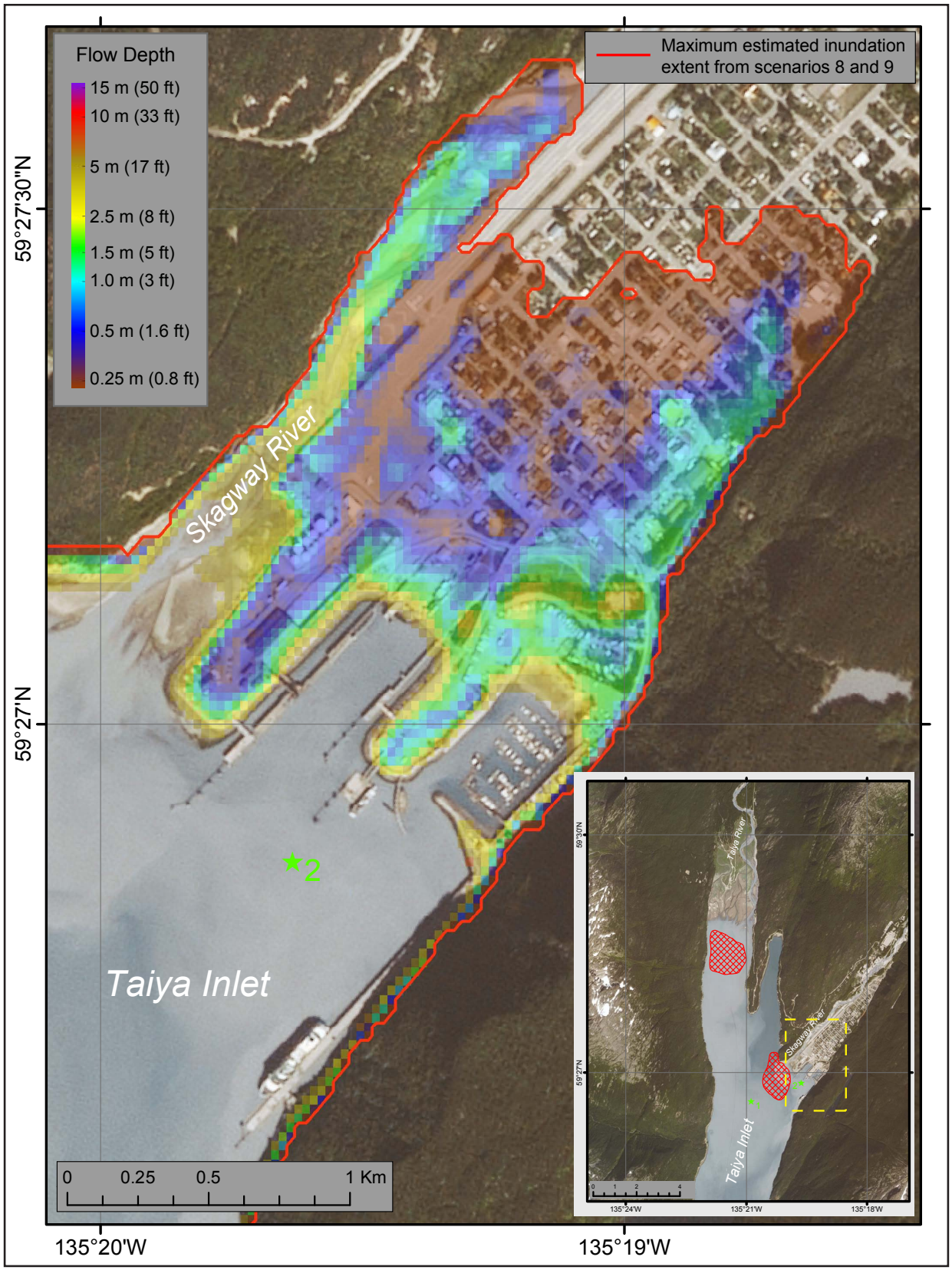

Figure 17. Maximum water flow depth from all hypothetical landslide scenarios at Skagway. Flow depth is computed as maximum composite of NHWAVE and FUNWAVE flow depths. Point 2, marked by a green star, is a location for which time series of water level are shown in figure 14.

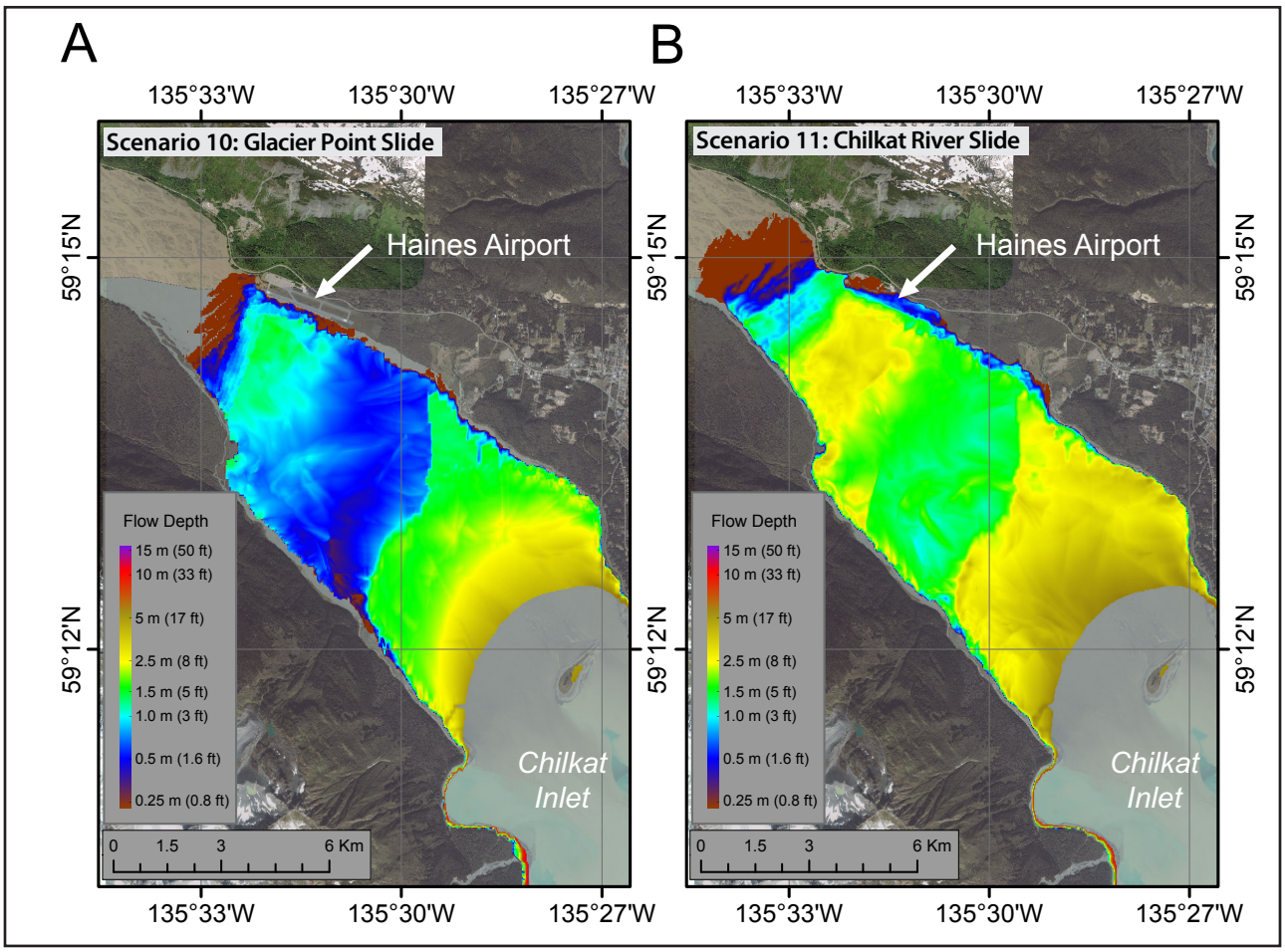

Figure 18. Maximum water flow depth from two hypothetical landslide-generated tsunamis at Haines. Flow depth is computed as maximum composite of NHWAVE and FUNWAVE flow depths. (**A**) Scenario 10–Glacier Point slide; (**B**) Scenario 11–Chilkat River slide. Slide thicknesses for each scenario are shown in figure 9.

Time series and other numerical results

We supplement inundation maps with the time series of modeled water levels and velocity dynamics at certain locations around the town to provide emergency managers with the tools necessary to completely assess the tsunami hazard in Skagway and Haines. Emergency managers should consider the arrival time of the first wave, the maximum wave amplitude, and the duration of wave action during their evacuation planning. Appendices A and B contain time series plots of sea level and velocity at critical locations for scenarios 1M and 4M for Skagway and Haines, respectively. Both scenarios were simulated with the modified coseismic slip values as a part of the numerical modeling technique. As described previously, this technique produces a close match to the observed wave height that occurred in 1964, validating this approach. Although scenario 4M is thought to be the worst-case tectonic tsunami, scenario 1M is a good representation of what a repeat of the 1964 event might look like. Because there are four models of repeat 1964 events and because the Johnson and others (1996) model produces the highest waves, we use the Johnson and others (1996) model to represent a repeat of the 1964 event.

For each location shown by a number in figures A-1 and B-1, we plot the sea level and water velocity according to both scenarios in figures A-2 and B-2. Zero time corresponds to the earthquake origin time. Elevations of onshore locations and

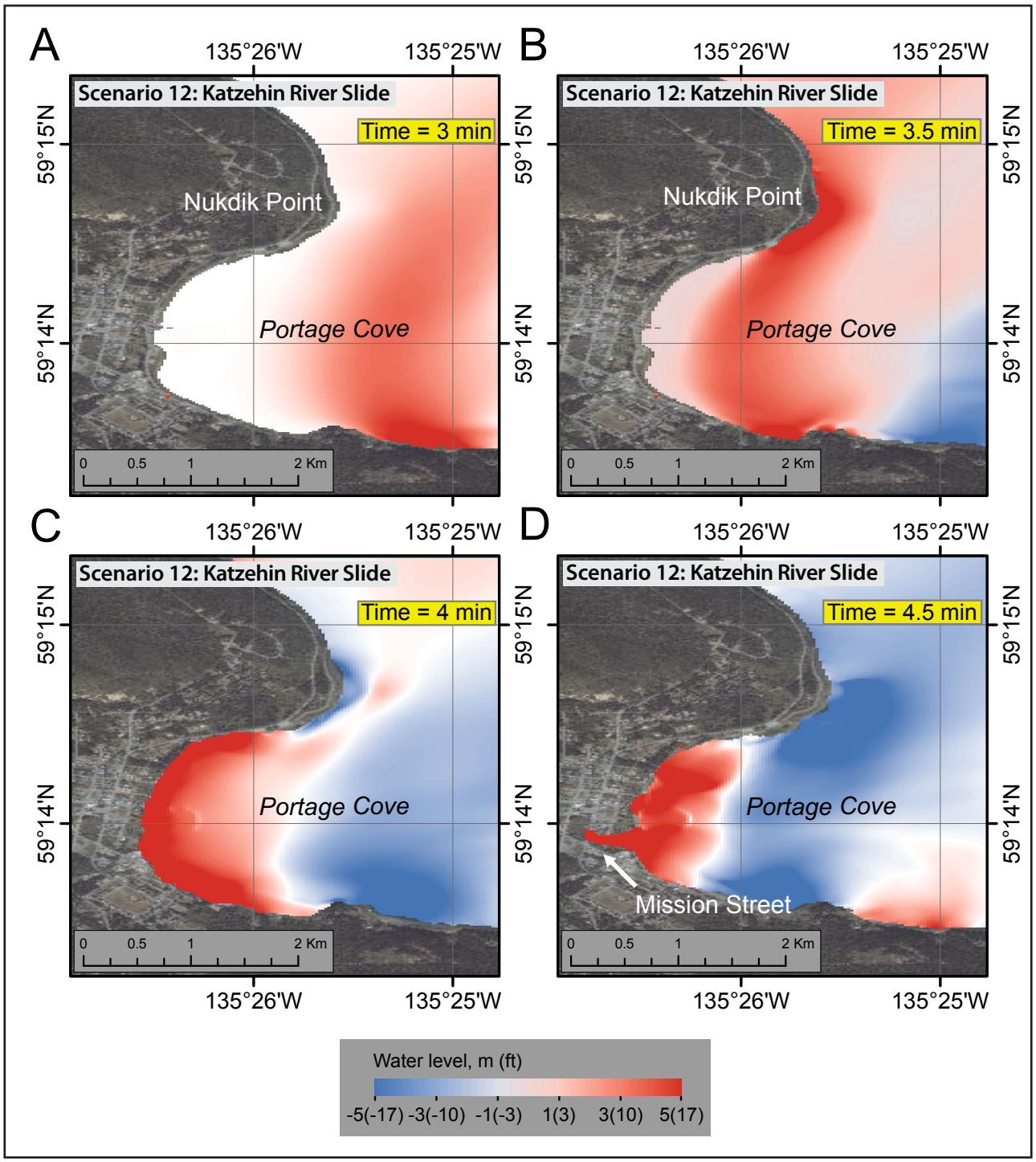

Figure 19. A series of snapshots for the modeled water height due to the hypothetical Katzehin River slide (scenario 12) near the Haines city harbor.

values of ocean depth at offshore locations are based on the MHHW datum. Because velocity magnitude is calculated as water flux divided by water depth, the velocity value has large uncertainties in shallow water. In these plots, velocity is computed only where water depth is greater than 0.3 m (1 ft).

For scenario 1M, the maximum water level is about 1.8 m (5.9 ft) and it occurs at the Skagway tide

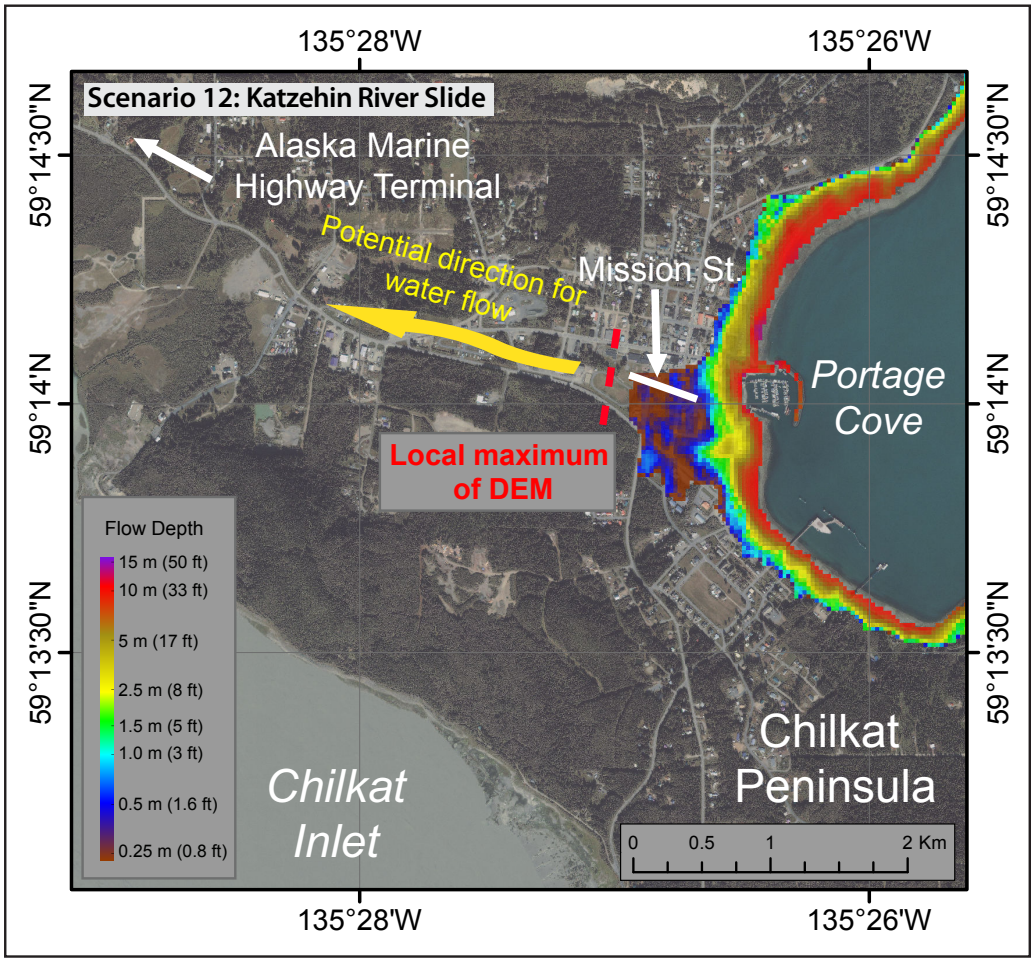

Figure 20. Inundation and flow depths near the Haines city harbor for scenario 12. The local topographic maximum along the Mission Street is shown by the dashed red line.

gauge (point 1; fig. A-1) about 5 hours 10 minutes after the earthquake (point 1; fig. A-2). The same scenario results in the maximum water level of about 1.4 m (4.6 ft) at the Haines small boat harbor (point 2; fig. B-1) about 6 hours 40 minutes after the earthquake (point 2; fig. B-2). For scenario 4M, the maximum water level is about 2.5 m (8.2 ft) and it occurs at the Skagway tide gauge (point 1; fig. A-1) about 4 hours 50 minutes after the earthquake (point 1; fig. A-2). The same scenario results in the maximum water level of about 1.7 m (5.6 ft) at the Haines small boat harbor (point 2; fig. B-1) about 4 hours 50 minutes after the earthquake (point 2; fig. B-2).

The strongest tsunami currents of 1.4 m/s (4.6 ft/s; 2.7 knots) occur at the Skagway Broadway dock (point 3, fig. A-1) about 4 hours after the earthquake, and the maximum tsunami currents of 2.7 m/s (8.9 ft/s; 5.3 knots) occur in Chilkat Inlet (point 7, fig. B-1) about 7.5 hours after the earthquake. The tsunami activity continues for at least 24 hours, with a 1 m (3.3 ft) wave arriving in Skagway and Haines as late as 19 hours after the earthquake, (figs. A-2 and B-2). Maximum wave heights at the selected locations are listed in tables A-1 and B-1 for Skagway and Haines, respectively.

Because water level oscillations can continue for more than a full day, even if the earthquake occurs during a low tide, these oscillations will be affected by the subsequent rising tide. Low-lying areas that were not initially flooded may become inundated 24–48 hours after the earthquake. Another important factor in the tsunami hazard assessment for any coastal community is the arrival time of the first wave. The time series plots demonstrate that the first wave arrives at both Skagway and Haines about 3 hours after the earthquake. This means that people in the communities would have up to 3 hours for evacuation if the tsunami

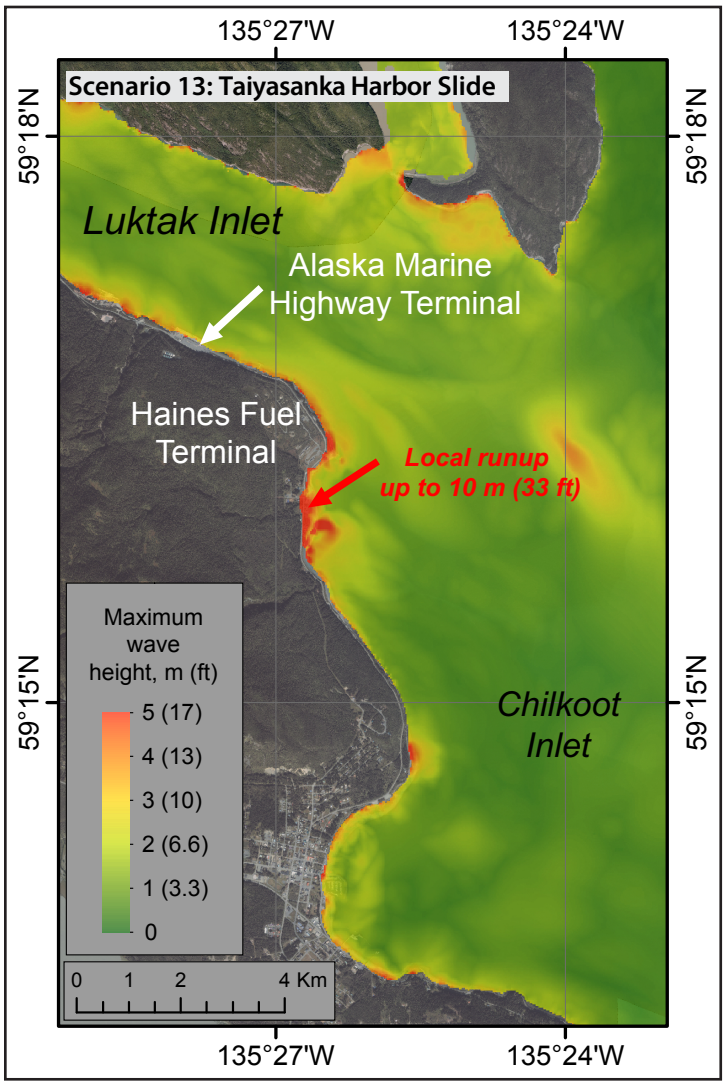

Figure 21. Hypothetical inundation at the Haines ferry terminal due to Taiyasanka Harbor Moraine slide (scenario 13). The area of the local maximum runup south of the Haines fuel terminal is shown by the red arrow.

is generated by a megathrust earthquake in the Gulf of Alaska. However, underwater landslides in the vicinity of Skagway and Haines are capable of producing waves that could reach onshore locations within minutes after the slope failure. Plots of the modeled water level and velocity for local landslide-generated tsunamis are shown in figures A-3 and B-3 for Skagway and Haines, respectively. These figures demonstrate the very large flow velocities compared to the results of the modeling for seismic sources, indicating that a near-field landslide tsunami can produce very large flow velocities that result in large impulse forces on buildings, causing much greater damage than just the static flow depth. Because the landslide-generated tsunamis are simulated both with the NHWAVE and FUNWAVE models using the two-stage approach, we provide the time series for both models. Because FUNWAVE was initialized at time d after the slide collapse, the FUNWAVE results are not available at the beginning of each scenario. Providing all modeling results permits an estimate of the uncertainty in wave heights. Recognizing that arrival time affects the vulnerability of a community to tsunami hazard has special significance for local emergency officials in evacuation planning.

Sources of errors and uncertainties

The hydrodynamic model used to calculate propagation and run-up of tectonic tsunamis is a nonlinear, flux-formulated, shallow-water model (Nicolsky and others, 2011b; Nicolsky, 2012)

that passed the verification and validation tests required for numerical codes used to produce tsunami inundation maps (Synolakis and others, 2007; National Tsunami Hazard Mitigation Program [NTHMP], 2012). The NHWAVE and FUNWAVE models used to simulate inundation from landslide-generated tsunamis have also passed the same NHTMP verification and validation tests (Tehranirad and others, 2012). Most of the errors/uncertainties in the numerical predictions originate from the tsunami sources used in the numerical models. Due to insufficient data on locations and volumes of hypothetical subaerial landslides, we do not model tsunamis generated by this type of landslide even though they present a significant potential hazard to Alaskan coastal communities.

Uncertainties in landslide tsunami sources remain high, and future tsunami hazard assessment studies would benefit greatly from the collection of additional onshore and offshore data. Geologic-hazards fieldwork on mountain slopes surrounding Lutak and Taiya inlets could help identify potential mass movement features and rockfalls (e.g., see figure 4C). For example, on September 5, 2017, a rockslide occurred at the north end of the railroad dock in Skagway (http://skagwaynews.com/2017/09/05/early-morning-rockfall-damages-railroad-dock/); on-the-ground mapping could assess the potential for a larger subaerial rockfall that might enter the ocean and generate a local tsunami with significant impact on the community and damage to critical infrastructure. Multibeam echo sounding and shallow seismic profiling of the ocean bottom could delineate extents and volumes of previous submarine landslides in the northern Chilkoot Inlet and Taiya Inlet, as has been previously accomplished in Seward and Valdez (Lee and others, 2006). Finally, we note that uncertainties in the inundation modeling of the Haines airport area could be significantly reduced by conducting a high-resolution lidar survey of the head of Chilkat Inlet.

The spatial resolution of the grid used to calculate tsunami inundation at Skagway and Haines is about 16 m (52.5 ft) and satisfies NOAA minimum recommended requirements for computation of tsunami inundation (National Tsunami Hazard Mitigation Program [NTHMP], 2010). We stress that this resolution is high enough to describe major relief features; however, small topographic features, buildings, and other facilities cannot be resolved accurately by the existing model. We also note that uncertainty in grid cell elevation/depth propagates into the modeling results and eventually contributes to the horizontal uncertainty in a location of the inundation line. However, no established practices exist to directly propagate the DEM uncertainty into the uncertainty of the inundation line (Hare and others, 2011). In addition to the uncertainty related to the grid cell elevation/depth, uncertainties in the tsunami source (earthquake and landslide geometry) are the largest sources of error in tsunami modeling efforts. The direction of the incoming waves, their amplitudes, and times of arrival are primarily determined by displacements of the ocean surface in the source area. Therefore, the inundation modeling results for local sources are especially sensitive to the fine structure of the tsunami source. The modeling process is highly sensitive to errors when the complexity of the source function is combined with its proximity to the coastal zone. The current practice is to create some additional buffer area around the inundation line to use for hazard mitigation and decisions related to tsunami evacuation.

SUMMARY

We present the results of numerical modeling of tectonic and submarine landslide-generated tsunami waves for the town of Haines and Skagway in southeastern Alaska. Each of our scenarios is geologically reasonable and presents potential hazards to the community. Scenario 4, based on a Tohoku-type source mechanism, is considered the worst-case tectonic tsunami scenario. How-

ever, the available geologic and paleoseismic evidence indicates that repeated 1964-type events may occur more frequently over the course of multiple seismic cycles (several thousands of years) and therefore we present results from this type of earthquake as well (scenario 1). Because our models slightly underestimate tsunami wave heights (due to tsunami-tide interactions that are not well understood), we create modified scenarios 4M and 1M to account for these shortcomings. We also explore several landslide-generated tsunamis that could result in short arrival times and high wave amplitudes. In Skagway, the Taiya River slide results in the most significant inundation. A local underwater slide at Katzehin River delta presents a tsunami hazard for Haines, while an underwater slide in Taiyasanka Harbor can create damaging waves at the Haines fuel terminal.

The maps that are part of this report have been completed using the best information available and are believed to be accurate; however, their preparation required many assumptions. We have considered several tsunami scenarios and have provided an estimate of maximum credible tsunami inundation. Actual conditions during a tsunami event may vary from those considered, so the report's accuracy cannot be guaranteed. The limits of inundation shown should only be used as a guideline for emergency planning and response action. Actual areas inundated will depend on specifics of earth deformations, on-land construction, and tide level and may differ from areas shown on the map. The information on this map is intended to assist state and local agencies in planning for emergency evacuation and tsunami response actions in the event of a major tsunamigenic earthquake. These results are not intended for land-use regulation or building-code development.

ACKNOWLEDGMENTS

This report was funded by Award NA16NWS4670030 by a National Tsunami Hazard Mitigation Program grant to Alaska Division of Homeland Security and Emergency Management and University of Alaska Fairbanks from the Department of Commerce/National Oceanic and Atmospheric Administration. This does not constitute an endorsement by NOAA. Numerical calculations for this work were supported by High Performance Computing (HPC) resources at the Research Computing Systems unit at the Geophysical Institute, University of Alaska Fairbanks. Thoughtful reviews by Stephan Grilli (University of Rhode Island) and Richard Koehler (University of Nevada) improved the report.

REFERENCES

Alaska Department of Labor and Workforce Development, 2016. http://labor.alaska.gov

Balay, S., Brown, J., Buschelman, K., Eijkhout, V., Gropp, W., Kaushik, D., Knepley, M., Curfman McInnes, L., Smith, B., and Zhang, H., 2012, PETSc Users Manual ANL_95/11, Revision 3.3: Argonne National Laboratory, Mathematics and Computer Science Division, 211 p. www.mcs.anl.gov/petsc/petsc-3.3/docs/manual.pdf

Caldwell, R.J., Taylor, L.A., Eakins, B.W., Carignan, K.S., and Collins, S. V., 2012, Digital elevation models of Juneau and Southeast Alaska—Procedures, data sources and analysis: National Geophysical Data Center, NOAA Technical Memorandum NESDIS NGDC, p. 53, 66.

Campbell, B.A., 1997, Analysis of the November 3, 1994 Skagway seafloor instability: *Unpublished Report*, Campbell and Associates, Anchorage, Alaska.

Campbell, B.A., and Nottingham, D.P.E., 1999, Anatomy of a landslide-created tsunami at Skagway, Alaska, November 3, 1994: Science of Tsunami Hazards, v. 17, no. 1, p. 19–42.

Cornforth, D.H., and Lowell, J.A., 1996, The 1994 submarine slope failure at Skagway, Alaska, *in* Senneset, K., ed., Proceedings of the 7th International Symposium on Landslides: A. A. Balkema, Rotterdam, p. 527–532.

Cossart, E., Braucher, R., Fort, M., Bourlès, D.L., and Carcaillet, J., 2008, Slope instability in relation to glacial debuttressing in alpine areas (Upper Durance catchment, southeastern France): Evidence from field data and 10Be cosmic ray exposure ages: Geomorphology, v. 95, no. 1–2, p. 3–26. https://doi.org/10.1016/j.geomorph.2006.12.022

Coulter, H.W., and Migliaccio, R.R., 1966, Effects of the earthquake of March 27, 1964 at Valdez, Alaska: U.S. Geological Survey Professional Paper, 542-C, 36 p. https://pubs.usgs.gov/pp/0542c

Doser, D.I., and Lomas, R., 2000, The transition from strikeslip to oblique subduction in southeastern Alaska from seismological studies: Tectonophysics, v. 316, p. 45–65.

Dunbar, P.K., and Weaver, C.S., 2008, U.S. states and territories national tsunami hazard assessment— Historical record and sources for waves: National Oceanic and Atmospheric Administration and U.S. Geological Survey, Technical Report, 59 p. http://nthmp.tsunami.gov/documents/Tsunami_Assess

Evans, S.G., and Clague, J.J., 1994, Recent Climatic change and catastrophic geomorphic processes in mountain environments: Geomorphology, v. 100, p. 107–128.

Fine, I. V., Rabinovich, A.B., Kulikov, E.A., Thomson, R.E., and Bornhold, B.D., 1998, Numerical modeling of landslide-generated tsunamis with application to the Skagway Harbor tsunami of November 3, 1994, *in* Proceedings of the International Conference on Tsunamis: Paris, p. 211–223.

Geist, B.E.L., Jakob, M., Wieczorek, G.F., and Dartnell, P., 2003, Preliminary Hydrodynamic Analysis of Landslide-Generated Waves in Tidal Inlet, Glacier Bay National Park, Alaska p. 2–20.

Geist, E.L., and Lynett, P., 2014, Source processes for the probabilistic assessment of tsunami hazards: Oceanography, v. 27, no. 2, p. 86–93. http://doi.org/10.5670/oceanog.2014.43

Geist, E.L., and Parsons, T., 2006, Probabilistic analysis of tsunami hazards: Natural Hazards. v. 37, no. 3, p. 277–314. http://dx.doi.org/10.1007/s11069-005-4646-z

Goto, C., Ogawa, Y., Shuto, N., and Imamura, F., 1997, IUGG/IOC time project: numerical method of tsunami simulation with the leap-frog scheme: Manuals and Guides, no. 35, Intergovernmenetal Oceanographic Commission of UNESCO, Paris.

Grilli, S.T., O'Reilly, C., and Tajalli Bakhsh, T., 2013, Modeling of SMF tsunami generation and regional impact along the upper U.S. East Coast: Center for Applied Coastal Research, University of Delaware, Research Report No. CACR-13-05. http://www1.udel.edu/kirby/nthmp/reports/grilli-etal-cacr-13-05.pdf

Haeussler, P.J., Lee, H.J., Ryan, H.F., Labay, K.A., Kayen, R.E., Hampton, M.A., and Suleimani, E.N., 2007, Submarine slope failures near Seward, Alaska, during the M9.2 1964 earthquake, *in* Lykousis, V., Sakellariou, D., and Locat, J., eds., Submarine mass movements and their consequences: Springer, p. 269–278.

Hamilton, S., and Shennan, I., 2005, Late Holocene great earthquakes and relative sea-level change at Kenai, southern Alaska: Journal of Quaternary Science, v. 20, no. 2, p. 95–111.

Hampton, M.A., Lemke, R.W., and Coulter, H.W., 2002, Submarine landslides that had a significant impact on man and his activities, Seward and Valdez, Alaska, *in* Schwab, W.C., Lee, H.J., and Twichell, D.C., eds., Submarine Landslides—Selected Studies in the U.S. Exclusive Economic Zone: U.S.G.S. Bulletin 2002, p. 123–134. https://pubs.er.usgs.gov/publication/b2002

Hare, Rob, Eakins, Barry, Amante, Chris, and Taylor, L.A., 2011, Modeling bathymetric uncertainty: US HYDRO 2011 conference, Tampa, FL, April 25–28, 2011, Proceedings. http://ushydro.thsoa.org/us11papers.htm

Hayes, G.P., Wald, D.J., and Johnson, R.L., 2012, Slab1.0: A three-dimensional model of global subduction zone geometries: Journal of Geophysical Research, v. 117, no. B01, p. 302. http://doi.org/10.1029/2011JB008524

Heezen, B.C., and Johnson, G.L., 1969, Alaskan submarine cables: a struggle with a harsh environment: ARCTIC, v. 22, no. 4. https://doi.org/10.14430/arctic3232

Holtkamp, Stephen, and Ruppert, Natalia, 2015, A high resolution aftershock catalog of the magnitude 7.5 Craig, Alaska, earthquake on 5 January 2013: Bulletin of the Seismological Society of America, v. 105, no. 2, p. 1,143–1,152. http://doi.org/10.1785/0120140179

Ichinose, G., Somerville, P., Thio, H.K., Graves, R., and O'Connell, D., 2007, Rupture process of the 1964 Prince William Sound, Alaska, earthquake from the combined inversion of seismic, tsunami, and geodetic data: Journal of Geophysical Research, v. 112, no. B07, p. 2,156–2,202. http://doi.org/10.1029/2006JB004728

Ito, Y., Tsuji, T., Osada, Y., Kido, M., Inazu, D., Hayashi, Y., Tsushima, H., Hino, R., and Fujimoto, H., 2011, Frontal wedge deformation near the source region of the 2011 Tohoku-Oki earthquake: Geophysical Research Letters, v. 38, no. 7. http://doi.org/10.1029/2011GL048355

Jiang, L., and LeBlond, P.H., 1992, The coupling of a submarine slide and the surface waves which it generates: Journal of Geophysical Research, v. 97, no. C8, p. 12,731–12,744. http://doi.org/10.1029/92JC00912

Johnson, J.M., Satake, K., Holdahl, S.R., and Sauber, J., 1996, The 1964 Prince William Sound earthquake—Joint inversion of tsunami waveforms and geodetic data: Journal of Geophysical Research, v. 101, no. B1, p. 523–532. http://doi.org/10.1029/95JB02806

Kachadoorian, R., 1965, Effects of the earthquake of March 27, 1964, at Whittier, Alaska: U.S. Geological Survey Professional Paper 542-B, p. B1–B21, 3 sheets, scale 1:4,800.

Kanamori, H., 1970, The Alaska earthquake of 1964—Radiation of long-period surface waves and source mechanism: Journal of Geophysical Research, v. 75, no. 26, p. 5,029–5,040. http://doi.org/10.1029/JB075i026p05029

Kirby, S., Scholl, D., von Huene, R., and Wells, R., 2013, Alaska earthquake source for the SAFRR tsunami scenario, Chapter B, *in* Ross, S.L., and Jones, L.M., eds., The SAFRR (Science Application for Risk Reduction) Tsunami Scenario: U.S.G.S. Open-File Report 2013–1170, 40 p. http://pubs.usgs.gov/of/2013/1170/b/

Kirby, J.T., Shi, F., Nicolsky, D.J., and Misra, S., 2016, The 27 April 1975 Kitimat, British Columbia submarine landslide tsunami—A comparison of modeling approaches: Landslides, v. 13, no. 6, p. 1,421–1,434. http:// doi.org/10.1007/s10346-016-0682-x

Kowalik, Z., 1997, Landslide-generated tsunami in Skagway, Alaska: Science of Tsunami Hazards, v. 15, no. 2, p. 89–106.

Kowalik, Z., and Proshutinsky, A., 2010, Tsunami–tide interactions—A Cook Inlet case study: Continental Shelf Research, v. 30, no. 6, p. 633–642.

Kowalik, Z., Proshutinsky, T., and Proshutinsky, A., 2006, Tide–Tsunami Interactions: Science of Tsunami Hazards, v. 24, no. 4, p. 242–256.

Kulikov, E.A., Rabinovich, A.B., Fine, I. V., Bornhold, B.D., and Thomson, R.E., 1998, Tsunami generation by landslides at the Pacific coast of North America and the role of tides: Oceanology, v. 38, no. 3, p. 323–328.

Kulikov, E.A., Rabinovich, A.B., Thomson, R.E., and Bornhold, B.D., 1996, The landslide tsunami of November 3, 1994, Skagway Harbor, Alaska: Journal of Geophysical Research, v. 101, no. C3, p. 6609–6615. https://doi.org/10.1029/95JC03562

Lander, J.F., 1996, Tsunamis affecting Alaska, 1737–1996: Boulder, CO, NOAA National Geophysical Data Center (NGDC), Key to Geophysical Research Documentation, v. 31, 195 p.

Lee, H.J., Ryan, H., Kayen, R.E., Haeussler, P.J., Dartnell, P., and Hampton, M.A., 2006, Varieties of submarine failure morphologies of seismically-induced landslides in Alaskan fjords: Norwegian Journal of Geology (Norsk Geologisk Tidsskrift), v. 86, no. 3, p. 221–230.

Leonard, L.J., and Bednarski, J.M., 2015, The preservation potential of coastal coseismic and tsunami evidence observed following the 2012 M_W 7.8 Haida Gwaii thrust earthquake, in 2012 Haida Gwaii and 2013 Craig earthquakes at the Pacific North America plate boundary (British Columbia and Alaska), Bulletin of the Seismological Society of America, v. 105, no. 2B, p. 1,280–1,289. http://doi.org/10.1785/0120140193

Lemke, R.W., 1967, Effects of the earthquake of March 27, 1964, at Seward, Alaska: U.S. Geological Survey Professional Paper 542-E, 43 p., 2 sheets, scale 1:63,360.

Lemke, R.W., and Yehle, L.A., 1972, Reconnaissance engineering geology of the Haines area, Alaska, with emphasis on evaluation of earthquake and other geologic hazards: U.S. Geological Survey Open-File Report 72-229, 109 p., 2 sheets, scale 1:24,000. http://pubs.er.usgs.gov/publication/ofr72229

Lopez-Venegas, A.M., Horrillo, J., Pampell-Manis, A., Huerfano, V., and Mercado, A., 2014, Advanced tsunami numerical simulations of the Puerto Rico October 11, 1918, Mona Passage tsunami: Pure and Applied Geophysics, v. 172, no. 6, p. 1,679–1,698. http://doi.org/10.1007/s00024-014-0988-3

Love, M.R., Eakins, B.W., Taylor, L.A., Carignan, K.S., Friday, D., and Grothe, P.R., 2012, Digital Elevation Model of Port Alexander, Alaska: Procedures, Data Sources and Analysis, NOAA Technical Memorandum NESDIS NGDC-63, U.S. Dept. of Commerce, Boulder, CO, 35 p.

Løvholt, F., Pedersen, G., Harbitz, C.B., Glimsdal, S., and Kim, J., 2015, On the characteristics of landslide tsunamis: Philosophical Transactions of the Royal Society A, v. 373, no. 2053. http://doi.org/10.1098/rsta.2014.0376

Ma, G., Shi, F., and Kirby, J.T., 2012, Shock-capturing non-hydrostatic model for fully dispersive surface wave processes: Ocean Modelling, v. 43–44, p. 22–35. http://doi.org/10.1016/j.ocemod.2011.12.002

Macpherson, A.E., Nicolsky, D.J., and Suleimani, E.N., 2014, Digital elevation models of Skagway and Haines, Alaska: Procedures, data sources, and quality assessment: Alaska Division of Geological & Geophysical Surveys Miscellaneous Publication 155, 15 p. http://doi.org/10.14509/29143

Mader, C.L., 1997, Modeling the 1994 Skagway tsunami: Science of Tsunami Hazards, v. 15, no 1, p. 41–48.

Miller, D.J., 1960, The Alaska earthquake of July 10, 1958: Giant wave in Lituya Bay: Bulletin of the Seismological Society of America, v. 50, no. 2, p. 253–266.

NCEI/WDS Global historical tsunami database at NCEI, 2100 BC to present (interactive map): National Centers for Environmental Information, NOAA. http://doi.org/10.7289/V5PN93H7

Nicolsky, D.J., 2012, Alaska tsunami model, *in* Proceedings and Results of the 2011 NTHMP Model Benchmarking Workshop: Boulder, CO, U. S. Department of Commerce/NOAA/NTHMP, NOAA Special Report, p. 55-87. http://nthmp.tsunami.gov

Nicolsky, D.J., Suleimani, E.N., Combellick, R.A., and Hansen, R.A., 2011a, Tsunami inundation maps of Whittier and western Passage Canal, Alaska: Alaska Division of Geological & Geophysical Surveys Report of Investigation 2011-7, 65 p., 4 sheets. http://doi.org/10.14509/23244

Nicolsky, D.J., Suleimani, E.N., Freymueller, J.T., and Koehler, R.D., 2015, Tsunami inundation maps of Fox Islands communities, including Dutch Harbor and Akutan, Alaska: Alaska Division of Geological & Geophysical Surveys Report of Investigation 2015-5, 67 p., 2 sheets, scale 1:12,500. http://doi.org/10.14509/29414

Nicolsky, D.J., Suleimani, E.N., Haeussler, P.J., Ryan, H.F., Koehler, R.D., Combellick, R.A., and Hansen, R.A., 2013, Tsunami inundation maps of Port Valdez, Alaska: Alaska Division of Geological & Geophysical Surveys Report of Investigation 2013-1, 77 p., 1 sheet, scale 1:12,500. http://doi.org/10.14509/25055

Nicolsky, D.J., Suleimani, E.N., and Hansen, R.A., 2011b, Validation and verification of a numerical model for tsunami propagation and runup: Pure and Applied Geophysics, v. 168, no. 6, p. 1,199–1,222. http://doi.org/10.1007/s00024-010-0231-9

Nicolsky, D.J., Suleimani, E.N., and Koehler, R.D., 2014a, Tsunami inundation maps of Cordova and Tatitlek, Alaska: Alaska Division of Geological & Geophysical Surveys Report of Investigation 2014-1, 49 p., 2 sheets. http://doi.org/10.14509/27241

Nicolsky, D.J., Suleimani, E.N., and Koehler, R.D., 2014b, Tsunami inundation maps of the villages of Chenega Bay and northern Sawmill Bay, Alaska: Alaska Division of Geological & Geophysical Surveys Report of Investigation 2014-3, 50 p., 7 sheets. http://doi.org/10.14509/29126

Nicolsky, D.J., Suleimani, E.N., Koehler, R.D., and Salisbury, J.B., 2017, Tsunami inundation maps for Juneau, Alaska: Alaska Division of Geological & Geophysical Surveys Report of Investigation 2017-9, 66 p., 5 sheets. http://doi.org/10.14509/29741

Nishenko, S.P., and Jacob, K.H., 1990, Seismic potential of the Queen Charlotte–Alaska–Aleutian seismic zone: Journal of Geophysical Research, v. 95, no. B3, p. 2,511–2,532. http://doi.org/10.1029/JB095iB03p02511

Nottingham, D.P.E., 1997, The 1994 Skagway tsunami tide gage record: Science of Tsunami Hazards, v. 15, no. 2, p. 81–88.

NTHMP, 2010, National Tsunami Hazard Mitigation Program, Guidelines and best practices for tsunami inundation modeling for evacuation planning: National Oceanic and Atmospheric Administration (NOAA), NTHMP Mapping & Modeling Subcommittee.

———2012, Proceedings and results of the 2011 NTHMP Model Benchmarking Workshop: Boulder, CO, U.S. Department of Commerce/NOAA/NTHMP, NOAA Special Report, 436 p. http://nthmp.tsunami.gov

Okada, Y., 1985, Surface deformation due to shear and tensile faults in a half-space: Bulletin of the Seismological Society of America, v. 75, no. 4, p. 1,135–1,154.

Page, R.A., 1973, The Sitka, Alaska earthquake of 1972: U.S. Geological Survey Earthquake Information Bulletin, v. 5, no. 5, p. 4–9.

Petroff, C., and Watts, P., 1995, Summary of preliminary findings on the Skagway tsunami: *Unpublished Report*, 5 p.

Plafker, G., and Greene, H.G., 1998, Report on the November 3, 1994, submarine landslide and associated landslide-generated wave at Skagway, Alaska: *Unpublished Report*.

Plafker, G., Kachadoorian, R., Eckel, E.B., and Mayo, L.R., 1969, Effects of the earthquake of March 27, 1964, on various communities: U.S. Geological Survey Professional Paper 542-G, 43 p., 2 sheets, scales 1:2,500,000 and 1:250,000. http://pubs.usgs.gov/pp/0542g/

Rabinovich, A.B., Thomson, R.E., Kulikov, E.A., Bornhold, B.D., and Fine, I. V., 1999, The landslide-generated tsunami of November 3, 1994 in Skagway Harbor, Alaska: A case study: Geophysical Research Letters, v. 26, no. 19, p. 3009–3012. http://doi.org/10.1029/1999GL002334

Raichlen, F., Lee, J.J., Petroff, C., and Watts, P., 1996, The generation of waves by a landslide: Skagway, Alaska—A case study: Proceedings of the 25th International Conference on Coastal Engineering, ASCE, Orlando, Florida. https://doi.org/10.1061/9780784402429.101

Ross, S.L., Jones, L.M., Miller, K., Porter, K.A., Wein, A., Wilson, R.I., Bahng, B., Barberopoulou, A., Borrero, J.C., Brosnan, D.M., Bwarie, J.T., Geist, E.L., Johnson, L.A., Kirby, S.H., and others, 2013, SAFRR (Science Application for Risk Reduction) Tsunami Scenario—Executive Summary and Introduction: U.S. Geological Survey Open-File Report 2013–1170–A, *in* Ross, S.L., and Jones, L.M., eds., The SAFRR (Science Application for Risk Reduction) Tsunami Scenario: U.S. Geological Survey Open-File Report 2013–1170, 17 p. http://pubs.usgs.gov/of/2013/1170/a/

Ryan, H., von Huene, R., Scholl, D., and Kirby, S., 2012, Tsunami hazards to US coasts from giant earthquakes in Alaska: Eos Transactions, American Geophysical Union, v. 93, no. 19, 185 p. http://doi.org/10.1029/2012EO190001

Schwab, W.C., Lee, H.J., and Twichell, D.C., 1993, Submarine landslides; Selected studies in the U.S. Exclusive Economic Zone: U.S. Geological Survey Bulletin 2002, 204 p. https://pubs.er.usgs.gov/publication/b2002

Shannon, W.L., and Hilts, D.E., 1973, Earthquake-caused submarine landslide at Seward, Alaska, in The Great Alaska Earthquake of 1964: National Academy of Sciences, Engineering, Publication 1606, p. 144–156.

Shao, G., Li, X., Ji, C., and Maeda, T., 2011, Focal mechanism and slip history of 2011 M_W 9.1 off the Pacific coast of Tohoku earthquake, constrained with teleseismic body and surface waves: Earth, Planets and Space, v. 63, no. 7, p. 559–564. http://doi.org/10.5047/eps.2011.06.028

Shelby, M., Grilli, S.T., and Grilli, A.R., 2016, Tsunami hazard assessment in the Hudson River Estuary based on dynamic tsunami–tide simulations: Pure and Applied Geophysics, v. 173, no. 12, p. 3,999–4,037. http://doi.org/10.1007/s00024-016-1315-y

Shennan, I., Barlow, N., and Combellick, R.A., 2008, Paleoseismological records of multiple great earthquakes in southcentral Alaska—A 4,000-year record at Girdwood, *in* Freymueller, J.T., Haeussler, P.J., Wesson, R.L, and Ekström, Goran, eds., Active Tectonics and Seismic Potential of Alaska: American Geophysical Union Geophysical Monograph 179, p. 185–199.

Soloviev, S.L., and Go, C.N., 1975, Catalog of tsunamis on the eastern shore of the Pacific Ocean: Academy of Science of the USSR.

Suito, H., and Freymueller, J.T., 2009, A viscoelastic and afterslip postseismic deformation model for the 1964 Alaska earthquake: Journal of Geophysical Research, v. 114, no. B11, p. 404–426. http://doi.org/10.1029/2008JB005954

Suleimani, E.N., 2011, Numerical studies of tectonic and landslide-generated tsunamis caused by the 1964 Great Alaska Earthquake: Fairbanks, Alaska, University of Alaska Fairbanks, Ph.D. dissertation, 181 p.

Suleimani, E.N., Nicolsky, D.J., and Koehler, R.D., 2013, Tsunami inundation maps of Sitka, Alaska: Alaska Division of Geological & Geophysical Surveys Report of Investigation 2013-3, 76 p., 1 sheet, scale 1:12,500. http://doi.org/10.14509/26671

Suleimani, E.N., Nicolsky, D.J., and Koehler, R.D., 2015, Tsunami inundation maps of Elfin Cove, Gustavus, and Hoonah, Alaska: Alaska Division of Geological & Geophysical Surveys Report of Investigation 2015-1, 79 p., 3 sheets. http://doi.org/10.14509/29404

Suleimani, E.N., Nicolsky, D.J., and Koehler, R.D., 2016, Tsunami inundation maps for Yakutat, Alaska: Alaska Division of Geological & Geophysical Surveys Report of Investigation 2016-2, 47 p., 1 sheet, scale 1:10,000. http://doi.org/10.14509/29577

Suleimani, E.N., Nicolsky, D.J., West, D.A., Combellick, R.A., and Hansen, R.A., 2010, Tsunami inundation maps of Seward and northern Resurrection Bay, Alaska: Alaska Division of Geological & Geophysical Surveys Report of Investigation 2010-1, 47 p., 3 sheets, scale 1:12,500. http://doi.org/10.14509/21001

Sykes, L.R., 1971, Aftershock zones of great earthquakes, seismicity gaps, and earthquake prediction for Alaska and the Aleutians: Journal of Geophysical Research, v. 75, p. 8,021–8,041.

Synolakis, C.E., 1999, Modeling of the November 3, 1994 Skagway, Alaska tsunami: *Unpublished Report*, 36 p.

Synolakis, C.E., Bernard, E.N., Titov, V. V., Kânoğlu, U., and González, F.I., 2007, Standards, criteria, and procedures for NOAA evaluation of tsunami numerical models: Seattle, Washington, NOAA/Pacific Marine Environmental Laboratory, Technical Memorandum OAR PMEL-135, 55 p.

Tang, L., Titov, V. V., Bernard, E.N., Wei, Y., Chamberlin, C.D., Newman, J.C., Mofjeld, H.O., Arcas, D., Eble, M.C., Moore, C., Uslu, B., Pells, C., Spillane, M., Wright, L., and others, 2012, Direct energy estimation of the 2011 Japan tsunami using deep-ocean pressure measurements: Journal of Geophysical Research, v. 117, no. C8. http://doi.org/10.1029/2011JC007635

Tarr, R.S., and Martin, L., 1912, The earthquakes at Yakutat Bay, Alaska, in September, 1899; preface by G. K. Gilbert: U.S. Geological Survey Professional Paper 69, 135 p., 3 sheets, scale 1:5,000,000. http://pubs.er.usgs.gov/publication/pp69

Tehranirad, Babak, Kirby, J.T., Ma, Gangfeng, and Shi, Fengyan, 2012, Tsunami benchmark results for non-hydrostatic wave model NHWAVE, Version 1.1: Newark, NJ, University of Delaware Center for Applied Coastal Research, Research Report No. CACR-12-03, 43 p.

Thomson, R.E., Rabinovich, A.B., Kulikov, E.A., Fine, I. V., and Bornhold, B.D., 2001, On numerical simulation of the landslide-generated tsunami of November 3, 1994 in Skagway Harbor, Alaska *in* Hebenstreit, G. T. (eds) Tsunami Research at the End of a Critical Decade; Advance in Natural and Technological Hazards Research, vol. 18, Springer, Dordrecht.

Tocher, D., 1960, The Alaska earthquake of July 10, 1958: Movement on the Fairweather fault and field investigation of southern epicentral region: Bulletin of the Seismological Society of America, v. 50, no. 2, p. 267–292.

Tolkova, E., 2013, Tide–tsunami interaction in the Columbia River, as implied by historical data and numerical simulations: Pure and Applied Geophysics, v. 170, no. 6–8, p. 1115-1126. http://doi.org/10.1007/s00024-012-0518-0

Tolkova, E., Tanaka, H., and Roh, M., 2015, Tsunami observations in rivers from a perspective of tsunami interaction with tide and riverine flow: Pure and Applied Geophysics, v. 172, no. 3–4, p. 953–968. http://doi.org/10.1007/s00024-014-1017-2

Watada, S., Kusumoto, S., and Satake, K., 2014, Traveltime delay and initial phase reversal of distant tsunamis coupled with the self-gravitating elastic Earth: Journal of Geophysical Research: Solid Earth, v. 119, no. 5, p. 4287–4310. http://doi.org/10.1002/2013JB010841

Wieczorek, G.F., Geist, E.L., Motyka, R.J., and Jakob, M., 2007, Hazard assessment of the Tidal Inlet landslide and potential subsequent tsunami, Glacier Bay National Park, Alaska: Landslides, v. 4, no. 3, p. 205–215.

Wilson, B.W., and Tørum, A., 1968, The tsunami of the Alaskan earthquake, 1964—Engineering evaluation: Vicksburg, MI, U.S. Army Corps of Engineers Technical Memorandum No. 25, 401 p.

Yeh, H., Tolkova, E., Jay, D., Talke, S., and Fritz, H., 2012, Tsunami hydrodynamics in the Columbia River: Journal of Disaster Research, v. 7, no. 5, p. 604–608.

APPENDIX A

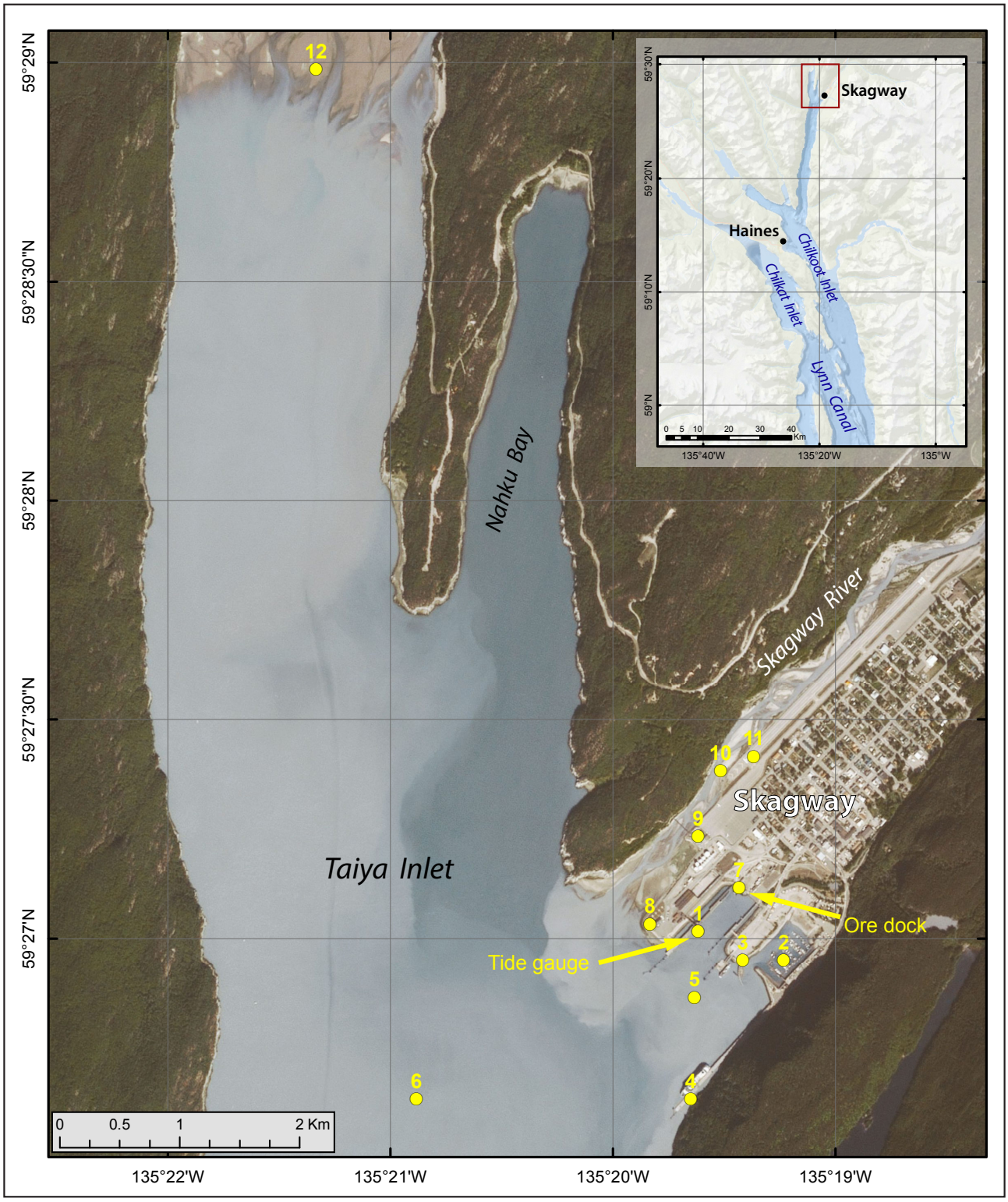

Figure A-1. Locations of time series points near Skagway. The longitude and latitude locations of the time series points are listed in table A-1.

Table A-1. Maximum water levels and water velocity at time series points near Skagway. The maximum water depth above ground is provided for pre-earthquake onshore (S) locations, whereas the maximum water level above the pre-earthquake MHHW is provided for offshore (O) locations. The minimum elevation (sixth column) above the post-earthquake MHHW datum is provided for onshore locations, while the minimum post-earthquake depth is provided for offshore locations. Blank cells indicate that the water dynamics for the particular landslide-generated tsunami scenario was not modeled at these locations because of the slide was located far away. The horizontal datum used is World Geodetic System of 1984.

#	Label	S/O	Longitude (°W)	Latitude (°N)	Minimum elevation/ depth (m)	Maximum Water Depth Above Ground/Sea Level (m)				Maximum Water Velocity (m/sec)			
						Tectonic scenarios (with the effective slip)		Landslide scenario		Tectonic scenarios (with the effective slip)		Landslide scenario	
						1M	4M	8	9	1M	4M	8	9
1	Skagway tide gauge	O	-135.326944	59.450278	1.8	2.5	0	0	0	0.1	17	0	0
2	Small Boat Harbor	O	-135.320556	59.449167	1.8	2.5	0.1	0	0	0.2	8.5	0	0
3	Broadway Dock	O	-135.323611	59.449167	1.8	2.5	0.5	0	0	1.4	3.7	0	0
4	Railroad Dock	O	-135.3275	59.443889	1.8	2.5	0.1	0	0	0.1	11.9	0	0
5	Skagway Harbor	O	-135.327222	59.447778	1.8	2.5	0	0.3	0	0.1	45.7	0.7	0
6	Upper Taiya Inlet	O	-135.348056	59.443889	1.8	2.5	0.1	0.7	0	0.1	169.9	0.7	0
7	Ore Dock	S	-135.323889	59.451944	1.5	2.2	0	7.4	0.2	0	0.4	5.1	0.1
8	Temsco Helicopters	S	-135.330556	59.450556	0	0	0	1.2	0.1	0	3.6	0.8	0.1
9	Skagway Airport	S	-135.326944	59.453889	0	0	0	2.7	0.6	0	3.6	0.9	0.1
10	Skagway River	S	-135.325278	59.456389	1.7	2.5	0.6	0.2	0	0.9	0.1	5.9	0
11	Airstrip	S	-135.322778	59.456944	0	0	0	0.0	0	0	4.5	0.0	0
12	Head of Taiya Inlet	O	-135.355556	59.483056	2	2.7	1.4	0.5	0	2.5	3.9	2.8	0

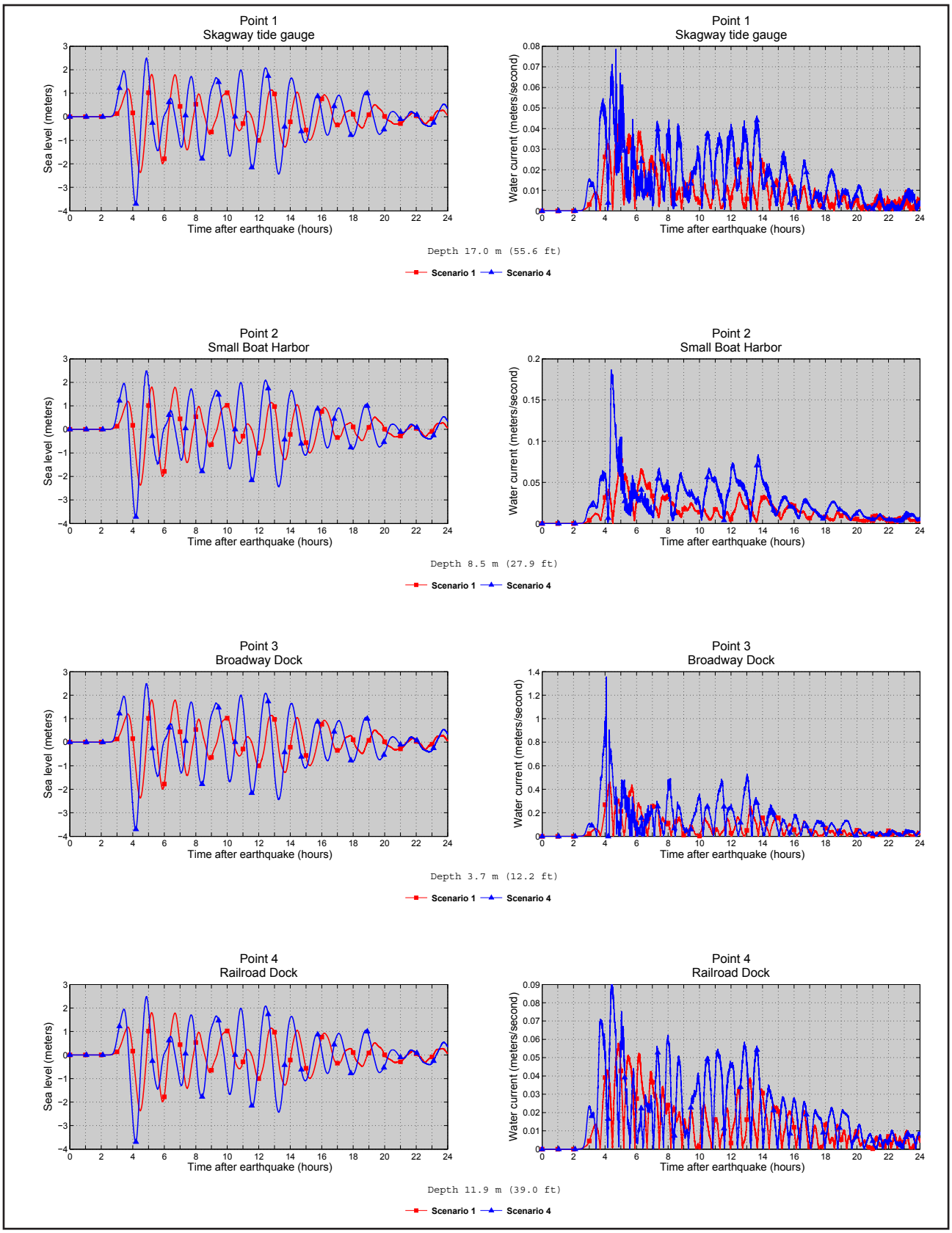

Figure A-2. Time series of the water level (left column) and velocity (right column) for tectonic scenarios 1 and 4 (with the effective slip parameterization to account for the tsunami-tide interactions) at locations shown in figure A-1. Elevations of onshore locations and ocean depth at offshore locations are given based on the pre-earthquake MHHW datum.

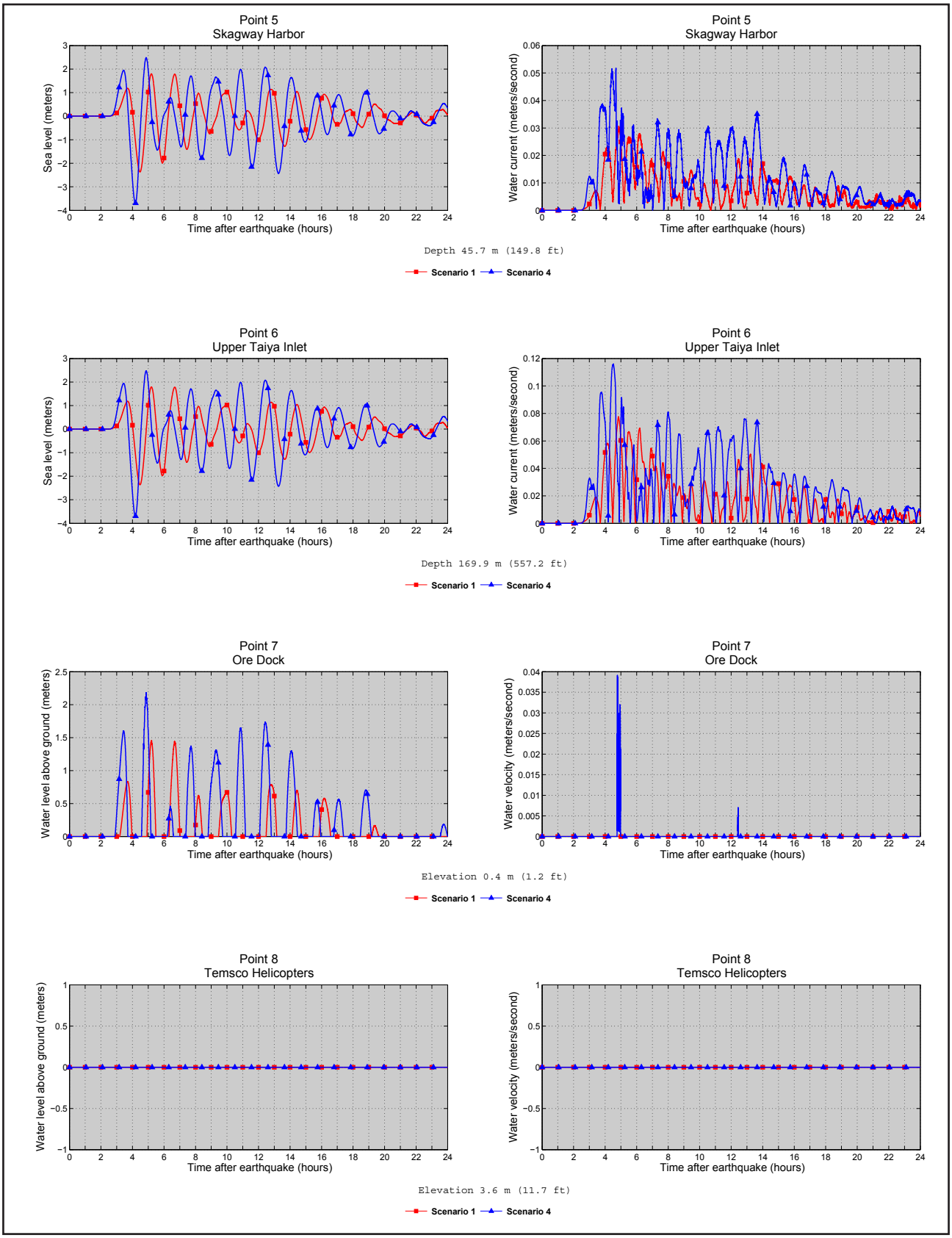

Figure A-2, continued. Time series of the water level (left column) and velocity (right column) for tectonic scenarios 1 and 4 (with the effective slip parameterization to account for the tsunami-tide interactions) at locations shown in figure A-1. Elevations of onshore locations and ocean depth at offshore locations are given based on the pre-earthquake MHHW datum.

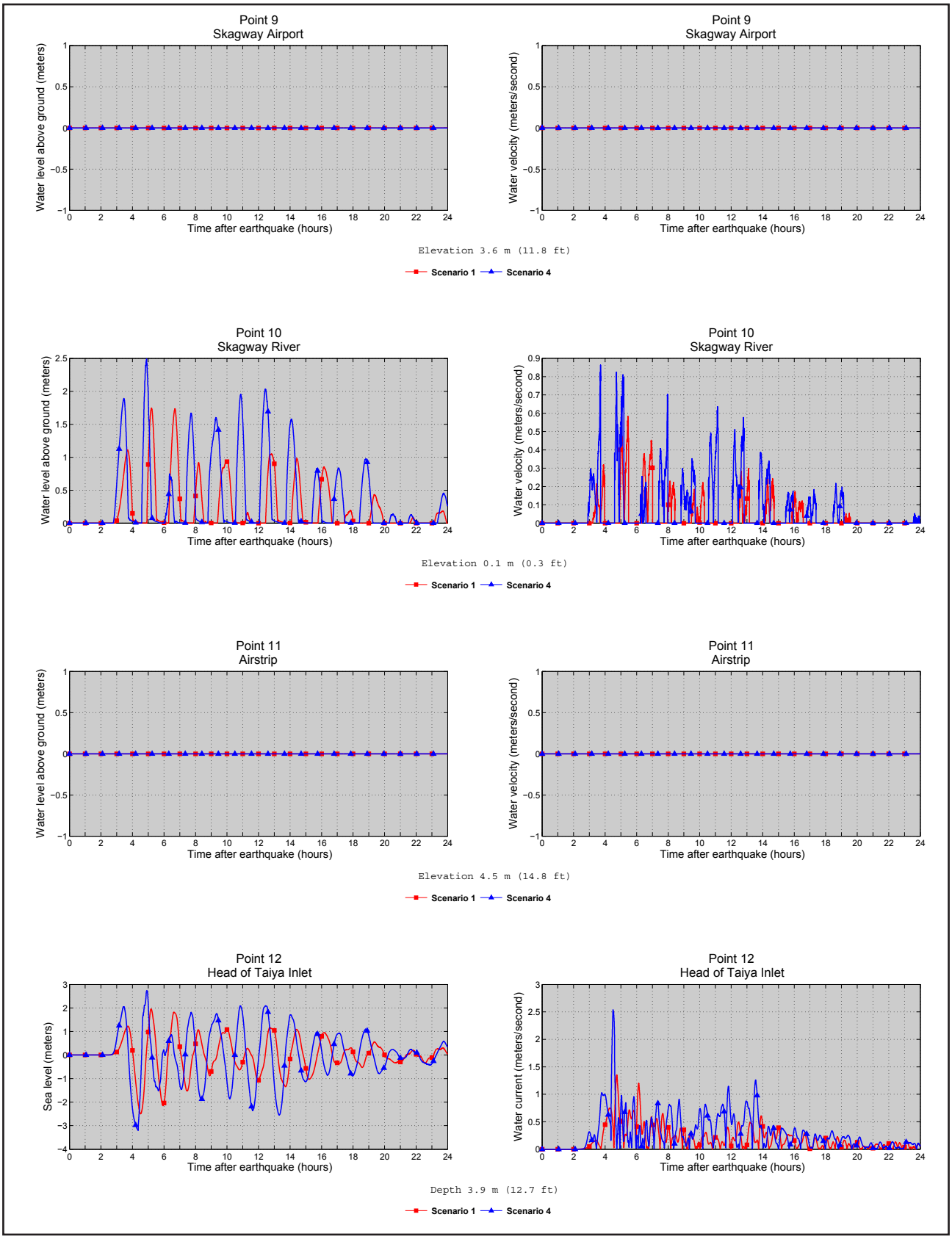

Figure A-2, continued. Time series of the water level (left column) and velocity (right column) for tectonic scenarios 1 and 4 (with the effective slip parameterization to account for the tsunami-tide interactions) at locations shown in figure A-1. Elevations of onshore locations and ocean depth at offshore locations are given based on the pre-earthquake MHHW datum.

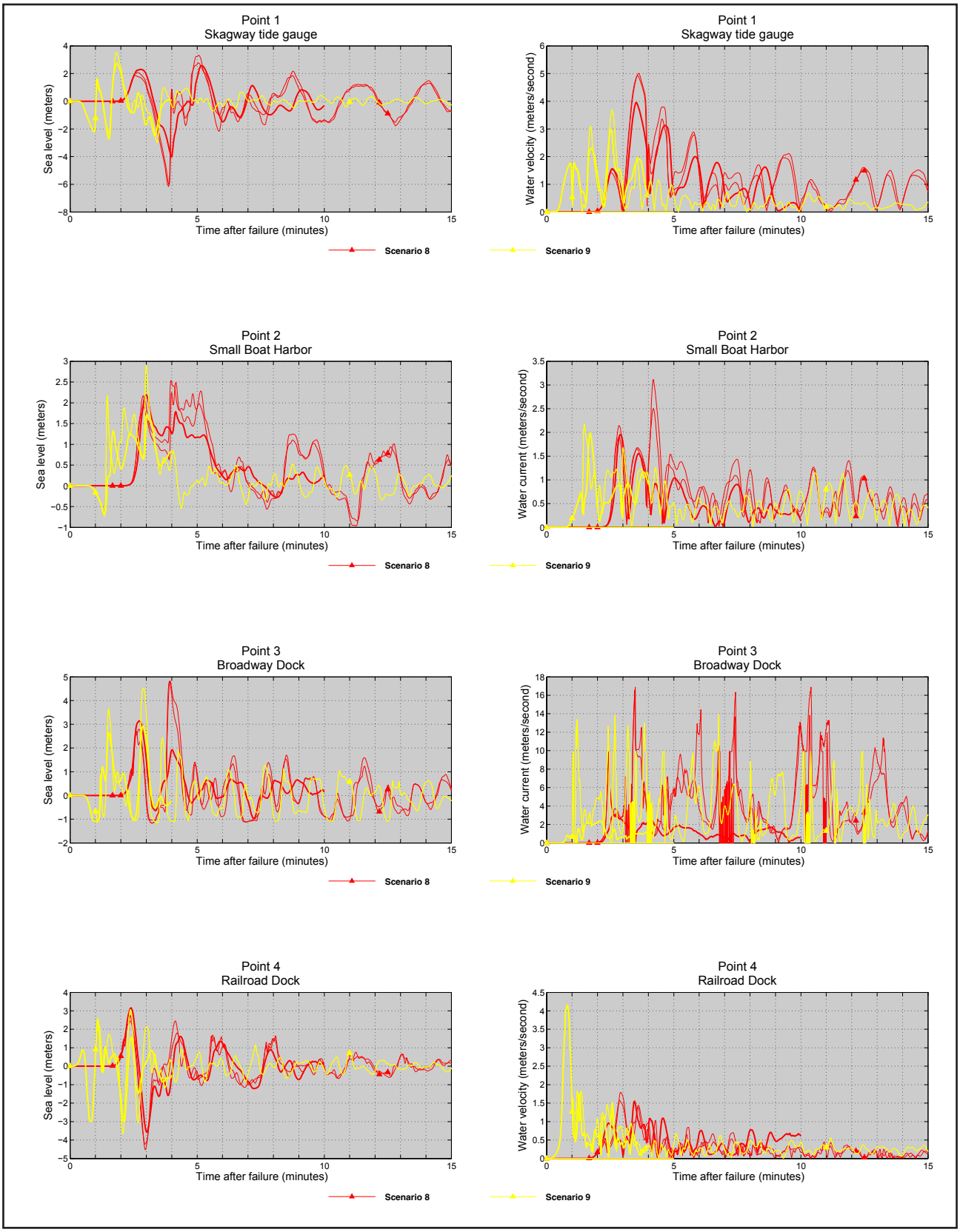

Figure A-3. Time series of the water level (left column) and velocity (right column) for landslide scenarios 8 and 9 at locations shown in figure A-1.

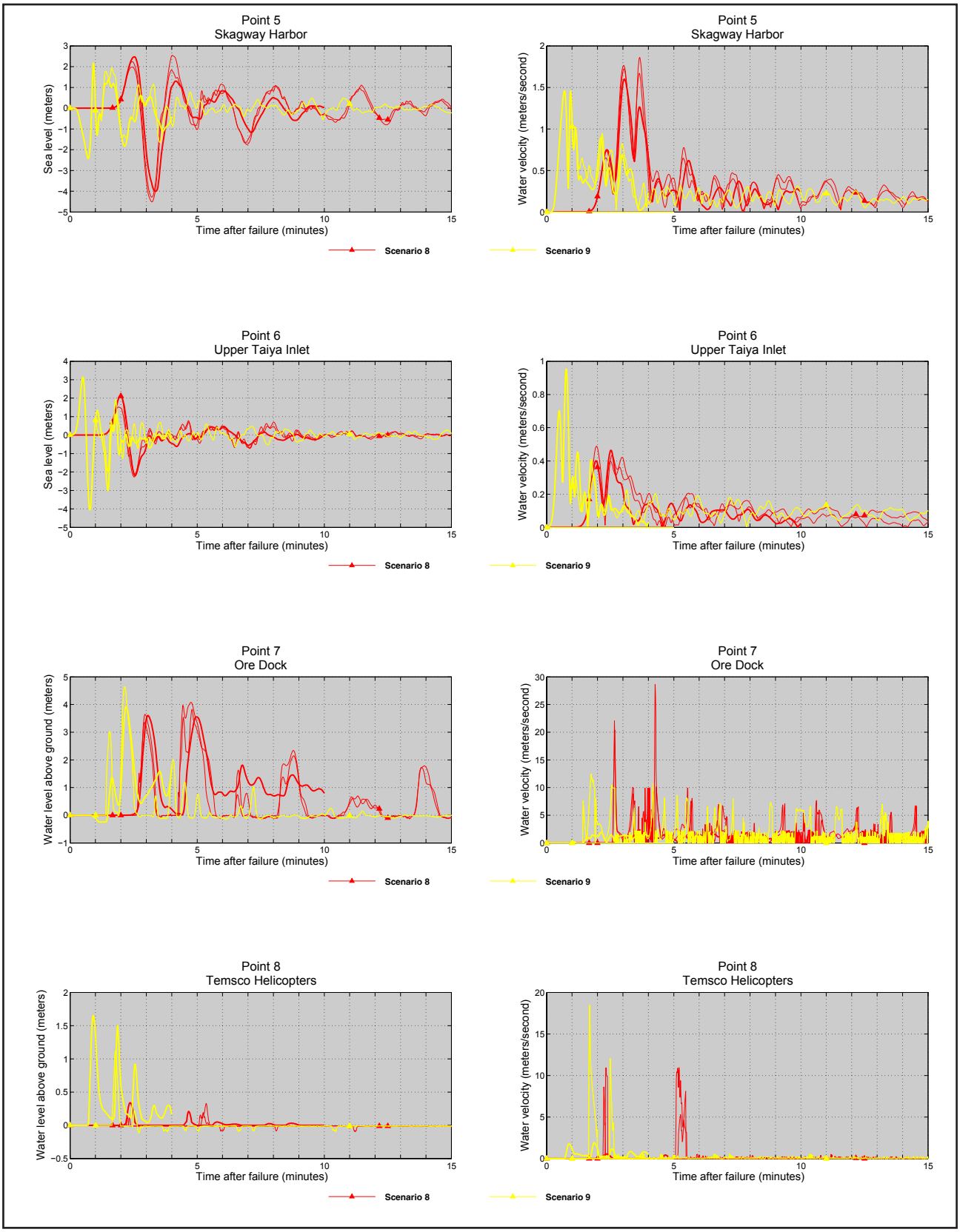

Figure A-3, continued. Time series of the water level (left column) and velocity (right column) for landslide scenarios 8 and 9 at locations shown in figure A-1.

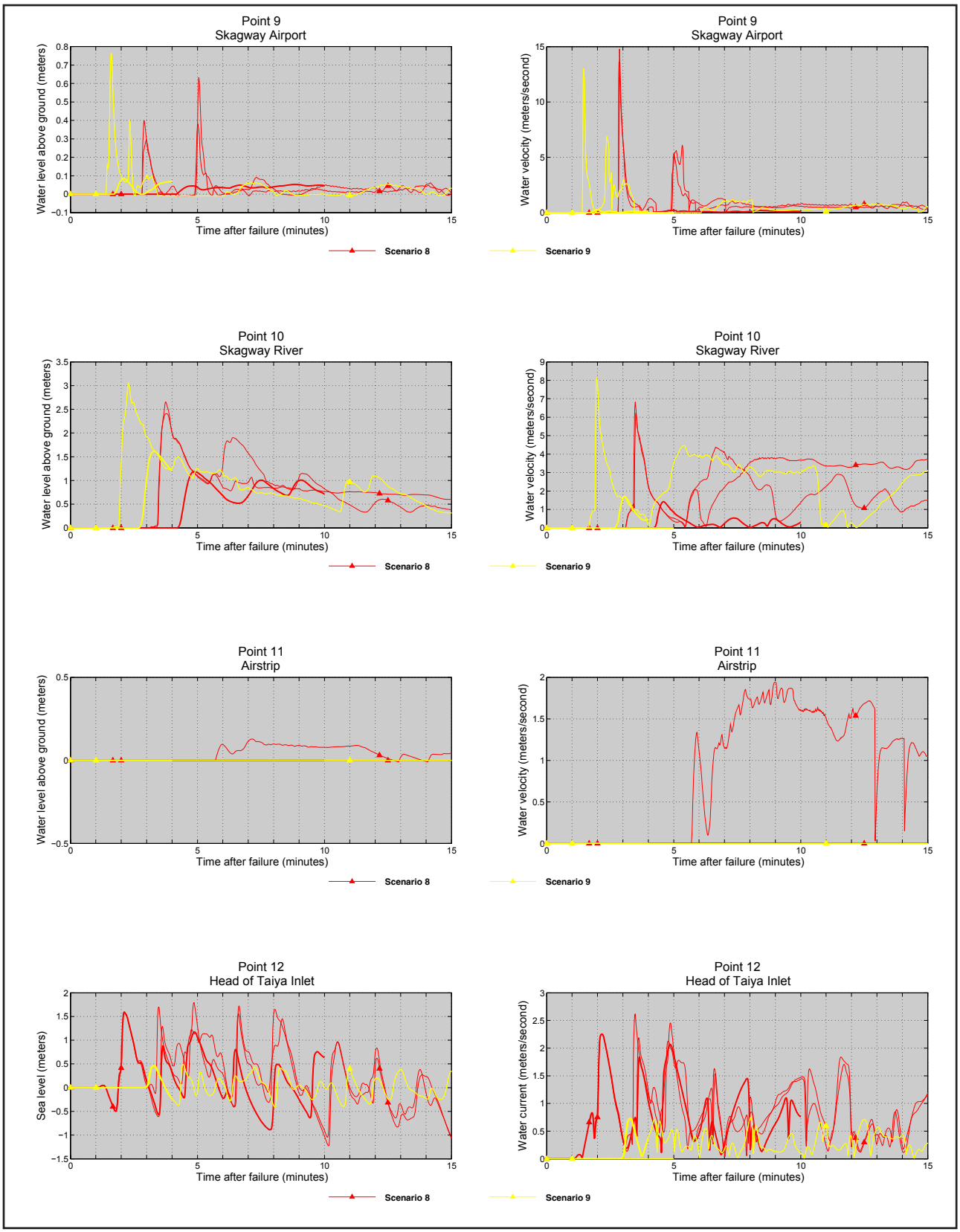

Figure A-3, continued. Time series of the water level (left column) and velocity (right column) for landslide scenarios 8 and 9 at locations shown in figure A-1.

APPENDIX B

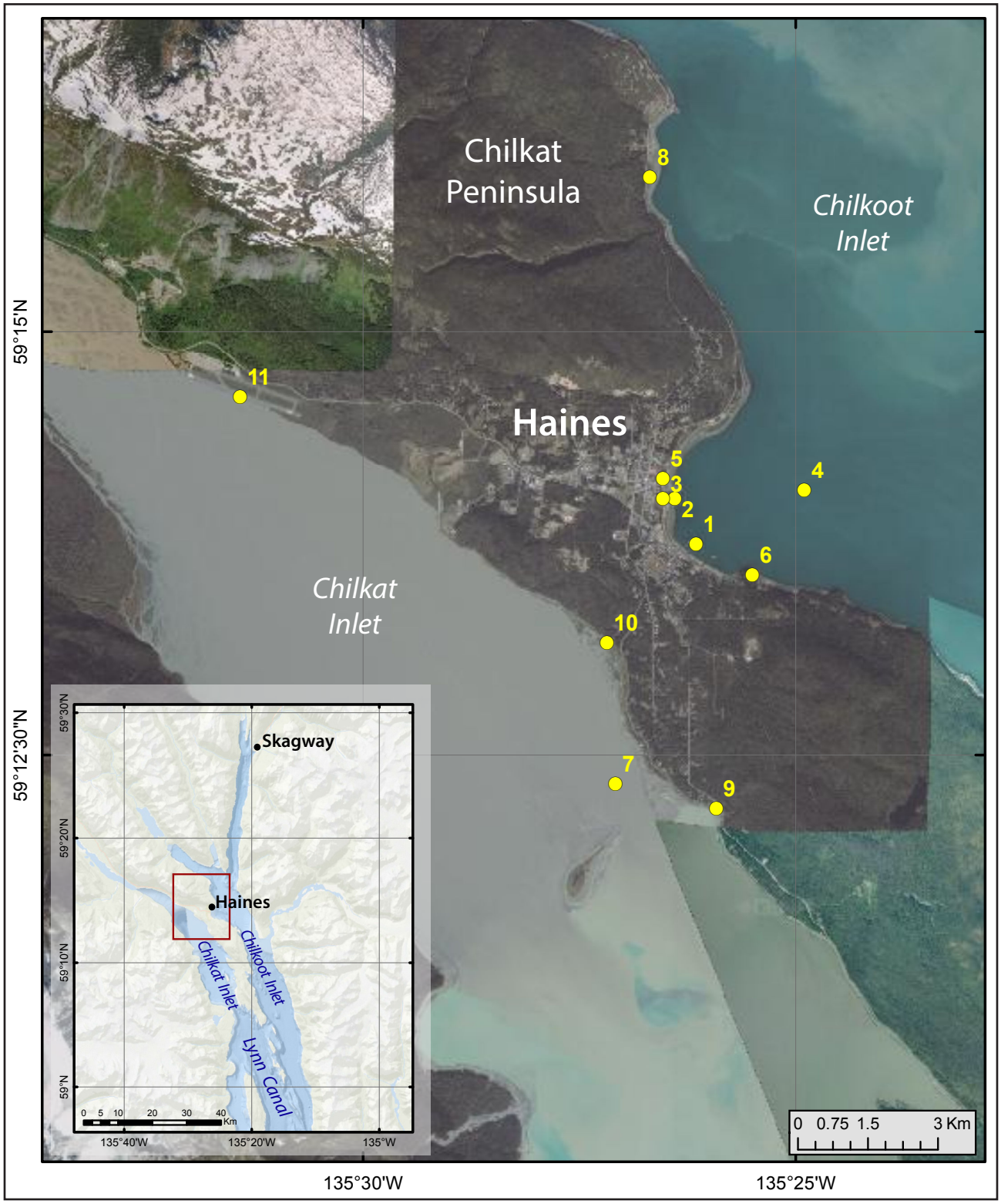

Figure B-1. Locations of time series points near Haines. The longitude and latitude locations of the time series points are listed in table B-1.

Table B-1. Maximum water levels and water velocity at time series points near Haines. The maximum water depth above ground is provided for pre-earthquake onshore (S) locations, whereas the maximum water level above the pre-earthquake MHHW is provided for offshore (O) locations. The minimum elevation (sixth column) above the post-earthquake MHHW datum is provided for onshore locations, while the minimum post-earthquake depth is provided for offshore locations. Blank cells indicate that the water dynamics for the particular landslide-generated tsunami scenario was not modeled at these locations because of the slide was located far away. The horizontal datum used is World Geodetic System of 1984.

#	Label	S/O	Longitude (°W)	Latitude (°N)	Minimum elevation/ depth (m)	Maximum Water Depth Above Ground/Sea Level (m)						Maximum Water Velocity (m/ sec)					
						Tectonic scenarios (with the effective slip)		Landslide scenario				Tectonic scenarios (with the effective slip)		Landslide scenario			
						1M	4M	10	11	12	13	1M	4M	10	11	12	13
1	Port Chilkoot Dock	O	-135.435833	59.229167	1.4	1.7	0.1	0	0	4.9	1.3	0.1	12.6	0	0	18.8	1.2
2	Small Boat Harbor	O	-135.44000	59.233611	1.4	1.7	0	0	0	8.2	1.9	0.1	9.6	0	0	12.3	1.6
3	Harbor parking	S	-135.442222	59.233611	0	0	0	0	0	6.4	0	0	5.3	0	0	24.2	0
4	Portage Cove	O	-135.415000	59.234444	1.4	1.7	0.2	0	0	3.5	0.8	0.3	81.4	0	0	1.3	0.3
5	Front Street	S	-135.442222	59.235556	0	0	0	0	0	4.3	0	0	7.1	0	0	14.8	0
6	Portage Cove Campground	S	-135.425000	59.226111	0	0	0	0	0	4.4	0	0	2.6	0	0	12.9	0
7	Chilkat Inlet	O	-135.451389	59.205556	0.9	2	1.4	3.3	2.1	0	0	2.7	3.6	4.3	3.2	0.1	0
8	Beach of Tanani Bay	S	-135.444722	59.265278	0.4	0.8	0.1	0	0	9.5	4.2	0.2	1.1	0	0	21.1	18.6
9	Mud Bay Road	S	-135.431944	59.203056	0	0	0	0.2	0	0	0	0	8.7	0.8	0	0	0
10	River Road	S	-135.453056	59.219444	0	0.9	0	1.7	1.3	0	0	0.1	1.4	11.6	6.8	0	0
11	Haines Airport	S	-135.523611	59.243611	0	0	0	0.7	0	0	0	0	2.2	2.8	0	0	0

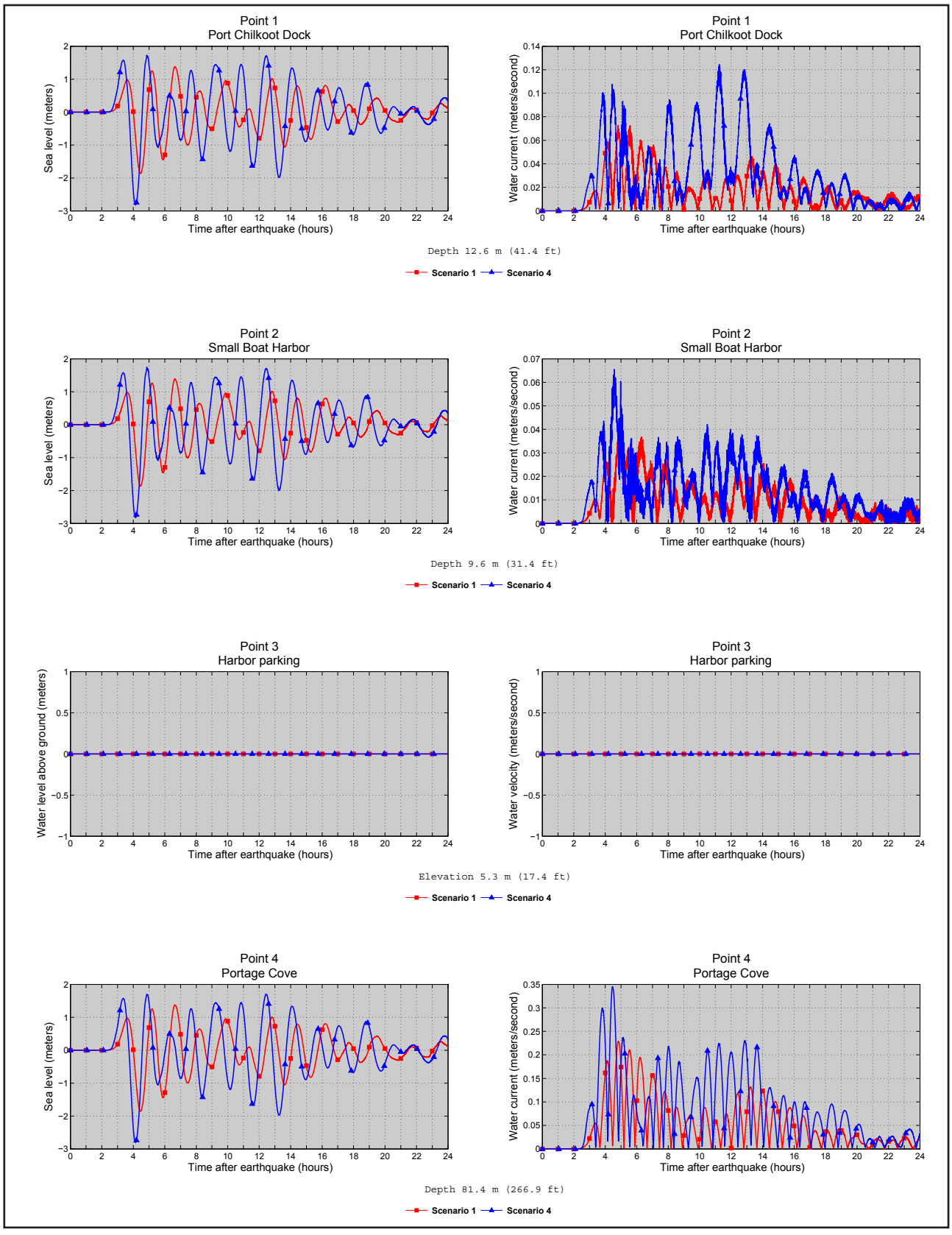

Figure B-2. Time series of the water level (left column) and velocity (right column) for tectonic scenarios 1 and 4 (with the effective slip parameterization to account for the tsunami-tide interactions) at locations shown in figure B-1. Elevations of onshore locations and ocean depth at offshore locations are given based on the pre-earthquake MHHW datum.

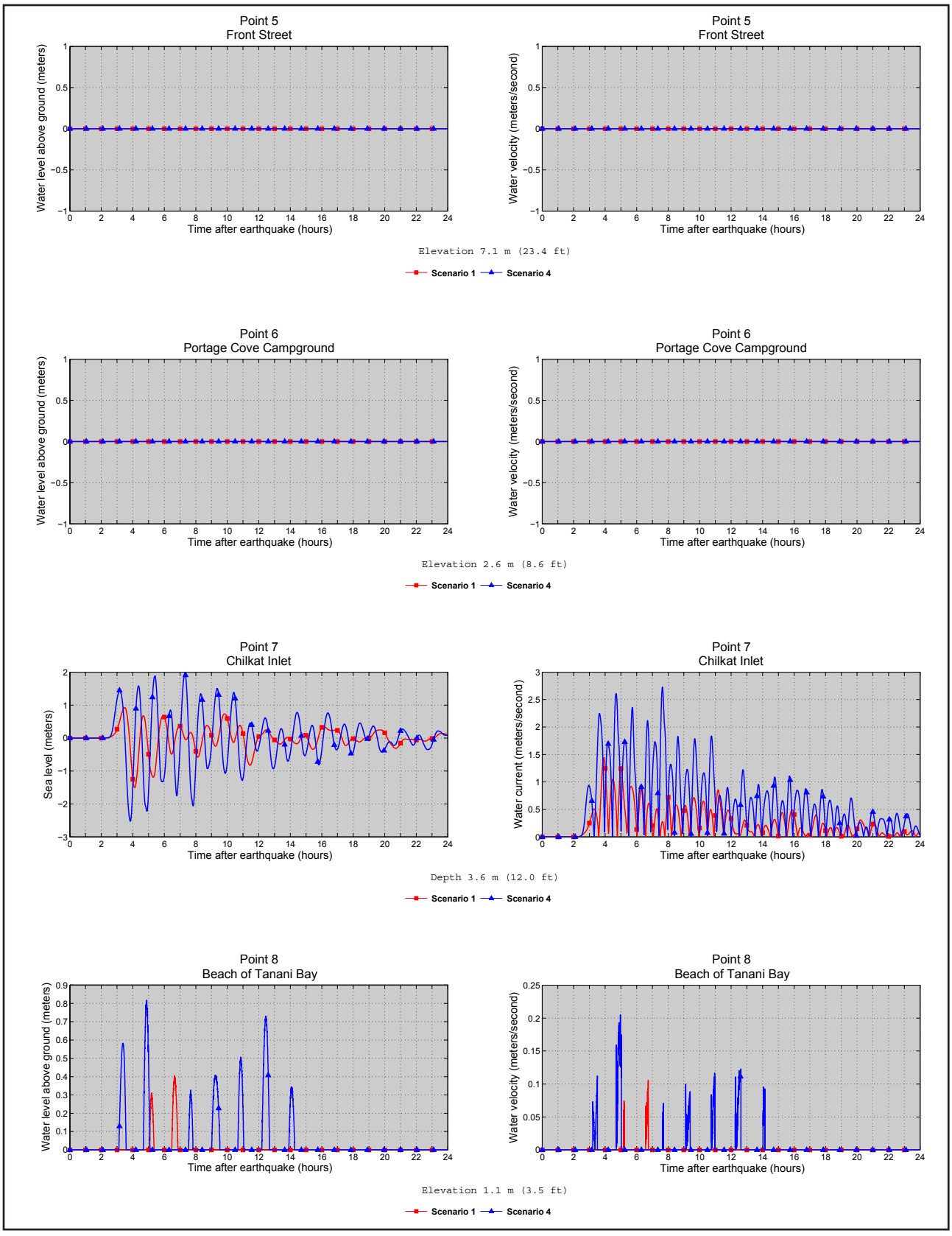

Figure B-2, continued. Time series of the water level (left column) and velocity (right column) for tectonic scenarios 1 and 4 (with the effective slip parameterization to account for the tsunami-tide interactions) at locations shown in figure B-1. Elevations of onshore locations and ocean depth at offshore locations are given based on the pre-earthquake MHHW datum.

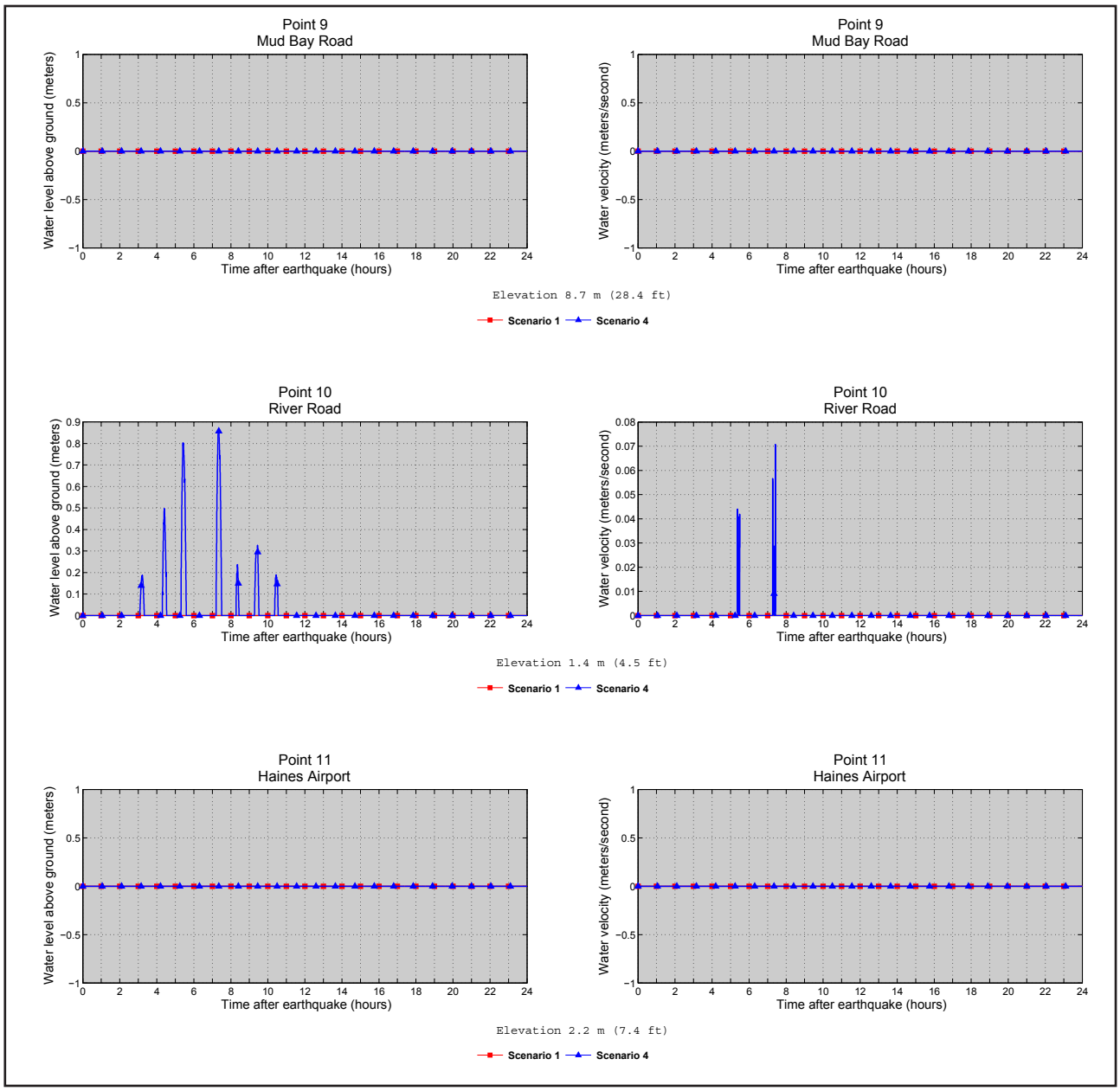

Figure B-2, continued. Time series of the water level (left column) and velocity (right column) for tectonic scenarios 1 and 4 (with the effective slip parameterization to account for the tsunami-tide interactions) at locations shown in figure B-1. Elevations of onshore locations and ocean depth at offshore locations are given based on the pre-earthquake MHHW datum.

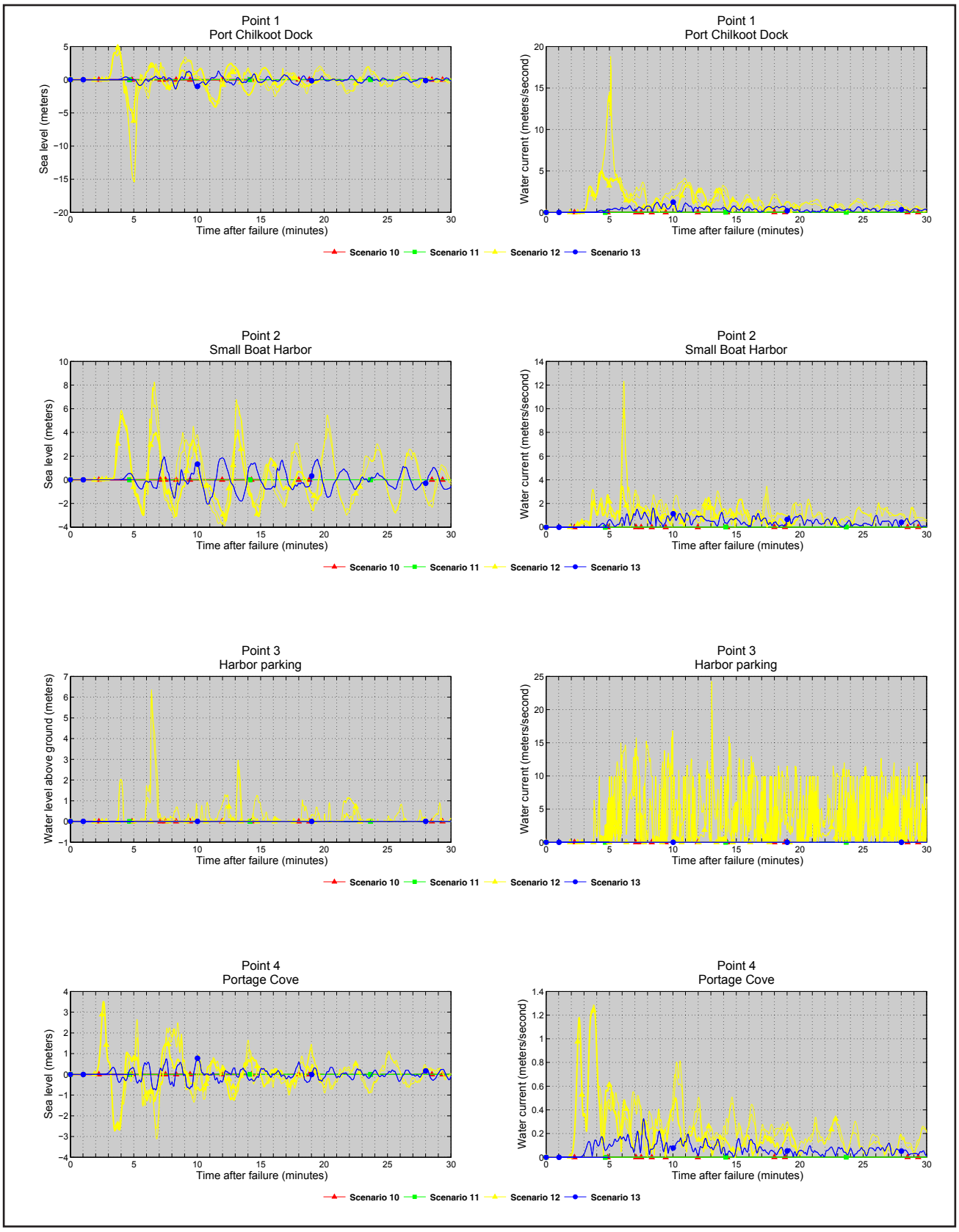

Figure B-3. Time series of the water level (left column) and velocity (right column) for landslide scenarios 10–13 at locations shown in figure B-1.

Figure B-3, continued. Time series of the water level (left column) and velocity (right column) for landslide scenarios 10-13 at locations shown in figure B-1.

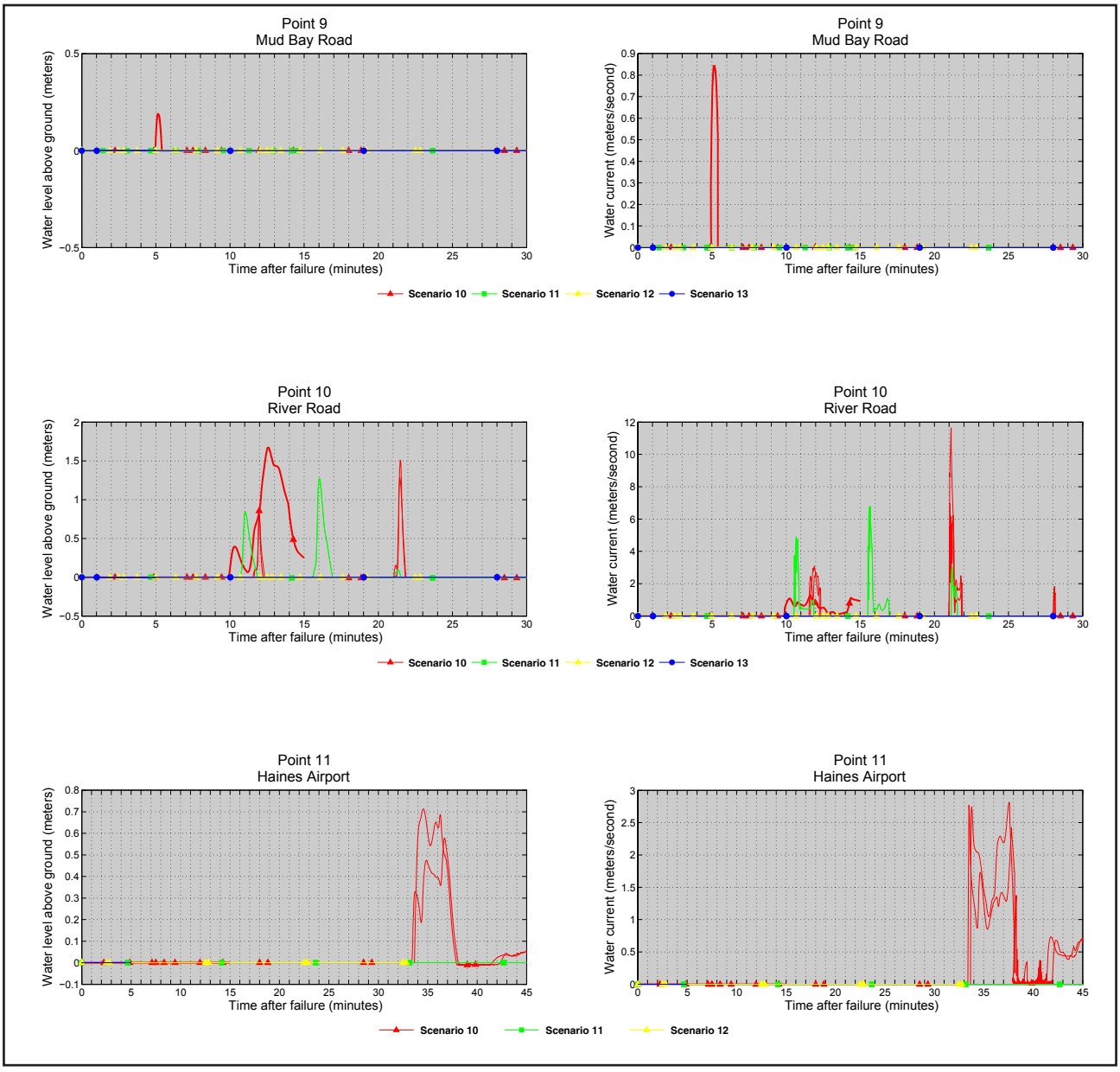

Figure B-3, continued. Time series of the water level (left column) and velocity (right column) for landslide scenarios 10-13 at locations shown in figure B-1.